NTNU
Det skapende universitet

Silisium Racetrack Resonator

Design og Fabrikasjon

Leidulv Vigen

Elektronisk systemdesign og innovasjon
Innlevert: januar 2014
Hovedveileder: Astrid Aksnes, IET

Norges teknisk-naturvitenskapelige universitet
Institutt for elektronikk og telekommunikasjon

Problem Description

Microphotonics is a sub-branch of photonics oriented towards integrated systems on a single semiconductor chip. It involves the design, fabrication and testing of optical components to be fabricated at micro- or even nano-scale. Examples of these components are dielectric waveguides, micro-resonators, light modulators, couplers, periodic structures and more.

The purpose of this master thesis is to design and fabricate waveguides and a micro-racetrack resonator at the NTNU NanoLab. The fabrication will be based on simulations done in the project thesis. The micro photonic structures will be made in single crystalline silicon to prepare for future silicon-on-insulator (SOI) waveguide fabrication. The fabrication process will consist of electron beam lithography (EBL) and inductively coupled plasma reactive ion etching (ICP-RIE). The results will be inspected using a scanning tunnelling electron microscope (S(T)EM). The work will be iterative, drawing extensively on the expertise and knowledge of the engineers and other users of the cleanroom in the beginning. One of the main challenges of the project will be to tune processing parameters with respect to the characterization results. The goal of this master thesis work is to achieve straight sidewall profiles with minimal sidewall roughness.

It is expected that significant amounts of time will be spent in the cleanroom as fabrication relies on cleanroom "know-how" and experience with the machines, in addition to established processing techniques. Acquiring the necessary experience and "know-how" will be time-consuming. Part of the purpose of this thesis is to add competence and experience to the NTNU NanoLab within the field of processing microphotonic structures to prepare for the increasing amount of research performed in this field.

Abstract

This thesis studies silicon photonic wire waveguides and racetrack resonators, with the aim of designing a waveguide and a resonator, and optimising the fabrication processes required for future testing. It is intended to be a platform for waveguide fabrication on silicon-on-insulator wafers and testing of silicon photonic components at the NTNU NanoLab. COMSOL Multiphysics was used in a previous project to simulate and design the racetrack resonator. Electron beam lithography and a fluorine based inductively coupled plasma reactive ion etching are used to fabricate waveguides, inverse tapered waveguides, and racetrack resonators in single crystalline silicon wafer dies. The waveguides have dimensions of 500×220 nm^2, and the tapered waveguides taper from 500 nm to 150 nm over 100 μm. The racetrack resonator is designed for coupling from waveguides spaced 200 nm apart, with a coupling region of 1.8113 μm and a bend radius of 3.2208 μm. 3×3 μm^2 polymer spot-size converters made from S1818 photoresist are proposed and fabricated. Waveguides with $\sim 90^\circ$ sidewall profiles and roughness of $\sim$5 nm in size were realised. The exposure dose is observed to contribute significantly to the sidewall profiles, however the required dose is discovered to vary between samples retaining equal resist thickness. An etching process using SF_6/CHF_3 chemistry is found to provide an adequate selectivity between silicon and PMMA of 2.11 by using a sapphire carrier wafer.

Sammendrag

Denne oppgaven studerer fotoniske silisiumsbølgeledere og ovale resonatorer, med sikte på å utforme en bølgeleder og en resonator, og å optimalisere fabrikasjonsprosessene som kreves for fremtidig testing. Dette er ment for å være en plattform for videre fabrikasjon av bølgeledere på silisium-på-isolator wafere og testing av fotoniske komponenter i silisium ved NTNU NanoLab. COMSOL Multiphysics ble brukt i et tidligere prosjekt for å simulere og designe resonatoren. Elektronstrålelitografi og en fluorbasert induktivt koplet plasma reaktiv ion ets er brukt for å fabrikere bølgeledere, omvendte koniske bølgeledere , og ovale resonatorer på prøvestykker fra singelkrystallinske silisiumskiver. Bølgelederen har dimensjoner på 500×220 nm^2, og de koniske bølgelederene smalner fra 500 nm til 150 nm over 100 μm. Den ovale resonatoren er utformet for kobling mellom bølgeledere adskilt 200 nm fra hverandre, med et koplingsområde på 1.8113 μm og en bøyeradius på 3.2208 μm. 3×3 μm^2 polymer strålebreddeomformere laget fra S1818 fotoresist er foreslått og fabrikkert. Bølgeledere med $\sim 90^\circ$ sideveggprofiler og ruhetsstørrelse på $\sim$5 nm ble realisert. Eksponeringsdosen er observert å bidra vesentlig til sideveggsprofilene, men den nødvendige dosen er funnet å variere mellom prøver med lik resisttykkelse. En etseprosess som bruker SF_6/CHF_3-kjemi er funnet å gi en tilfredsstillende selektivitet mellom silisium og PMMA på 2.11 ved hjelp av en safir bærerskive.

Preface

This thesis is delivered in partial fulfilment for the degree of M.Sc. in Electronics at the Department of Electronics and Telecommunications at the Norwegian University of Science and Technology, NTNU. It builds heavily upon the work done in a precursory project thesis by the same author. The project thesis reviewed the fundamental theory and simulated silicon waveguides and racetrack resonators to optimize the dimensions. This master thesis endeavours to fabricate and realise the work done in the project thesis. Except for the important contributions by the people acknowledged below, the experimental work as well as the text in this master thesis is the individual work of the author.

Acknowledgements

Firstly I would like to give a big thanks to my supervisor professor Astrid Aksnes for her guidance and help in managing my time during the work for this thesis, interpreting results, and layout this thesis. While immensely busy she went above and beyond what was required of her, and it is greatly appreciated. Secondly I would like to thank Oleg Zero for his help during the project thesis and for providing helpful tips about working in the cleanroom. I would also like to thank Mark Chiappa and Espen Rogstad, department engineers at NTNU NanoLab, for readily offering their expertise in processing and puzzling results. I would like to thank fellow M.Sc. student Marius Lorvik for sharing his cleanroom experiences and providing valuable insight for making waveguides. Lastly I would like to thank Dr. Magnus Breivik and fellow M.Sc. student Ida Marie Høiaas for engaging in discussion on various issues.

Contents

List of Figures

Chapter 1

Introduction

Silicon photonics is a field that has received much attention in recent years. This has mostly been due to its compatibility with established silicon IC manufacturing, low cost per unit area, and high crystal quality compared to other semiconductor materials[1][2]. Silicon has low absorption in telecommunication wavelengths since the band gap for silicon is $\sim$1.1 eV[3]. For comparison the photon energy for a wavelength of 1550 nm is 0.7999 eV. Because of this propagation loss of silicon waveguide cores are mostly dependent on surface roughness. Silicon has a high refractive index contrast with respect to silicon dioxide (SiO_2) which gives strong optical confinement. This in turn makes it possible to fabricate nano-scale photonic components. Xu et al.[4] report low loss ring resonators with radii at $1.5\mu m$. Jalali and Fathpour[1] also list a number of other advantages to silicon photonics, i.e. high thermal conductivity, high optical damage threshold, and high third order non-linearities.

Recently work has been undertaken at the NTNU NanoLab to fabricate nano-scale photonic components[5][6]. This work will contribute to the growing knowledge base being built at NTNU NanoLab in the field of silicon micro- and nano-photonics. However the primary goal is to investigate the viability of fabricating the waveguide and racetrack resonator designed in the project thesis[7] as well as investigate fabrication of chip scale photonic structures at the NTNU NanoLab. The waveguides being made are 500 nm wide and 220 nm in height, the racetrack resonators have a radius of 3.2208 μm and a coupling length of 3.6226 μm to account for the 200 nm separation from the waveguide. A waveguide

core of 500×220 nm^2 was believed to fulfil single-mode conditions for the 1550 nm wavelength[8], however the single-mode condition might require a slightly smaller waveguide core at 460×200 nm^2[3]. Micro-resonators are interesting to study as they have many uses, e.g. for filter and sensing applications.

The following chapter will present fundamental electromagnetic theory and coupled mode theory, as well as give an introduction to theory regarding silicon waveguides, micro-ring resonators, and spot-size converters. Chapter 3 describes the equipment used during the work and introduce fabrication processes and explain some of the challenges with processing silicon photonic devices and considerations taken into account. Chapter 4 details the design and work flow. Chapter 5 will go through the results chronologically and discuss them in detail. Chapter 6 gives conclusions on the results based on the discussion in the previous chapter.

Chapter 2

Theory

This chapter addresses some of the fundamental theory behind photonics as well as some more advanced theory required to understand certain design choices made in this work. The chapter is taken mostly from the project thesis[7] with small adaptations. The first section describes Maxwell's equations along with their boundary conditions and limitations. Section 2.2 will describe coupled mode theory. Section 2.3 will explain silicon waveguides and modes. Section 2.4 will detail micro-ring resonators. Lastly section 2.5 will describe the theory behind spot-size converters.

2.1 Maxwell's equations

Maxwell's equations are a set of partial differential equations that describe how electromagnetic radiation propagates as a wave through a medium or vacuum. These have two major variants, the microscopic and the macroscopic set. The microscopic set uses total charge and total current including the atomic level charges and currents in materials. The macroscopic set circumvents the atomic level charges by defining two new auxiliary fields $\mathbf{D}$ and $\mathbf{H}$ which are defined as[9][10]

$$\mathbf{D}(\mathbf{r}, t) = \epsilon_0 \mathbf{E}(\mathbf{r}, t) + \mathbf{P}(\mathbf{r}, t) \tag{2.1}$$

$$\mathbf{H}(\mathbf{r},t) = \frac{1}{\mu_0}\mathbf{B}(\mathbf{r},t) - \mathbf{M}(\mathbf{r},t). \tag{2.2}$$

E is the electric field intensity, **D** the electric flux density or electric displacement, **H** the magnetic field intensity, **B** the magnetic flux density, **P** the polarization, **M** the magnetization, ϵ the permittivity, and μ the permeability of vacuum. The bold typeset is used to signify vectors. In linear materials these have the consecutive relations

$$\mathbf{D} = \epsilon\mathbf{E} \tag{2.3}$$

$$\mathbf{H} = \frac{\mathbf{B}}{\mu}. \tag{2.4}$$

Maxwell's equations are an approximation to the fundamental theory of quantum electrodynamics[11]. This thesis will use and describe the macroscopic set. The macroscopic set of Maxwell's equations in differential form is as follows

$$\nabla \times \mathbf{H} = \mathbf{J} + \frac{\partial \mathbf{D}}{\partial t} \tag{2.5}$$

$$\nabla \times \mathbf{E} = -\frac{\partial \mathbf{B}}{\partial t} \tag{2.6}$$

$$\nabla \cdot \mathbf{D} = \rho \tag{2.7}$$

$$\nabla \cdot \mathbf{B} = 0 \tag{2.8}$$

where J is the current density and ρ the electric charge density. Equation (2.5) was originally Ampère's law

$$\nabla \times \mathbf{H} = \mathbf{J} \tag{2.9}$$

stating that a magnetic field can be generated by an electric current. Maxwell added a correction stating that a magnetic field can also be generated by a changing electric field[12]. This along with (2.6) explains how a self-sustaining electromagnetic wave can travel through empty space. Equation (2.6) is actually Faraday's law, but is more restrictive than the original law, which is

$$\Phi_B = \iint\limits_{\sum(t)} \mathbf{B}(\mathbf{r},t) \cdot d\mathbf{A}. \tag{2.10}$$

It states that a time varying magnetic field induces an electric field. Equation (2.7) is Gauss' law describing the relation between an electric field and the charges that cause it and relates the electric flux through any closed Gaussian surface to the enclosed electric charge. The last of Maxwell's equations (2.8) states that there are no "magnetic charges" but that the magnetic field from materials is generated from dipoles and that the magnetic field lines are either loops or extend to infinity and back[13].

2.1.1 Boundary conditions

To be able to solve Maxwell's equations for a system consisting of several materials there must be some boundary conditions in place for the boundaries between the materials. For two dielectrics, assuming they are lossless, the conditions are[14][15]

$$E_{1t} = E_{2t} \tag{2.11a}$$
$$H_{1t} = H_{2t} \tag{2.11b}$$
$$D_{1n} = D_{2n} \tag{2.11c}$$
$$B_{1n} = B_{2n} \tag{2.11d}$$

where the notation 1 and 2 means material 1 and material 2, and the notation t and n means the tangential component and the normal component, respectively. These equations mean that the tangential component of the **E**-field and the normal component of the **B**-field are continuous across the boundary.

At the interface between a dielectric and a perfect conductor the conditions are given by[14][15]

$$E_{1t} = 0 \quad E_{2t} = 0 \tag{2.12a}$$
$$\mathbf{a}_{n2} \times \mathbf{H}_1 = \mathbf{J}_s \quad H_{2t} = 0 \tag{2.12b}$$
$$\mathbf{a}_{n2} \cdot \mathbf{D}_1 = \rho_s \quad D_{2n} = 0 \tag{2.12c}$$
$$B_{1n} = 0 \quad B_{2n} = 0 \tag{2.12d}$$

This means that since a perfect conductor is a material with surface charges, the **H**-field and **D**-field are discontinuous across the boundary.

2.1.2 Solving Maxwell's equations

Maxwell's field equations are a set of partial differential equations which means all methods for solving PDEs apply to Maxwell's equations as well. Analytical solutions include such methods as separating variables[16], Fourier analysis[17], and more. PDEs can become too complex to solve analytically, in those cases a numerical method can be used. One of the more common numerical methods is the finite element method.

2.1.3 Limitations

As mentioned earlier, Maxwell's equations are an approximation to the fundamental theory of quantum electrodynamics and can be quite noticeably inaccurate. For instance for extremely strong fields or extremely short distances some of Maxwell's equations need to be supplemented by terms of field components in higher powers[18]. Maxwell's equations describes electric and magnetic fields and as such have no way to describe singular photon travel and its randomness. Therefore any phenomena involving individual photons such as photoelectric effect require the extension theory of quantum electrodynamics[19].

2.2 Coupled mode theory

Coupling is the phenomenon occurring when two or more waveguides are closely spaced. Coupling between two waveguides means that the modes from waveguide 1 move over to waveguide 2 and vice versa. This happens because the mode's evanescent tail – the part of the field that is in the cladding, decaying exponentially – touches the other waveguide and transfers the field strength to the other waveguide. A mode describes the field distribution of a wave in a waveguide and is discussed in detail in section 2.3.2. The coupled modes are the ones that couple between the waveguides.

The coupled mode equations can be derived from perturbation theory. From [20] it is assumed that the electromagnetic fields of the coupled waveguide can be expressed as the sum of the eigenmodes in each waveguide

$$\tilde{\mathbf{E}} = A(z)\tilde{\mathbf{E}}_1 + B(z)\tilde{\mathbf{E}}_2\tilde{\mathbf{H}} = A(z)\tilde{\mathbf{H}}_1 + B(z)\tilde{\mathbf{H}}_2 \tag{2.13}$$

where the subscripts 1 and 2 denote waveguides 1 and 2, and A(z) and B(z) are the amplitudes of the fields in waveguides 1 and 2, respectively. Using Maxwell's equations and some vector relations the following expression is derived

$$(\mathbf{u}_z \times \tilde{\mathbf{E}}_1)\frac{dA}{dz} + (\mathbf{u}_z \times \tilde{\mathbf{E}}_2)\frac{dB}{dz} = 0 \tag{2.14}$$

$$\begin{aligned}(\mathbf{u}_z \times \tilde{\mathbf{H}}_1)\frac{dA}{dz} - j\omega\epsilon_0(N^2 - N_1^2)A\tilde{\mathbf{E}}_1 \\ +(\mathbf{u}_z \times \tilde{\mathbf{H}}_2)\frac{dB}{dz} - j\omega\epsilon_0(N^2 - N_2^2)B\tilde{\mathbf{E}}_2 = 0,\end{aligned} \tag{2.15}$$

where ω denotes angular frequency and ϵ_0 denotes permittivity in vacuum, and N_1 and N_2 denote refractive index in waveguide 1 and 2, respectively. N^2(x,y) is the refractive index distribution in the entire coupled waveguide. Equations (2.14) and (2.15) are substituted into the integrals

$$\iint_{-\infty}^{\infty} \left[\tilde{\mathbf{E}}_1^* \cdot (2.15) - \tilde{\mathbf{H}}_1^* \cdot (2.14)\right] dxdy = 0 \tag{2.16}$$

$$\iint_{-\infty}^{\infty} \left[\tilde{\mathbf{E}}_2^* \cdot (2.15) - \tilde{\mathbf{H}}_2^* \cdot (2.14)\right] dxdy = 0 \tag{2.17}$$

This eventually becomes[20]

$$\frac{dA}{dz} + c_{12}\frac{dB}{dz}e^{-j(\beta_2-\beta_1)z} + j\chi_1 A + j\kappa_{12}Be^{-j(\beta_2-\beta_1)z} = 0 \tag{2.18}$$

$$\frac{dB}{dz} + c_{21}\frac{dA}{dz}e^{+j(\beta_2-\beta_1)z} + j\chi_2 B + j\kappa_{21}Ae^{+j(\beta_2-\beta_1)z} = 0 \tag{2.19}$$

with β being the propagation constant of the respective materials and κ, c and χ defined as

$$\kappa_{pq} = \frac{\omega\epsilon_0 \int_{-\infty}^{\infty}\int_{-\infty}^{\infty} (N^2 - N_q^2)\mathbf{E}_p^* \cdot \mathbf{E}_q dxdy}{\int_{-\infty}^{\infty}\int_{-\infty}^{\infty} \mathbf{u}_z \cdot (\mathbf{E}_p^* \times \mathbf{H}_p + \mathbf{E}_p \times \mathbf{H}_p^*)dxdy} \tag{2.20}$$

$$c_{pq} = \frac{\int_{-\infty}^{\infty}\int_{-\infty}^{\infty} \mathbf{u}_z \cdot (\mathbf{E}_p^* \times \mathbf{H}_q + \mathbf{E}_q \times \mathbf{H}_p^*)dxdy}{\int_{-\infty}^{\infty}\int_{-\infty}^{\infty} \mathbf{u}_z \cdot (\mathbf{E}_p^* \times \mathbf{H}_p + \mathbf{E}_p \times \mathbf{H}_p^*)dxdy} \tag{2.21}$$

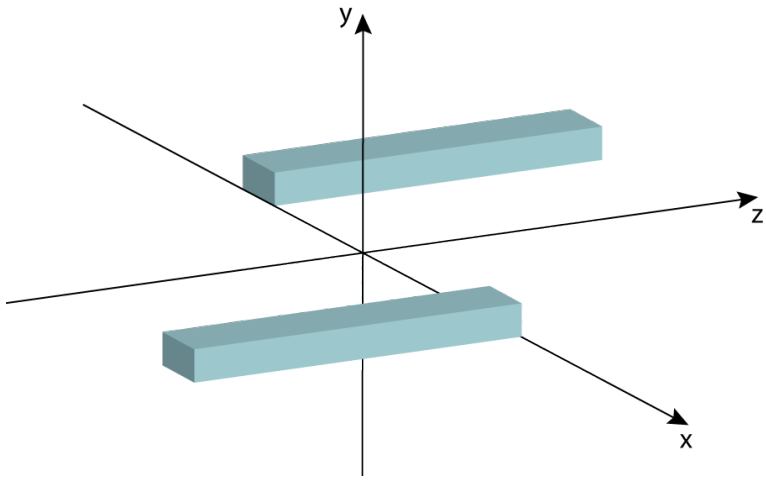

Figure 2.1: *Two waveguides separated in x-direction with ends at the same z-coordinate. In this instance c_{pq} is equal to zero. Figure inspired by similar figure in [20]*

$$\chi_p = \frac{\omega\epsilon_0 \int_{-\infty}^{\infty}\int_{-\infty}^{\infty} (N^2 - N_p^2)\mathbf{E}_p^* \cdot \mathbf{E}_p dxdy}{\int_{-\infty}^{\infty}\int_{-\infty}^{\infty} \mathbf{u}_z \cdot (\mathbf{E}_p^* \times \mathbf{H}_p + \mathbf{E}_p \times \mathbf{H}_p^*)dxdy}, \tag{2.22}$$

where (p,q) can be either (1,2) or (2,1), denoting the eigenmodes of waveguides 1 and 2. In most cases both c_{pq} and χ_p are assumed to be zero, however they should be included in strict analysis[20]. κ_{pq} is the coupling coefficient of two parallel waveguides in close proximity to each other. c_{pq} represents the coupling coefficient between the ends of the waveguides(ref. figure 2.1), the overlapping coupling coefficient. Since in figure 2.1 the ends are neither facing nor very close c_{pq} is naturally zero, or at least very close to zero. χ_p is the self-coupling coefficient. The self-coupling is caused by the waveguide perturbation in the coupling region. The coupling effect that happens between two close waveguides can be analysed by investigating the interference phenomena between the even and odd modes. Sufficiently separated, each of these two waveguides – properly constructed – will have only one guided mode. Spacing the waveguides closer together, optical power will begin coupling between them. Because of the

coupling effect these two single mode waveguides now possess two modes, an even and an odd mode, illustrated in figure 2.2.

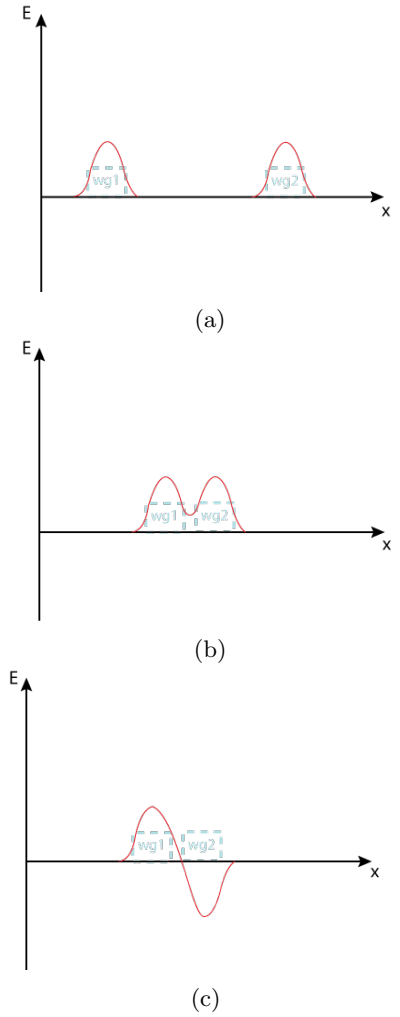

Figure 2.2: *Electric field amplitude as a function of the geometric dimension x. (a) Two single mode waveguides apart. (b) Even mode of two single mode waveguides close together. (c) Odd mode of two waveguides close together.*

If the higher-order modes are neglected the total electric field in the coupler can be approximated by summation of the even and odd modes[20], what some would call even and odd "supermodes".

$$E(x,z) = E_e(x)e^{-j\beta_e z} + E_o(x)e^{-j\beta_o z} \tag{2.23}$$

where $E_e(x)$ and β_e denote the electric field and propagation constant of the even mode, and $E_o(x)$ and β_o denote the odd mode, respectively. The amplitude of the electric field at z is given by

$$|E(x,z)| = |E_e(x) + E_o(x)e^{j(\beta_e-\beta_o)z}| \tag{2.24}$$

If the incident field is coupled to waveguide I at z = 0 then the distance at which the field is fully coupled to waveguide II is[20]

$$L_c = \frac{\pi}{\beta_e - \beta_o} \tag{2.25}$$

This gives a coupling coefficient of

$$\kappa = \frac{\pi}{2L_c} = \frac{\beta_e - \beta_o}{2} \tag{2.26}$$

If the waveguides are not symmetrical, the propagation constants of the waveguides will be different and there will be a phase mismatch, δ. The phase mismatch would cause higher coupling losses, but can be counteracted with e.g. a phase-shift grating. Note that while phase-matched coupling ($\delta = 0$) is always symmetric ($\kappa_{12} = \kappa_{21}^*$), symmetric coupling is not necessarily phase-matched.[21]

2.3 Silicon Waveguides

An optical waveguide is a structure that confines an electromagnetic field in the optical spectrum, guiding the wave from end to end[22]. An optical waveguide can either be a mirror waveguide or a dielectric waveguide, which can be either planar or a strip. Since mirror waveguides are not addressed in this thesis only dielectric waveguides will be discussed.

Silicon photonics is one of the most common photonic integration platforms due to the fact that it has a very high index contrast and that most of the fabrication technology already exists through CMOS technology[2][1]. Because of the large

index contrast silicon allows for very small features, reducing the footprint of photonic integrated circuits. A high index contrast is especially needed when making very small ring resonators as they require small bend radiuses which in turn require strong confinement. Many ring resonator applications need a relatively large free spectral range, for which small rings are needed[2]. Silicon also exhibits other good optical properties like large optical damage threshold and thermal conductivity[23][1].

2.3.1 Dielectric waveguides

A dielectric waveguide is made from a core surrounded by cladding. The core material is a dielectric with high refractive index and the cladding material is usually an insulator with low refractive index. The higher the difference in refractive indices between the core and the cladding the higher confinement. Waveguiding will occur in the material with the highest refractive index, therefore it is important that this is the core. With high confinement a sharper angle of approach can be used without loss, giving a high numerical aperture. Only light incident from the side can excite guided modes in waveguides, light incident from the top or bottom will only be reflected or refract right through the structure.

Confinement factor The confinement factor of power in a waveguide is given by the ratio between the power in the core and the total power[24]. Defining the direction of propagation to be the z-direction, the confinement factor becomes

$$\Gamma = \frac{\iint_{core} |\langle S_z(x,y)\rangle| \, dxdy}{\iint_{-\infty}^{\infty} |\langle S_z(x,y)\rangle| \, dxdy} \tag{2.27}$$

as extracted and modified from [25]. Defining the middle of the core as zero in the x and y plane would make (2.27)

$$\Gamma = \frac{\int_0^{\frac{h}{2}} \int_0^{\frac{w}{2}} |\langle S_z(x,y)\rangle| \, dxdy}{\iint_0^{\infty} |\langle S_z(x,y)\rangle| \, dxdy} \tag{2.28}$$

where w is the core width, h is the core height, and $\langle S_z(x,y)\rangle$ is the z-component of the ensemble Poynting vector of the field propagating in the z-direction. The Poynting vector is the electromagnetic power flux[14]

$$\mathcal{S} = \mathbf{E} \times \mathbf{H}, \tag{2.29}$$

and the complex Poynting vector is[26]

$$\mathbf{S} = \frac{1}{2}\mathbf{E} \times \mathbf{H}^*. \tag{2.30}$$

Planar waveguides

A planar waveguide is a slab of dielectric material covered with a cladding material on the top and bottom. It is considered to be infinite in two dimensions, confining the field in the y-direction and guiding it in the z-direction. True infinitely wide waveguides aren't very practical, but they form a good basis for analysis of waveguides with rectangular cross sections[27].

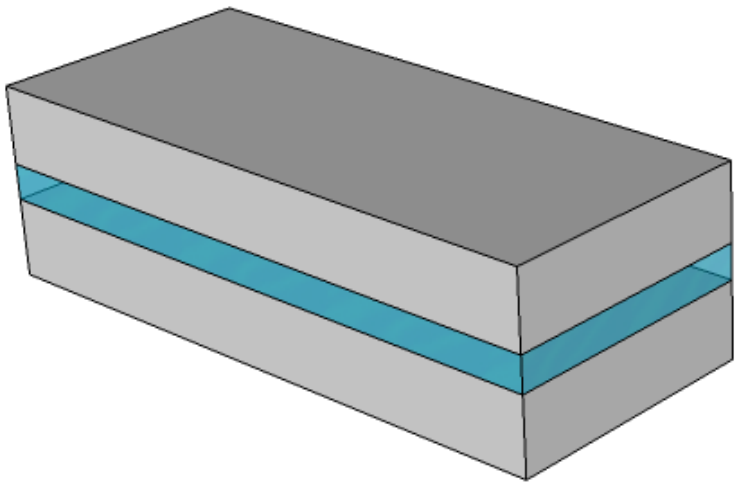

Figure 2.3: *A planar waveguide. The field is confined in only y-direction.*

Strip waveguides

Strip waveguides are finite in both the x and y directions, confining the field, and guiding it in the z-direction. The principles of a strip waveguide are the same as for a planar waveguide, but with a lengthier mathematical description[28]. They are more commonly wider on the sides parallel to the substrate but do not have to be. The field distribution in a rectangular waveguide is difficult to solve analytically. In the project thesis[7] the simulations on the strip waveguides were therefore solved by an approximate numeric solution called the finite element method.

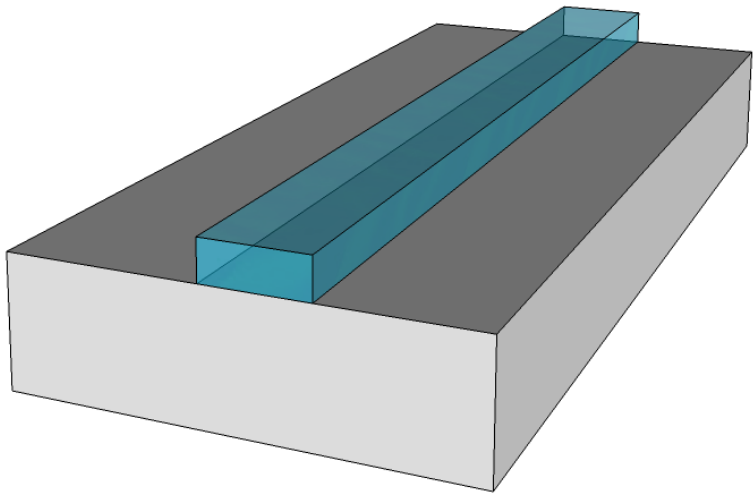

Figure 2.4: *A strip waveguide. The field is contained in both x- and y-directions.*

2.3.2 Modes

A mode is a spatial distribution of optical energy in one or more dimensions that remains constant in time. It is one of several electromagnetic fields that are solutions of Maxwell's wave equation. The following is mostly taken from [27].

$$\nabla^2 \mathbf{E}(\mathbf{r}, t) = \left[\frac{n^2(\mathbf{r})}{c^2}\right] \frac{\partial^2 \mathbf{E}(\mathbf{r}, t)}{\partial t^2} \tag{2.31}$$

where **E** is the electric field vector, n(**r**) is the index of refraction, and c is the speed of light in vacuum.

If we assume a planar waveguide and a monochromatic, uniform plane wave, the solution to (2.31) has the form

$$\mathbf{E}(\mathbf{r}, t) = \mathbf{E}(\mathbf{r})e^{i\omega t} \tag{2.32}$$

where ω is the radian frequency. Substituting (2.32) into (2.31) gives

$$\nabla^2\mathbf{E}(\mathbf{r}) + k^2n^2(\mathbf{r})\mathbf{E}(\mathbf{r}) = 0 \tag{2.33}$$

where k $\equiv \frac{\omega}{c}$. With the wave propagating in the z direction

$$\mathbf{E}(\mathbf{r}) = \mathbf{E}(x, y)e^{-i\beta z}, \tag{2.34}$$

β being the propagation constant, equation (2.33) can be written as

$$\frac{\partial^2\mathbf{E}(x, y)}{\partial x^2} + \frac{\partial^2\mathbf{E}(x, y)}{\partial y^2} + [k^2n^2(\mathbf{r}) - \beta^2]\mathbf{E}(x, y) = 0. \tag{2.35}$$

The partial differentiation with respect to y is zero since the waveguide is assumed to be infinite in the y direction and equation (2.35) is therefore written as

$$\frac{\partial^2E(x, y)}{\partial x^2} + (k^2n_j^2 - \beta^2)E(x, y) = 0, \qquad j = 1, 2, 3 \tag{2.36}$$

where E(x,y) is the Cartesian component of **E**(x,y). If $(k^2n_j^2 - \beta^2)$ is greater than zero, then the solution to (2.36) is sinusoidal. If $(k^2n_j^2 - \beta^2)$ is less than zero, the solution becomes exponential[27]. Figure 2.5 depicts a planar waveguide with the first three transverse electric modes sketched. TE_0 is called the zeroth order mode, TE_1 is called the first order mode and TE_2 is called the second order mode. They can be recognized by how many times the field crosses its zero-point. These modes are supported for values of β between kn_2 and kn_3[27]. In a strip waveguide the mode annotation is TE_{mn} where either m or n can be zero, but not both. For a strip waveguide where the horizontal sides are larger than the vertical sides the TE_{10} is the dominant mode. The dominant mode is the mode with the lowest cut-off frequency.

Propagation constant

The propagation constant is a recurring theme when talking about modes because each mode corresponds to a certain value of β. β is discrete in nature for all

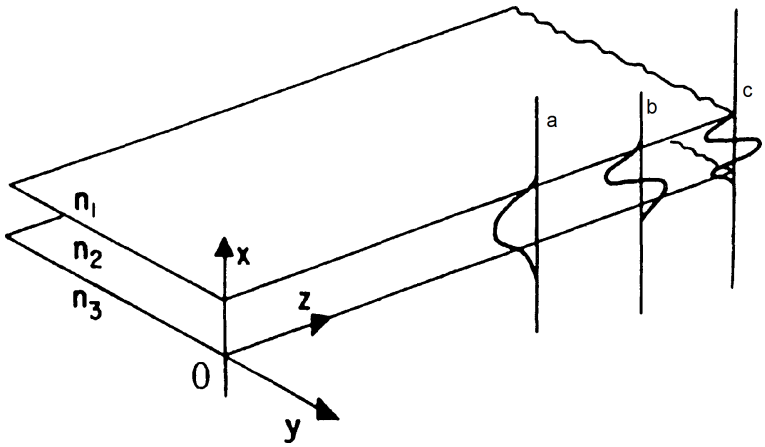

Figure 2.5: *A three layer planar waveguide with the (a) TE_0, (b) TE_1 and (c) TE_2 modes illustrated. n_1, n_2, and n_3 denotes the refractive indexes of the respective layers. Figure modified from [27].*

propagating modes, meaning only discrete values of β are allowed in the range between kn_3 and kn_2. These values correspond to TE_j and TM_k (with j = 0,1,2,... and k = 1,2,3,...) in planar waveguides. The reason only discrete values of β are allowed in the $kn_3 \leq \beta \leq kn_2$ region is because wavefronts travelling from one interface to the other must have a total phase change of 2π, else the wave will decay due to destructive interference as it travels through the waveguide[27]. The number of modes allowed that can be supported by the waveguide are dependent on the geometrical size, the frequency and the refractive indices of the core and cladding materials. From this follows the conclusion that for specific geometrical sizes and refractive indices there is a cut-off frequency ω_c below which no guided modes can exist. Even though β is discrete for the guided modes, it has continuous values for the radiative modes as shown in R.G. Hunsberger[27].

TE vs TM modes

The difference between a transverse electric (TE) and a transverse magnetic (TM) mode is that for the TE mode the electric field is oscillating parallel to the top and bottom of the waveguide, and for the TM mode the electric field

is oscillating normally with respect to the top and bottom of the waveguide.

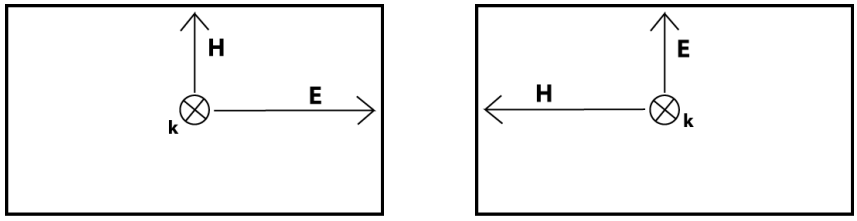

(a) *The TE mode.* (b) *The TM mode.*

Figure 2.6: *Illustration of the field oscillation of the modes at the end of a strip waveguide.* ***H*** *is the magnetic field vector,* ***E*** *the electric field vector and* ***k*** *is the wave vector.*

In reality the modes usually aren't pure TE or TM, but a TE-"like" or TM-"like" mode called quasi-TE and quasi-TM modes. Because of its superior confinement and therefore also small bending loss the TE mode is the most common preferred mode of operation[29][4]. For some applications however, it is best to use TM modes[30]. This is because of their smaller scattering loss due to lesser overlap with the sidewalls[2], and lower back reflections[31]. De Heyn et al.[31] also claim that TM based microring resonators have shown a higher quality factor than their TE based counter parts. Chin et al.[32] show that microring resonators are polarization dependent because the coupling length for TM modes are shorter than for TE, and Headley et al.[33] demonstrate that a resonator can be made polarization independent by having the modes couple back and forth a different number of times for TE and TM. De Brabander et al.[34] show that the temperature sensitivity in pressure sensing using micro-ring resonators can be avoided by using both the TE and the TM modes. As mentioned before in this thesis we are using the TE mode. This is because of the higher confinement needed for small radii.

2.4 Micro-ring resonators

A micro-ring resonator is a circular waveguide placed in close proximity to a waveguide such that a propagating wave from the waveguide couples into the ring.

Depending on the design of the ring certain wavelengths experience constructive interference within the ring, resonating. After multiple round trips, the intensity builds up and the wave either couples back to the original waveguide or to another waveguide if multiple are in close proximity to the ring. The wavelengths the ring is not designed for will experience considerable losses due to decreased confinement and destructive interference. Micro-ring resonators are proving themselves to be excellent building blocks for photonic circuits[35]. Thus far micro-ring resonators have been implemented as filters[32][29][36], dispersion compensators[29], sensors [37][34], and in lasers[38].

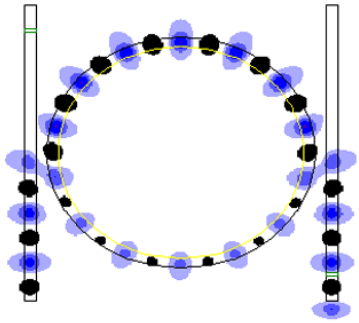

Figure 2.7: *An optical ring resonator with waveguides on each side. All power is transmitted to the ring from the leftmost waveguide which means that the requirement for critical coupling is met. Figure taken from [?]*

Critical coupling means that the propagating wave coupled completely from the waveguide to the resonator. The resonator filters out all wavelengths it was not designed for and couple the remaining wavelengths back into the straight waveguide. The wavelengths that resonate in the ring are the ones that have a phase multiple of 2π after a round trip. This means that the wavelength of light fits a whole number of times inside the optical length of the ring[2]

$$\lambda_{res} = \frac{n_{eff}L}{m}, m = 1, 2, 3... \tag{2.37}$$

where L is the round trip length and m is the number of wavelengths oscillated during one round trip. The effective index, n_{eff}, for a particular guided mode is mostly dependent on the material of the core and those in close proximity to the core. Therefore it is sensitive to small changes in material composition around it. This can be exploited in sensors by measuring the resonant frequency based on how close a different material is to the ring functioning as a pressure sensor. The resonator can also function as a chemical sensor, measuring the resonant frequency based on the material composition around the ring. De Vos et al.[37] shows that by scaling down the micro-ring resonator they are able to sense a coverage of 0.7 fg molecular layer.

2.4.1 Free spectral range

As stated earlier, a micro-ring resonator has multiple resonance wavelengths. The free spectral range in a ring resonator is the wavelength range between two resonances[2]

$$FSR = \frac{\lambda^2}{n_g L}. \tag{2.38}$$

Since there is strong confinement in SOI, very sharp bends can be realised which in turn increases the potential FSR in resonators made of SOI. This is desirable in many applications. FSR is dependent on the group index n_g which is dependent on effective index and takes into account the dispersion of the waveguide[2]

$$n_g = n_{eff} - \lambda_0 \frac{dn_{eff}}{d\lambda}. \tag{2.39}$$

2.4.2 Finesse and Quality factor

As previously mentioned there are losses in a ring resonator which are exploited to let through light at a certain wavelength, however even the resonant frequencies experience losses in the ring[2]. This means that there are different qualities for different resonators and these are measured through finesse and quality factor

$$Finesse = \frac{FSR}{FWHM} \tag{2.40}$$

$$Q - factor = \frac{\lambda_{res}}{FWHM} \tag{2.41}$$

where FWHM is the full width half maximum of the resonance spectrum. For an all-pass ring resonator, where one straight waveguide couples to a ring and then couples back to the same straight waveguide, the FWHM is defined as

$$FWHM = \frac{(1 - ra)\lambda_{res}^2}{\pi n_g L \sqrt{ra}} \tag{2.42}$$

where a is the single-pass amplitude transmission and r is the self-coupling coefficient, including coupling loss and propagation loss in the ring[2]. It is related to the power attenuation coefficient, α, as

$$a^2 = e^{-\alpha L}. \tag{2.43}$$

Q-factor and finesse can then be rewritten as

$$Q - factor = \frac{\pi n_g L \sqrt{ra}}{\lambda_{res}(1 - ra)} \tag{2.44}$$

$$Finesse = \frac{\pi \sqrt{ra}}{1 - ra}. \tag{2.45}$$

Finesse is defined as the number of round trips within a factor of 2π it takes for the light to reduce its energy to $\frac{1}{e}$ of its initial value. The definition of Q-factor is that it is the number of oscillations of the field before the energy depletes to $\frac{1}{e}$[2]. The higher the Q-factor, the lower the losses of your device. A good Q-factor is about 50 000. It is also worth mentioning that there are two different Q-factors, loaded and unloaded. Loaded simply means that the ring is close enough to a waveguide to have coupling and because of coupling losses the loaded Q-factor is always less than the unloaded. When talking about Q-factor the loaded Q-factor is usually implied[2].

2.4.3 Sensitivity

Ring resonators are sensitive to a multitude of effects, e.g. temperature, physical deformation and compositional changes. This makes them very attractive in sensing applications[2]. The sensitivity comes from the resonance wavelength dependence on the optical round trip length and the losses accumulated. Changes in the effective index n_{eff} of the mode resonating in the ring causes shifts in the resonance wavelength λ_{res}. From (2.37) we get

$$\Delta\lambda_{res} = \frac{\Delta n_{eff} L}{m}, \qquad m = 1, 2, 3... \tag{2.46}$$

where m is the number of oscillations the wave experiences during one round trip. Physical deformation alters round trip length and effective index through geometrical changes. The refractive index of both the core and cladding material is also a function of temperature, and therefore the effective index will vary depending on temperature. Compositional changes will alter the material composition of the cladding altering the effective index. The change in λ_{res} in turn influences n_{eff} turning (2.46) into a first order approximation found in Bogaerts et al.[2]

$$\Delta\lambda_{res} = \frac{\Delta_{env} n_{eff} \lambda_{res}}{n_g}. \tag{2.47}$$

$\Delta_{env} n_{eff}$ is the shift in effective index after an environmental change and can be expressed as[2]

$$\Delta_{env} n_{eff} = c \int \Delta\epsilon \mathbf{E}_\nu \cdot \mathbf{E}_\nu^* dxdy. \tag{2.48}$$

A thorough analysis of effective index sensitivity for environmental changes can be found in Tiefenthaler & Lukosz[39].

2.4.4 Losses

The ring resonator system has many different sources of losses. Dispersion from the atomic structure of the waveguides and the surface roughness, along with material absorption are called propagation losses[2]. Additionally there are losses from absorption and dispersion in the coupling region, inferior confinement in the sharp bends of the resonator, destructive interference from the reflections from the resonator, and backscattering from imperfections in the materials[2]. Q-factor and finesse are intrinsically connected to the losses of the system. Propagation losses are minimized by using high quality SOI and good processing techniques, and reflections and backscattering are negligible. Therefore to increase Q-factor the most important losses to minimize are usually the bend losses[2]. Bogaerts et al.[2] suggest the use of adiabatic bends as opposed to circular bends. Another technique often used to reduce bend loss is to increase the round trip length of the resonator, however even though increasing the round trip length reduces the bend loss it also increases the propagation losses, which is also pointed by Bogaerts et al.[2]. For this reason the reduction in bend loss gives a lesser increase in Q-factor.

Bogaerts et al.[2] mention that the resonance is also dependent on losses accumulated. What is meant by this is that a phase change in the field is caused by the losses in the coupling region, and the dispersion from surface roughness in the ring. This phase change is what makes a change in the resonant wavelength. So even though the resonator has been made to meet specifications provided by theory and simulations, it still may not be usable for the chosen wavelength. This can be circumvented by tweaking the other parameters that the resonance is dependent on, e.g. temperature.

2.5 Spot-size converter

Coupling from external optical fibres to silicon waveguides is a challenge as the cross section of the silicon waveguide core is 500 × 220 nm^2 while the mode size of an optical fibre is much greater at a few microns. Typical losses from optical fibre to silicon waveguide could be as much as 20 dB[40]. Shoji et al.[40] proposed using a long inverse silicon taper and deposit a larger polymer waveguide on top of the taper to lower the coupling losses. The larger polymer waveguide is then called a spot-size converter. A typical design for a wavelength of 1550 nm, the tip of the inverse taper should optimally be less than 100 nm, to limit the amount of reflections, and the spot-size converter should have dimensions 3 × 3 μm^2 with a 2.5% index contrast to the cladding[3].

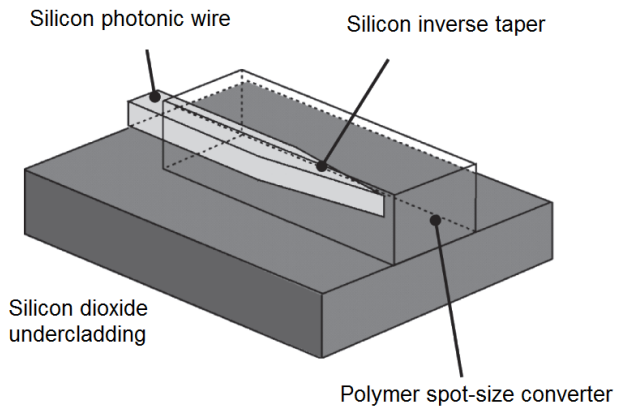

Figure 2.8: A polymer spot-size converter on a silicon inverse taper. Figure reprinted and adapted from [3].

Other coupling methods have been tested, e.g. coupling gratings[8], however they are much more difficult to realise for integrated chip design.

Chapter 3

Equipment and Fabrication

This chapter will give the full details of the specific equipment that has been used in making the structures in this master thesis. The chapter will also introduce some challenges that arise during processing.

3.1 Scribing and breaking

Usually a wafer of 2 or more inches will need to be diced into several smaller dies. This can be done before or after any step in the fabrication process. When manufacturing a proven design this is usually not done until the dies are about to go trough the packaging process as it is usually more convenient and economical to process as many chips as possible at the same time. When doing research, depending on which process step is being explored, dicing is done earlier in the process. This gives more dies available to vary the parameters for the experiment.

Dicing can be done either by sawing through the wafer directly with a thin saw blade or by going through a scribing and breaking process. Scribing means to have a sharp tip scribe a dent in the wafer along one of the crystal axes making

it easier to break the wafer at the desired location using a hammer applied to the backside of the wafer. This work uses a scribing and breaking process.

The scriber being used when doing the work for this thesis is the Dynatex DX-III. It works by placing the sample on a square piece of adhesive tape attached to two rings. The ring is placed on the scriber stage and locked in place by vacuum. The sample is then theta aligned horizontally such that the sample is scribed along the crystal axis $\langle 1\ 0\ 0 \rangle$. The DX-III can automatically scribe and break from a set of parameters and a predetermined die size, or manually scribe and break by using the interactive mode. For this thesis the automatic mode was used to scribe whole wafers and the manual mode was used when scribing and breaking for cross-section characterization. The scribe parameters that can be set by the users are given in table 3.1 as well as the values used for the work done for this thesis, while the break parameters are given in table 3.2. The step size is 10 mm in X-direction and 6 mm in Y-direction. The scriber uses a diamond tip to scribe a line across the sample along the crystal plane, and then the sample is broken by an impulse bar applied directly beneath the scribed lines. If the theta alignment is satisfactory along the crystal plane very clean breaks can be achieved.

When scribing the etched samples to inspect the profiles of the structures manual mode is used. The sample is scribed starting the line ∼3-400 μm past the structures. Then the sample is unloaded and turned 180° before being loaded again. A new scribe line is then made on the other side of the structures, aligned with the first line. The sample is then broken along the two aligned scribe lines resulting in a break across the structures without destroying the surface.

Table 3.1: Parameters used for scribing 250μm thick silicon samples.

Parameter	X & Y
Method	Continuous
Impulse bar height	0 μm
Extension	90 μm
Scribe force	1600 cnts
Scribe angle	36o
Scribe speed	6 $\frac{mm}{s}$
Approach speed	1 $\frac{mm}{s}$

Table 3.2: Parameters used for breaking $250\mu m$ thick silicon samples.

Parameter	X & Y
Method	Anvil
Air pressure	80 kPa
Anvil Height	0.426 mm
Gap	0.376 mm
Dwell time	0.1 s
Cycle time	0.2 s

3.2 Spin coating and resist

Electron beam lithography uses a resist spun upon the wafer to make a mask. The resist consists of a polymer in a solvent. The type of polymer and solvent varies and the ratio between polymer material and solvent can be varied depending on which mask thickness is needed. The resist used in this master project is polymethyl methacrylate (PMMA).

Any particles on the wafer should be removed prior to spinning on the resist. This means that it must be cleaned with acetone to remove any particles and grease on the wafer, then with ethanol and isopropanol to remove the acetone before it dries and leaves residues on the wafer. Optionally the isopropanol can be washed off with deionized water and dried with nitrogen gas. Lastly the wafer must be on a 200°C hotplate for 20 minutes to undergo a dehydration bake. This is necessary even if the optional step of washing with water was not done. The dehydration bake is very important to get the resist to stick properly to the wafer. The PMMA is spun on the wafer using a spin coater (it is a good idea to spray the wafer with nitrogen gas just before putting on the liquid resist to make sure there are no contaminants on the wafer). The thickness is dependant on the polymer/solvent ratio as well as the speed at which the resist is spun on in the spin coater. After the resist has been spun on the excess resist on the backside of the wafer should be removed, usually with acetone, to make the backside of the wafer flat. If the wafer is slightly angled when exposing, some problems may occur with the write field alignment. After cleaning the backside of the wafer the wafer and the mask must go through an annealing step. This is done on a hotplate at 180°C for 60 seconds. The PMMA datasheet recommends 60-90 seconds, however throughout this work this step is kept at 60 seconds for consistency. When the anneal is done, the wafer is moved to a cold plate to cool it down. This is to ensure that the annealing step does not last longer than the designated time.

Figure 3.1: *Illustration of the edge bead effect, exaggerated for illustration purposes. The blue area represents resist on top of silicon.*

3.2.1 Uniformity

Good resist uniformity means that the resist has the same thickness everywhere on the wafer. This is important because the resist thickness dictates the exposure dose. Usually, because of surface effects, the resist gathers around the edge to form an unavoidable hill which is why patterning at the edge of the wafer is usually avoided. The edge bead is illustrated in figure 3.1. If the resist is spun on at too low velocities or for too short a time the uniformity suffers not just along the edges. For a given polymer/solvent mixture minimum thickness is reached at around 4000 RPM. If the blend is made such that the desired thickness is the minimum thickness of the blend, high RPM is needed. This in turn provides a higher probability of good uniformity.

3.2.2 Defects

Even though great care has been taken in handling and cleaning the sample, some microscopic particles might still have contaminated the resist. These defects in the mask can be critically disruptive of the pattern. When using a small pattern as the one used in this master project the defects can be avoided by choosing the location of the pattern carefully. However in the industry where available area on the die is a precious commodity, almost all of the wafer is used making it very difficult or impossible to avoid areas with defects.

Summary check-list

1. Clean sample
2. Dehydration bake
3. Spin coat
4. Clean backside
5. Anneal
6. Check uniformity and look for defects

3.3 Electron Beam Lithography

Electron beam lithography(EBL) is a direct write lithography process where the pattern printed into the photoresist is determined by a pattern defined in the software. As the name suggests the process accelerates electrons towards the sample to activate the resist covering the sample. The beam is scanned across the sample according to the pattern, and as such the process is slower than optical lithography. The feature size limit depends on the configuration of the stage and beam as well as the hardware. The quality of the beam is controlled by the column set up as well as the alignment of three electromagnetic lenses called deflectors. The EBL instrument used in the work done for this thesis consists of a Hitachi S-4300 Schottky Field Emission SEM, and a Raith Quantum pattern generator and stage. The position of the stage is determined using laser interferometry. Thanks to the work done by Kai M. Beckwith[41] parallel to the work done for this thesis a greater understanding of the configuration options was gained.

3.3.1 Setup

The beam current is determined by the acceleration voltage V_{acc}, the current I_e, and the external voltage V_{ext} as well as the column setup. Throughout the work these were held at 20kV, 14-15 μA, and 1.5kV, respectively. The working distance for the column was set to 6.9 mm. The beam current is measured by aiming the electron beam at the Faraday cup located on the stage. The beam current was usually measured to be $\sim$40 pA with these settings. This current is of course

measured to be negative as the beam is made up of electrons. The trade-offs as listed by Beckwith[41] are as follows. Increasing the working distance will increase the depth of focus, while decreasing it will give less aberrations and better resolution. Increasing the beam current will increase the writing speed while decreasing it will reduce the probe size and increase the resolution. The acceleration voltage will also determine the at which velocity the electrons hit the sample. The electron velocity will in turn determine the broadness of the scattering in the resist. These trade-offs are also indicated in [42].

Before exposure can be done the user must ensure perfect focus, astigmatism, and aperture centering. This is done by finding a small feature on the sample and zooming in, focus and adjust astigmatism and aperture, zoom in further and reiterate. To investigate the focus and astigmatism a contamination dot can be burned into the resist at a spot which will not contain any features. If a perfectly round contamination dot is achieved in less than 5 seconds it is safe to continue with the exposure.

The Raith software Elphy Plus provides angle and origin correction. Angle correction is done by defining the two bottom corners of the sample. The software then calculates the angle and applies it to the relative uv-coordinates. The origin correction is done by moving the stage to a select location and defining the centre of the image as the origin. Lastly the write field must be defined and a write field alignment process must be completed, which will also define at which magnification the exposure will be carried out. The write field alignment procedure is done manually by having the stage move slightly over a selected feature and scan the beam over a defined area from four points. A point on the feature is identified and the middle of the image is moved to the selected spot. When this has been done for all four write fields, the scan area is decreased and the process is reiterated. As waveguides are very sensitive to roughness the best possible write field alignment is required. To achieve this write field alignment with the smallest scan area possible for the selected write field must be reiterated several times. When the middle of all the write fields are in the same selected spot the alignment process is finished. The trade-off as listed by Beckwith[41] is that increased write field size will increase the write speed, while decreasing it will increase the precision.

3.3.2 Scattering effects

When the electrons enter the sample they will scatter readily from atomic collisions and as silicon is a harder material than PMMA backscattering events will also occur. The scattering and backscattering will broaden the lines and contribute to the total dose for the affected areas in the resist[42]. At low acceleration voltages the electrons will be more susceptible to scattering but travel shorter distances after scattering. At high acceleration voltages the electrons will be less susceptible to scattering but travel longer distances after scattering. The ultimate resolution is however not set by electron scattering, but by a combination of other factors which will not be listed here. These are however summarized in [42] for the interested reader. Scattering also lead to proximity effects. The proximity effect is the contribution of scattered electrons from features in close proximity to each other. These will increase the dose received by affected areas and can, in patterns containing several closely spaced features, significantly degrade the pattern[42].

3.3.3 Resist

The resists used for EBL at the NTNU NanoLab are based on polymethyl methacrylate(PMMA). They are 950PMMA A9 and A2 where A denotes that anisol has been used as the solvent for the solution and the number following denotes the percentage amount of solids. A higher percentage of solids will provide a thicker resist layer assuming the same spin process has been used. The resist can either be positive, meaning that the exposed resist will be removed in the developer, or negative, meaning that the unexposed resist will be removed in the developer. The developer used is nine parts isopropyl alcohol(IPA) and one part deionized(DI) water which gives good resolution. In the work done for this thesis the PMMA resist is used as the etch mask. The reason for this is that the removal of a hard mask such as silicon dioxide or chromium may introduce further roughness.

3.4 ICP-RIE

ICP-RIE, or inductively coupled plasma reactive ion etching, utilizes physical as well as chemical etch types. A physical etch type means that atoms on the sample

are dislodged by incoming ions. A physical etch is considered an anisotropic etch since the ions will only dislodge atoms in their path, leaving a straight sidewall if undisturbed. The etch rate of a purely physical etch is determined by the weight of the atoms on the sample, and the weight and speed of the incoming ions. A chemical etch type is an etch that utilizes chemical reactions between the etchant and the substrate to form liquid or gaseous compounds. A chemical etch is considered an isotropic etch meaning that if etchant is left at the bottom of a trench it will etch exposed reacting materials equally in horizontal and vertical directions. The etch rate in a purely chemical etch is determined by the availability of the etching radicals and the speed of the chemical reaction.

The instrument used in the work done for this thesis is an Oxford Instruments PlasmaLab System 100 ICP-RIE 180, which uses a combination of capacitive coupled plasma(CCP) and inductively coupled plasma to generate plasma. CCP is generated by applying a radio frequency voltage to anode and cathode plates[43]. This frequency is usually 13.56 MHz as this band is reserved for industrial use in the United States. The electrons in the plasma oscillate between the plates, colliding with the slower moving ions and causing further ionization. A capacitor is placed between the anode and the RF supply. Negative charges will accumulate on the plate resulting in a potential difference between the plasma and the plate called the self bias V_b. This will drive the ions in the plasma towards the anode, which is often called the table[43].

ICP is generated by applying the radio frequency inductively which results in a changing magnetic field[43]. This field in turn induces an electric field which circulates the plasma parallel to the CCP plates. Similarly collisions between electrons and ions cause further ionization. Electrons are lost to the grounded chamber walls which create a static voltage called the plasma voltage. A large coil surrounding the plasma chamber realizes the inductive coupling. Figure 3.2 shows a sketch of an ICP-RIE system indicating the positioning of the plates and the coil. The sketch is reprinted from [43]. This system allows the user to control the ion density without changing the energy of the ions incident on the sample, which is clamped on the stage. The glow discharge is the region where energy from the gas particles is transferred to bound electrons. These electrons emit photons when returning to their original state, giving off a glow. The colour of the glow is dependent on the gas species and can be used as a diagnostic tool for changes in the plasma. The dark space is below the glow discharge region and is dark because electron depletion. This part of the plasma affect the incoming ions the most[43]. The incoming ions will scatter in this region and give a spread in energy and trajectory. These spreads are described by the ion energy

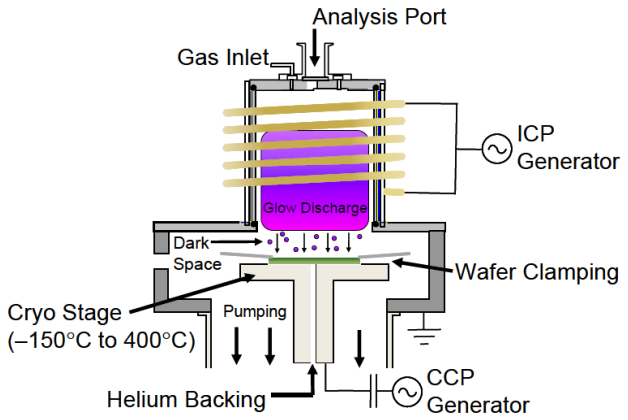

Figure 3.2: *Illustration of an ICP-RIE etching chamber and the processes it contains. Reprinted from [43].*

distribution function(IEDF) and the ion angular distribution function(IADF), respectively[43][44]. If the IADF is sharply curved it indicates that most of the ions travel in the same direction[44], therefore there are less scattering events in the dark region. However if the IADF is broad a greater amount of ions will be angled towards the sidewalls[43][44], removing any passivation layers and causing effects such as bottling[44]. Similarly a sharp IEDF curve will indicate that most of the ions have retained their energy upon arriving at the sample[44]. The IEDF indicates the amount of ions that can remove passivation layers and activate chemical reactions[43]. The IADF and IEDF can be controlled through the bias voltage V_b, the ion density, the gas composition, and the mean free path[43]. Since the samples used in this work are 10 mm $\times$ 6 mm they are too small to be clamped to the stage. Instead the samples were placed on a carrier wafer of either silicon or sapphire connected thermally by depositing Fomblin oil between the sample and the carrier wafer. It is important to keep the sample at a constant temperature as many of the processes during etching are temperature dependent.

Increasing the ICP power will increase the ion density in the plasma and increasing the CCP power will increase the incident energy of the ions. CCP power is often referred to as the forward power. Increasing the incident energy will increase the physical etch rate done by ion bombardment on the sample. Increasing

the ion density in the plasma will increase the physical etch rate as well as the chemical etch rate[43]. Along with ICP and CCP power the gas flow is also a significant parameter to the etch process. This work utilized a fluorine based etch using a combination of SF_6 and CHF_3 inserted into the chamber simultaneously. Fluorine radicals along with silicon form the volatile compound SiF_4[45], effectively removing the exposed silicon from the sample. CHF_3 supplies CF_i (i=1,2,3) radicals depositing a polymer layer on the sample[46]. This polymer layer will be removed by ion bombardment when depositing on the bottom of a trench however it will stay on the sidewalls where the ion bombardment is less frequent. This layer on will prevent fluorine radicals to reach the silicon and will prevent SiF_4 from diffusing out. An increase in the SF_6 gas flow rate will increase the generation of fluorine radicals increasing the etch rate. An increase in CHF_3 will increase the deposition rate of the polymer increasing the thickness of the polymer barrier. This will also decrease the etch rate as more ion bombardment is needed to remove the polymer at the bottom of the trenches. The sidewall profile can be controlled by adjusting the ratio of the etching and passivation gases[43].

3.4.1 Selectivity

The selectivity is a measure of the how fast one material is etched over another and is the ratio of the etch rates of the materials. A high selectivity means that etching occurs faster on the desired material than on the compared material[47]. The formula for selectivity between the substrate and the masking layer is as follows

$$\text{Selectivity} = \frac{\text{Etch rate of substrate}}{\text{Etch rate of mask}} \tag{3.1}$$

If the mask material has been chosen correctly the mask should have limited reaction with the gas chemistry, giving a good selectivity for the chemical etching process. However the selectivity between the mask and the substrate is usually considerably dependent on the amount of physical etch generated by an etching recipe. Increased ICP power leads to reduced selectivity due to an increase in ion density[43], and as previously increasing ion density increases the physical etch rate. The CCP power is the main method for controlling the physical etch rate, increasing the CCP power will increase the energy of the incident ions, increasing the physical etch rate and reducing selectivity.

During nanoscale etching, as done in this work, large etch rates and high selectivity is not needed[43]. Accuracy and straight sidewalls are more important.

Depending on the etch depth a selectivity of 5:1 is usually acceptable[43]. For this work a low selectivity PMMA etch mask was used, however an alumina mask made using resist lift off is a great alternative due to its higher selectivity, easy patterning, and electric insulation[43].

3.4.2 ARDE lag

ARDE, or aspect ratio dependent etch, refers to a non-uniformity of the etch caused by feature size. The aspect ratio is defined as the depth divided by the width of the feature. Many factors contribute to ARDE effects and a few along with possible causes are listed in [44] and [48]. ARDE lag refers to the aspect ratio dependency of the etch rate. A small feature is etched slower because of a depletion of the etching radicals or accumulation of reaction products at the bottom of high aspect ratio trenches, and is called micro-loading[44][48][8]. Micro-loading is caused by reduced ion flux at the bottom of the trench[48]. In the case of a large feature the etching radicals are consumed faster than they are transferred from the plasma and therefore etches the larger features more slowly. This is called macro-loading. It is indicated in [48] that ARDE lag can be minimized by increasing the process pressure, and other ARDE effects by using high SF_6 flow rates, using shorter etch times, low pressure and low CCP power. Silicon-on-insulator(SOI) and silicon-on-glass(SOG) wafers can be used to avoid the ARDE lag, however one significant concern is that notching occurs at the junction between the silicon and the oxide[48]. ARDE is a complex phenomenon and it is outside the scope of this work to attempt to explain all possible mechanisms involved.

3.5 Reflectometer

The reflectometer used in this work is a Filmetrics F20. The device uses spectral reflectometry in the 380 nm to 1080 nm wavelength range to measure film thickness, refractive index, and wave vector. Spectral reflectance works by measuring the background spectrum $I_{bkg}(\lambda)$, the reference reflectance spectrum $I_{ref}(\lambda)$, and then the reflectance spectrum of the desired thin film $I_{meas}(\lambda)$. For this work the reference is silicon and the thin film is PMMA. The total

reflectance $R(\lambda)$ is then calculated as shown[49]

$$R(\lambda) = \frac{I_{meas}(\lambda) - I_{bkg}(\lambda)}{I_{ref}(\lambda) - I_{bkg}(\lambda)} R_{ref}(\lambda) \tag{3.2}$$

where $R_{ref}(\lambda)$ is the theoretical reflectance of the reference sample. The total reflectance along with the reflected phase change is used to calculate film thickness, refractive index, and wave vector. The method is described in more detail in [49]. The device then determines a goodness of fit parameter denoted g which have is called g-factor in this thesis. The goodness of fit parameter is a number between 0 and 1 and indicates how well the measured reflectance spectrum compares to the theoretical spectrum, 1 being the perfect fit. The goodness of fit should not be less than 1 by more than a few decimals.

3.6 Profilometer

The Veeco Dektak 150 profilometer used in this work is a contact stylus profilometer. It uses a 12.5 μm diamond tipped stylus which is run across the sample measuring height differences. A profilometer is often used to measure roughness on a sample surface, however it can also be used to measure etch depths or thickness of a deposited film if an area has been left untouched by the process. The Dektak 150 has a vertical resolution of 1 Å.

3.7 Maskaligner

The Karl Süss MA6 maskaligner uses optical lithography at the UV wavelength of 365 nm called the i-line. The i-line is generated by a mercury arc lamp and has a critical dimension resolution of 0.35 μm[47]. To achieve the best resolutions the mask is pressed onto the sample. This is to minimize the effects of light diffraction along the mask edges. The mask is a glass plate patterned with chromium. Since the mask is in contact with the sample there is risk of contamination as the mask may contain debris from previous contact[47].

3.8 Scanning electron microscope

The Hitatchi S-5500 S(T)EM is an in lens cold field emission electron microscope that can achieve a maximum resolution of 0.4 nm. Surface profiles can be examined using the secondary electron detectors while the backscattered electron detectors can distinguish between light and heavy materials. The microscope also have bright and dark field detectors to allow for transmission measurements. For this work only the secondary electron emissions have been examined. The depth from where these electrons originate is determined by the acceleration voltage. A higher voltage will cause the electron beam to penetrate deeper into the sample and the secondary electrons will originate from the penetration depth of the beam, making structures appear smoother. For this work an acceleration voltage of 10 kV was found to provide good characterization of the sidewall roughness.

The microscope was also supplied with cross section stages with a slit measuring 7 mm wide and 3 mm deep. A sample scribed and broken accordingly can fit sideways into the slit to be fastened by screws and then inserted into the microscope, allowing the user to examine sidewall profiles as well as characterize the roughness from a different angle.

Chapter 4

Design

This chapter will describe the process of making the waveguide and racetrack resonator. First a summary of some of the results of the simulations done in the project thesis will be presented. Then the different mask designs will be shown. Lastly there will be a short review of the general fabrication process.

4.1 Racetrack resonator

As mentioned in the introduction the waveguides have dimensions 500 × 220 nm^2. The design process of the racetrack resonator is detailed in the project thesis[7], however a brief summary of some of the most important results will be given here. The simulations were performed using COMSOL Multiphysics. This program uses the finite element method which is described in the project thesis[7].

Firstly the coupling length was found on the basis of propagation constants for the odd and even modes found in table 4.1. A waveguide separation of 200 was chosen and the coupling lengths were calculated according to[20]

$$L_c = \frac{\pi}{\beta_e - \beta_o} \tag{4.1}$$

where β_e and β_o denote the propagation constant for the even and odd mode,

Table 4.1: Odd and even propagation constants for different separations found through simulations.

Separation [nm]	$\beta_o[10^6]$	$\beta_e[10^6]$
500	6.55231	6.73128
450	6.52536	6.75809
400	6.49093	6.79348
350	6.44741	6.84062
300	6.39324	6.90421
250	6.32719	6.99175
200	6.24874	7.11595

respectively. The calculation yielded a coupling length of 3.6226 μm. Simulations were run on a simple structure consisting of two waveguides of length 3.6226 μm placed 200 nm apart, and were found to be in agreement with the theoretical results as shown in figure 4.1.

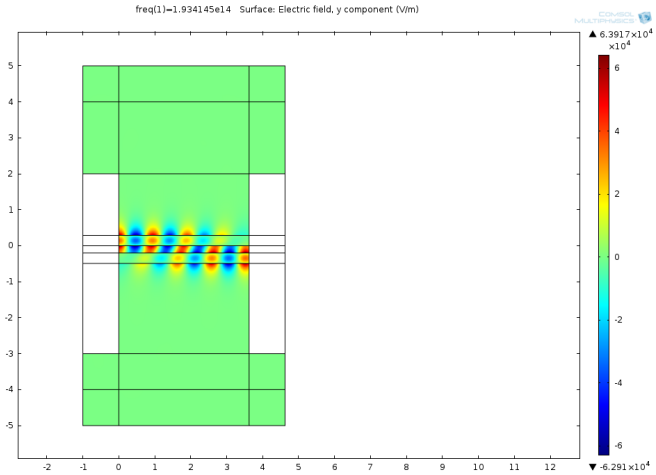

Figure 4.1: *Simulated coupling length of 3.6226 µm with a waveguide separation of 200 nm. The field shown is the y-component of the electric field.*

With the coupling length determined the bend radius of the resonator could be calculated. For a specific wavelength to experience constructive interference within the ring, the phase must be a multiple of 2π after each round trip. The

round trip length is

$$L = 2 \cdot (L_c + 2\pi r). \tag{4.2}$$

According to equation (2.37) the radius is then

$$r = \frac{\lambda_{res} m}{2\pi n_{eff}} - \frac{L_c}{\pi}. \tag{4.3}$$

With n_{eff} having been found to be 2.82 earlier in the project thesis[7] some radii were calculated using different number of wavelength oscillations, m. From the results the bend radius was chosen to be 3.2208 μm. The reason was that this radius was adequate when taking into account bend loss and die area. When simulating the whole resonator structure however, it was found that because of fringe effects from the bends before and after the coupling region, the coupling length needed to be halved to 1.8113 μm. The results are shown in figure 4.2.

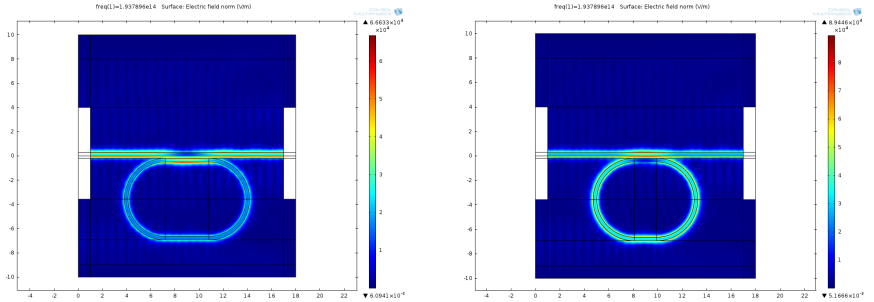

(a) (b)

Figure 4.2: *Full resonator structure with a straight coupling section of (a) 3.6226 μm and (b) 1.8113 μm. The colour bar to the right represents the normalized electric field.*

4.2 Mask

The project thesis[7] focused on the design of the racetrack resonator for specific wavelengths and a specific coupling length. However when implemented for testing purposes there are extra considerations that must be taken into account

when designing the mask layout. How will the light be coupled into the waveguide? How far away should the reference waveguide be from the test waveguide? How long exposure time will the mask need?

As this is precursory work for work with SOI and testing, light coupling to the waveguides from optical fibre had to be considered as well. Butt coupling to the waveguides using an inverse silicon waveguide taper cladded with a polymer of low refractive index is chosen in this work. The reason for this choice is that it is easier to realise an inverse tapered waveguide without adding more process steps. A coupling grate require a different etch depth than the waveguides[50], therefore another EBL and etching step would be needed to integrate gratings with the waveguides.

Firstly a mask was made to test how well the smaller dimensions would handle the suggested process. The mask is shown in figure 4.3. The leftmost part of

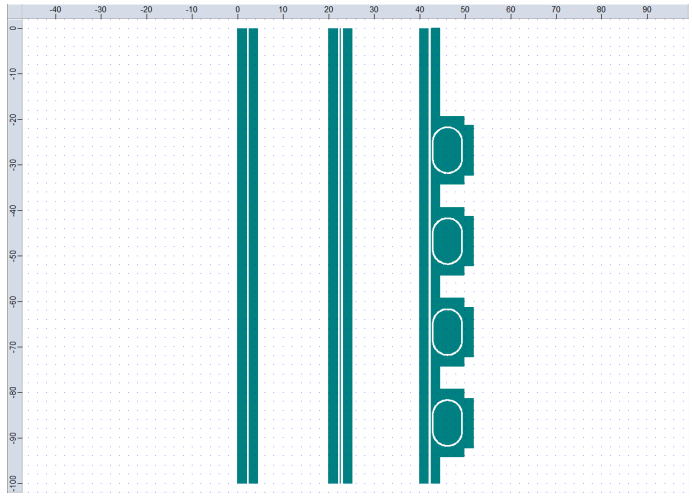

Figure 4.3: *The first mask design comparing a single waveguide to two closely spaced waveguides to the designed resonator and waveguide.*

the mask is a single waveguide by itself, the middle part are two waveguides spaced 200 nm apart, and the right part consists of a single waveguide with four racetrack resonators spaced 200 nm apart from the waveguide. There are four resonators to check for process uniformity across the mask. The resist being used is positive which means that the exposed areas are being softened and removed

during development, i.e. the green areas of the mask will be etched making the white space between them the waveguides. The distance between the waveguide sides and the remaining surface is 2 μm to ensure that very little light couples to the wafer. The resonators were made with a bend radius of 3.2208 μm and a coupling region length of 3.6226 μm. However the longer coupling region has no consequences for this work as this thesis focuses on optimizing the fabrication process.

After the exposure and etch test the etch test mask was extended to be able to reach the edges of the dies. The mask is shown in figure 4.4. The initial thought

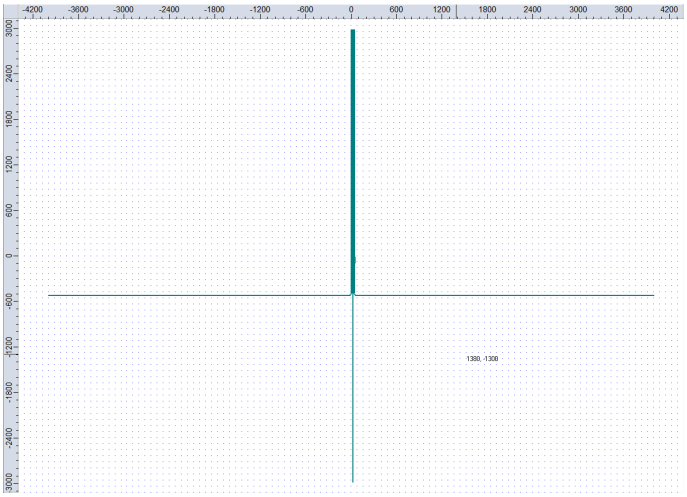

Figure 4.4: *The second mask design. A beginning solution to external coupling and designing larger masks.*

was to couple light into the different waveguides from each side to ensure that light would only couple into the intended waveguide. This led to the discovery that the Raith software handles the mask by making a square around the far edges of the mask and then divides the whole square into write fields. Because of this the mask was divided into approximately twelve million units. It was apparent from the Raith software that the length of time needed to expose the mask was excessive. Therefore this mask was not exposed.

The unreasonably long exposure time required revealed the need to review the design. The new mask in figure 4.5 shows that instead of having the inputs on

different sides of the die, they are both located at the lower end by using two 20 μm radius 90 degree bends, the middle waveguide left straight. The number of

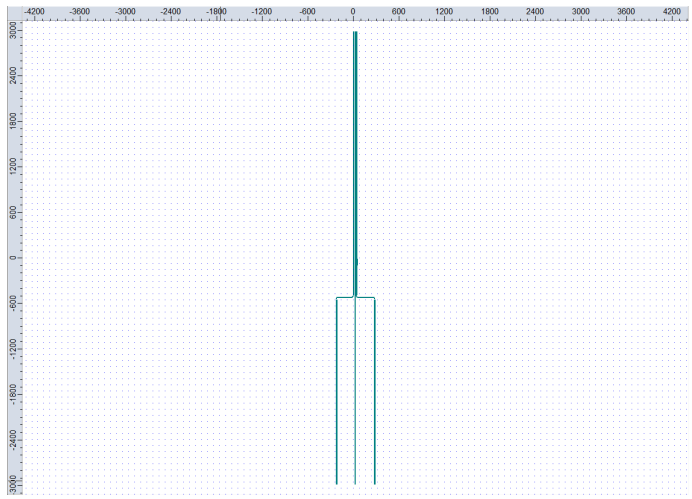

Figure 4.5: *The third mask design, making the area of the mask smaller while retaining length.*

resonators was left at four for easier cross-section inspection after scribing and breaking.

Later a new version of the mask shown in figure 4.5 was made, improving on the mask design by removing the two middle waveguides which were no longer needed, and adding inverse tapers as well as 4.5 μm of trenches to the ends of the waveguides to make room for butt coupling. The tapers are 100 μm long and taper from a width of 500 nm to 80 nm. This gives a natural mark and room for error when scribing and breaking by removing silicon from an area in front of the taper. The left most waveguide is just a plain waveguide mirroring the waveguide with the racetrack resonator. This is not removed as it is going to be used as a reference waveguide, which will have comparable roughness and therefore comparable losses to the waveguide being measured. The reasoning is that the loss from the reference waveguide can be subtracted from the loss of the waveguide with the racetrack resonator, giving reasonable certainty that any major loss contribution comes from the resonator and not the waveguide itself. The mask is shown in figures 4.6a and 4.6b. Eventually this mask would be

(a) (b)

Figure 4.6: *The fourth mask design, including inverse tapered waveguides for external coupling. Consists of one reference waveguide and a waveguide with resonators. This mask is given slight changes throughout this work.*

further improved upon by placing the tapers on a different layer, elongating the trenches in front of the tapers, and widening the tip of the tapers. The tapers were placed on a different layer so that the dose scale factor for the tapers could be set separately from the rest of the waveguides. The trenches in front of the tapers were extended from 100 μm to 123 μm because some results showed very bad write field alignment at the beginning of the mask. The edge of the write field at the beginning of the mask coincides with the edge of the first element when that element is 100 μm. This element, i.e. the trenches, was extended such that the edges of the element coinciding with the edge of a write field could either be identified as the problem or ruled out as the problem. A taper tip of 80 nm could be achieved, but with significant roughness. The tip was then widened from 80 nm to 150 nm, still tapering over 100 μm. A width of 150 nm was chosen as it was wide enough so that the major roughness problems would not arise, but still narrow enough to keep reflection loss low[51]. Along with the tapers the mask was adjusted so that no structures were overlapping.

A mask containing only a single taper was made to be able to test which exposure doses would provide good tapers for the larger mask. The mask is shown in figure 4.7. The taper is identical to the one described earlier, tapering from 500 nm to 80 nm over a length of 100 μm.

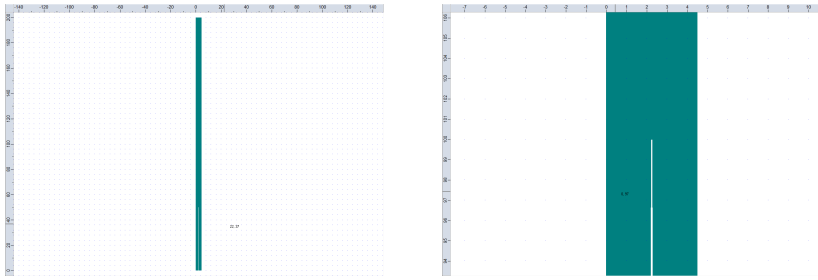

(a) (b)

Figure 4.7: *The taper mask. Contains a waveguide inverse tapered from 500 nm to 80 nm width over 100 µm, and a wide trench of 4.5 µm following the taper.*

4.3 Fabrication

The general process flow for making the waveguides and racetrack resonators is reviewed briefly in this chapter. Firstly a 250 μm thick two inch silicon wafer is scribed and broken into 16-20 10×6 mm^2 sample pieces. All the pieces are then cleaned according to the following sequence to ensure no silicon dust from the breaking process is left.

1. Acetone
2. Ethanol
3. Isopropanol
4. De-ionized water

The samples are then stored and marked with a number in 4×4 sample holders.

Samples are then later taken out and are taken through the following procedure for spin coating.

1. Clean
2. Dehydration bake
3. Spin coat
4. Anneal

Then the resist thickness is measured by a reflectometer before the sample is mounted to the EBL stage. The sample is exposed with a mask in the EBL and then developed in a mixture of nine parts isopropanol and one part de-ionized water. The developed mask is then investigated for any contaminations using an optical microscope. The etching chamber of the ICP-RIE instrument is then conditioned by performing a dummy run. A dummy run is running the etching recipe on the carrier wafer. After the dummy run the sample is placed in the ICP-RIE by putting Fomblin oil on the carrier wafer and putting the sample on the oil, making sure the oil is only present underneath the sample. After the etch the resist thickness is once again measured by a reflectometer to investigate the etch rate of the PMMA. The resist is then stripped off the sample and the sample is cleaned. The sample is then carefully scribed and broken to prepare for a cross-section inspection in the SEM. The sample is once again cleaned and then mounted to the SEM first for an overhead view to measure the roughness and then in the cross-section holder to characterize the sidewall profiles.

Chapter 5

Results

This chapter will go through the results chronologically and discuss the results, and at the end give a short summary on all the results. The samples will be discussed chronologically according to the sequence they were processed. Some samples were not fully processed and did not contribute significantly to the results, and as such have been excluded.

5.1 Exposure and etch test

The samples discussed in this section were used as initial exposure and etching tests. The purpose of these samples were to familiarize the author with the equipment and provide some initial data to proceed further.

Sample L4.16 The first few exposure and etch tests served also as lab practice to gain experience using the equipment. The samples were cleaned as per the method described in section 4.3, then resist was spun on. Sample L4.16 had resist spun on at 300 rpm for 12 seconds and then 2000 rpm for 45 seconds. The sample numbering is explained in appendix A. The thickness of the resist on L4.16 was not measured but it is estimated to lie between 550 nm and 600

Table 5.1: The first spin recipe.

Sequence	*Spin speed[RPM]*	*Time[s]*
1	300	12
2	2000	45

nm[1]. The thick nature of the mask stems from the work done by my co-student Marius Lorvik[6], which this master thesis builds upon. In [6] it is explained that because of poor selectivity during etch, a thickness of approximately 500 nm is needed. Left over resist of a blend mentioned in [6] was used. However some of the anisol, which is the solvent in this resist, had evaporated, making it thicker, which explains the extra 50-100 nm of resist thickness for sample L4.16.

After spinning on the resist sample L4.16 was given a cursory visual inspection for any defects in the mask and then scratched with a scalpel. The scratch was made using one fluid motion aiming for the middle of the sample and dragged down to the edge of the sample. This is done to get controlled defects in the sample to use for the EBLs iterative and time-consuming configuration process. The sample is then put into the EBL to start the configuration process. This process entails angle and origin correction, to make sure the mask is exposed straight relative to the sample and is exposed at the wanted location respectively. Then focusing on the sample and correcting astigmatism by aligning the three deflectors. The next step is to make contamination dots on the sample close to where the mask exposure is being placed so that the dot is made at the same height as the mask. This means to expose the smallest dot possible on the sample for a given period of time. At first this exposure may take 1-2 minutes. If no dot has appeared or if it is not perfectly round, a reiteration of focusing and stigma correction is needed. This configuration process continues until a perfectly round contamination dot appears in 5 seconds or less. The beam current is then measured by zooming in on the Faraday cup located on the stage. The measurement is done by an amperemeter that can measure picoamperes, which is connected to the EBL. The last configuration step is to align the write fields. This is done by finding a particle or dent in the sample. This alignment mark should be stationary and be easy to discern from different angles, like a pointy edge or the middle of a circle. When a manual write field alignment step

[1]The thickness not having been measured, is estimated using the data from following samples.

is initiated an area is divided into a set amount of write fields with a set step size. The settings used in this master thesis were 4 write fields with step sizes being 60 μm, 10 μm, 5 μm, and lastly 1 μm. The manual part is to align the middle of the image for all four write fields to a chosen point on the particle. This is usually done once for all the step sizes except the last and smallest one. The alignment process for the smallest step size needs to be reiterated until the log in the protocol tool shows that the misalignment, delta u and delta v, are at or below specifications for the tool. This usually takes around 10-15 reiterations of the smallest step. The whole configuration process takes an experienced user 1-2 hours, while someone new to the instrument might need up to 4 hours.

When done with the configuration the exposure is set up. This is done by putting the mask in a position list and then putting in the (u,v)-coordinates for the lower left corner of the mask in the properties menu of the step in the position list. For clarification the u- and v-coordinates are the relative x- and y-coordinates, respectively, taking angle and origin correction into account. The dose scale factor is set, the beam current is defined by the user, and then the software calculates the step size and dwell time needed with respect to the selected dose. This is done for areas, curved elements, lines and dots. For sample L4.16 mask depicted in figure 4.3 was used 4 times being 100 μm apart in u-direction, with a scale factor of 0.8, 1, 1.2, and 1.4, respectively. This is a bit misleading because of a misunderstanding with exposure doses. The misunderstanding led to the actual doses deviating slightly from the default doses. After exposure the sample was developed using 9 parts isopropanol and 1 part deionized water. The sample was submerged in the developer for exactly 30 seconds while applying slight agitation. After 30 seconds the sample is quickly lifted out of the developer and into a basin of water, again applying slight agitation. As a final step the developed mask was inspected in a microscope to look for flaws in the mask and to give hints as to what to expect after the etch.

For the etching step, first a carrier wafer for the sample is chosen and then the etching chamber in the ICP-RIE is prepared by running the recipe first on only that carrier. This is to make sure that only the materials expected are present in the chamber. For sample L4.16 a silicon carrier was chosen, the recipe used is given in table 5.2. The recipe builds on the recipe given in [6]. The only change made for this thesis is that the ICP power is halved to 600 Watts. The effect of this is that the reactive ion density is lowered, resulting in a slower etch rate. The recipe was run for 40 seconds. With data acquired from [6] and an almost linear relationship between ICP power and etch rate, the etch depth is expected to be approximately 300 nm. After etching the mask thickness was checked by a

Table 5.2: ICP-RIE etch recipe for shallow silicon etch. Modified from [6].

Parameter	*Amount*	*Unit*
SF_6 flow	7.5	sccm
CHF_3 flow	50.0	sccm
Pressure	15	mTorr
CCP power	40	W
ICP power	600	W
Temperature	20	°C
Helium backing	10	Torr

reflectometer and then removed in an acetone bath. The PMMA thickness was found to be between 320 nm to 330 nm depending on the location on the sample the thickness was measured. The etch depth was reassured with a profilometer, by running the tip over the valley left by the scalpel when making a scratch in the sample mask. The data is shown in figure 5.1. The profileometer scan shows that the silicon etch depth is approximately 336 nm, making the etch rate

$$\text{Silicon etch rate} = \frac{33\ nm}{40\ s} \cdot 60\ s = 504\ {}^{nm}/_{min}. \tag{5.1}$$

The hill that can be seen in the figure before the trench could be caused by a speck of dust, or mask residues left after being cleaned. Another possibility is in the event that the mask lost adhesion close to the trench when scratched with a scalpel some silicon might have deposited under the mask to form a hill. The latter explanation seems unlikely however because of the size of the hill. It is several micrometers wide as well as tall, which is substantially more than would have potentially deposited during an etching process according to the cleanroom engineers.

As a final step before characterization the sample is scribed and broken so that it is possible to look at the sidewall profiles of the waveguides and racetrack resonator. This is done by scribing on either side of the structures and then breaking it. This will cause a clean break across the structures. Unfortunately, because of inexperience with the scriber, the structures on sample L4.16 were ruined by the scriber. The tip was driven over the waveguides and resonators and because the scribe tip is fairly large in comparison, and due to the nature of scribing, the structures were completely destroyed.

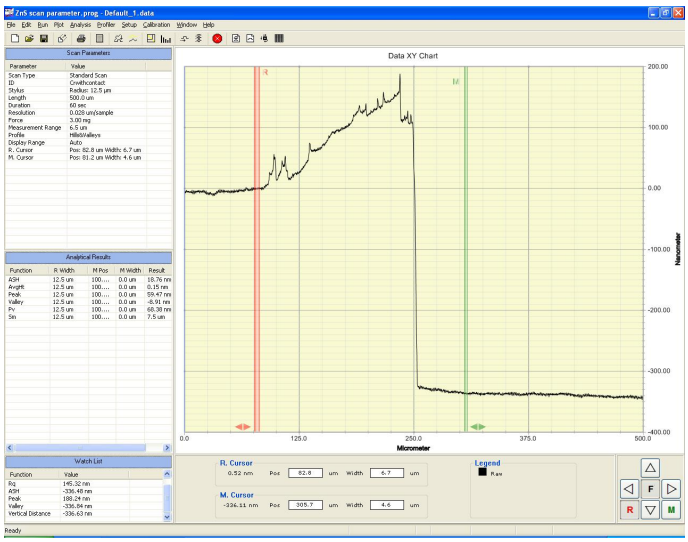

Figure 5.1: *Profilometer scan for sample L4.16. A large "hill" can be observed leading to the trench.*

Sample L4.15 Although no images of sample L4.16 were acquired, the sample was inspected in an optical microscope before the etch. This inspection suggested that a dose scale factor of 1.2 or 1.4 would provide good results. This, alongside a desire to determine a necessary write field and wish to identify issues related to write field alignment, prompted an experiment using a larger mask. The resist was spun on these samples according to the recipe in table 5.1 using the resist blend left over from Marius Lorvik's experiments. The recipe yielded a thickness of 611.1 nm with a g-factor[2] of 0.996. This sample was originally intended to be exposed using the mask in figure 4.4 with a write field of 2 μm. However the EBL instrument showed that the exposure of this mask would demand an unreasonable amount of time, therefore they served as tests of the spin recipe to check a probable thickness yield of the previous sample as well as giving experience with the EBL process. The reason for choosing such a small write field when exposing the mask for this sample was to define the minute features of

[2]The g-factor is a number given by the refractometer called goodness of fit. The closer the number is to 1, the more accurate the measurement is. A layer of poor uniformity would lower this number.

the racetrack resonator. The Raith software divided the mask into ∼12 million write fields and it was evident that even the calculation of the time the exposure would take would not finish for at least a day. This result demanded a mask covering a smaller area and a larger write field.

Sample L4.14 Resist was spun on these samples according to the recipe in table 5.1 using the deteriorated resist blend. The recipe yielded a thickness of 580.0 nm with a g-factor of 0.995. The mask depicted in figure 4.5 was calculated to take ∼48 minutes when using a write field of 100 μm, ∼68 minutes using a write field of 50 μm, and ∼113 minutes using a write field of 25 μm. A write field of 100 μm was used according to recommendations by the engineer. The dose scale factor was set to 1.4. The sample was overdeveloped by 15-30 seconds because the sample slipped from the tweezers grip. Most of the waveguides disappeared as a result as shown in figures 5.2a and 5.2b.

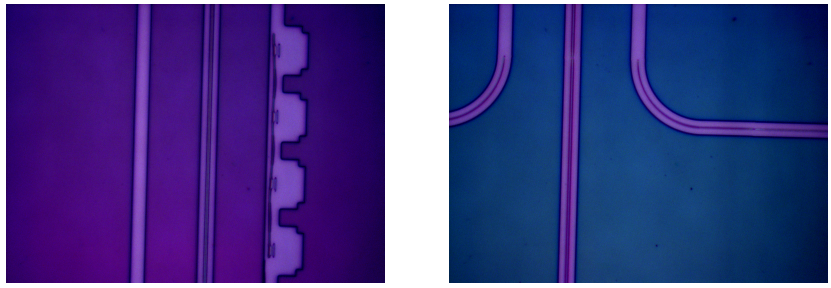

(a) (b)

Figure 5.2: *Overdevelopment of the exposed mask resulting in feature disintegration.*

The masks are made on a grid where the middle of the grid is defined as the origin. The masks were made such that the origin of the grid is in the middle of the mask. It was previously thought that the Raith software would match the origin of the mask with the coordinates set for the exposure on the stage. The image of the exposed mask in figure 5.3 shows that this is not the case. The mask has its origin close to the resonators and the stage has its origin defined to be the tip of the scratch seen to the left of the image. The mask was set to be exposed 1 mm to the right of the origin. Figure 5.3 implies that the Raith

software matches the lower left corner of the mask with the exposure coordinates.

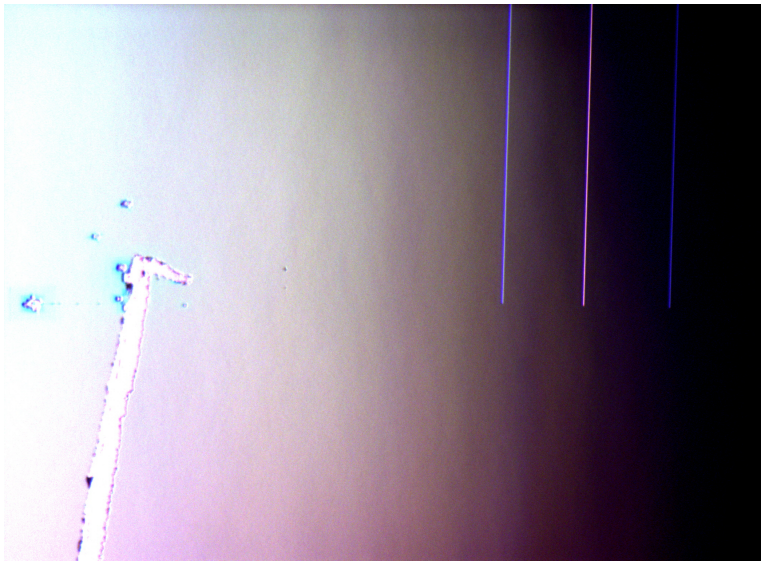

Figure 5.3: *The Raith software Elphy Plus defines the lower left portion of the mask as the beginning of the mask.*

Sample L4.13 PMMA resist was spun on according to the recipe in table 5.3 using the deteriorated resist blend. The reason for the change was because of mask thickness results from previous samples. The target thickness is ∼500 nm, however due to anisol dissipating from the solution the resist thickness was ∼80-100 nm thicker. The increased rotation velocity is an attempt to counteract the effects of the thicker resist[52]. This yielded a thickness measured to be 517.9 nm with a g-factor of 0.9968. Since a thinner resist layer was expected, another exposure test was performed. Again the mask in figure 4.3 was utilized four times, this time with dose factors 1.2, 1.4, 1.6, and 1.8, and inspected after development. Previous inspections suggested a dose scale factor of 1.4 to be promising. Therefore the range was set from 1.2 to 1.8 to observe if this would present under- or overexposure, respectively. Figures 5.4a-5.4d present the results as inspected by an optical microscope at 100 times magnification,

Table 5.3: The second spin recipe.

Sequence	*Spin speed[RPM]*	*Time[s]*
1	500	12
2	2500	45

ranging from dose scale factors 1.2-1.8, respectively. As can be seen from the figures, figure 5.4d looks to be the best developed, indicating that a dose scale factor of at least 1.8 is needed.

After inspection etching was done with the recipe in table 5.2. Except for the etching time the recipe was not changed during the lab work for this thesis. The reason for keeping the recipe constant was that it was postulated that the significant sidewall roughness was attributed mostly to overexposure of the resist layer during electron beam lithography. This time the etching step was set to 30 seconds. The plasma stabilized after approximately 2 seconds. The plasma stabilization time is important because as explained in section 3.4 plasma is needed to supply reactive ions. Consequently when no plasma is present the gases will not be decomposed into reactive ions and no significant etching will be accomplished. This gives a certain margin of error when calculating the etch rate since two seconds of unstable plasma does not necessarily imply two seconds without plasma. By increasing the etch time the margin of error in the etch rate can be reduced. The recipe is designed for use with SOI wafers, therefore the etch depth is trivial provided that it is more than 220 nm. This etch does not have great selectivity between silicon and silicon dioxide[45]. However, the consequence of etching into the oxide layer is a lower effective refractive index for the cladding providing greater confinement. Greater confinement is generally better for a waveguide, but might cause issues in coupling regions, requiring the regions to be longer. Another consideration is that a lower cladding index might cause more interference effects in areas with roughness issues[53].

After the etch, the resist thickness was measured by the refractometer to be 339.3 nm, with a g-factor of 0.9949. This makes the PMMA etch rate

$$\text{PMMA Etch rate} = \frac{517.9\ nm - 339.3\ nm}{30\ s} \cdot 60\ s = 357.2\ {}^{nm}/_{min} \tag{5.2}$$

The two seconds used to stabilize the plasma has been included as it is believed that plasma was present for a greater amount of time than not during the

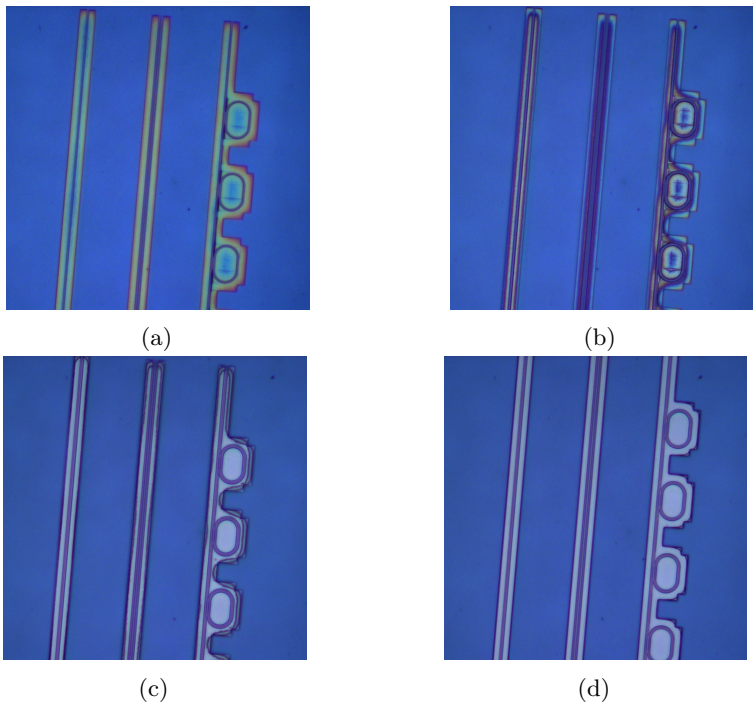

(a) (b)

(c) (d)

Figure 5.4: *517.9 nm thick PMMA resist developed after being exposed with a dose scale factor of (a) 1.2, (b) 1.4, (c) 1.6, and (d) 1.8.*

stabilization period. This gives a margin of error such that the PMMA etch rate might be slightly higher than calculated.

The results of the processing is shown in figures 5.5a and 5.5b. From the walls in figures 5.5a and 5.5b underexposure can be observed. However, only slightly for a dose scale factor of 1.8 as shown in figure 5.5b, which can be observed in the unfocused background behind the resonator. This indicates that a dose increase is necessary.

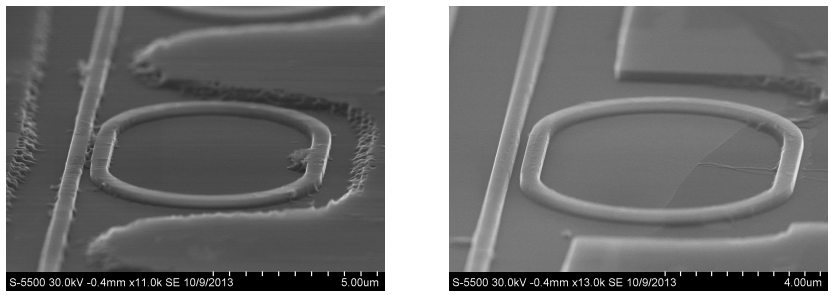

(a) (b)

Figure 5.5: *The etching results of exposures at dose scale factors of (a) 1.6, and (b) 1.8.*

Sample L4.11 The resist was spun on according to the recipe in table 5.4 using the deteriorated resist. The reason for changing the spin time from 45

Table 5.4: The third spin recipe.

Sequence	*Spin speed[RPM]*	*Time[s]*
1	500	12
2	2500	60

seconds to 60 seconds was to improve uniformity though it is unclear if the change had any significant impact. The yield for this spin recipe using this resist was measured to be 559.9 nm with a g-factor of 0.9984. This sample had its resist layer spun on a few weeks later. Since there was very little resist left in the bottle, the anisol in the solution will continue to dissipate until the bottle is filled with the dissipation gases. When the bottle is then opened the gases are released giving space for the anisol to continue to dissipate. Therefore the solution effectively deteriorates further every time the bottle is opened, making it thicker, which can explain the result of a thicker mask. The mask used by the Raith software was the one depicted in figure 4.6, exposed at a dose scale factor of 2.0. The increase is due to the previous results showing signs of underexposure. Figure 5.6 shows upper tapers in the mask after exposure and development. The tips look to have been lifted up from the substrate and curled in the developer. The reason for this behaviour could be; the dose is too high, the write field of 100

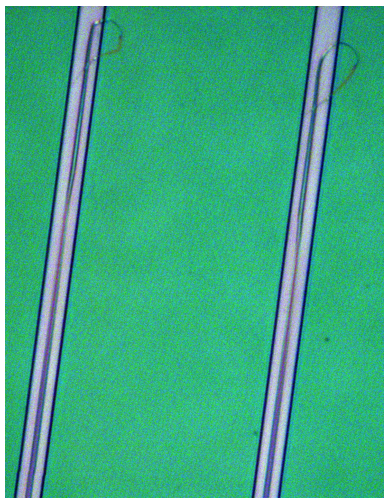

Figure 5.6: *The resulting tapers using a 559.9 nm thick PMMA layer and a dose scale factor of 2.0. Note the taper tips loosing adhesion and curling.*

μm cannot handle the smaller feature, the mask is too thick, or a combination of the three. One of the lower tapers was better defined than the rest, shown in figure 5.7.

The sample was etched for 30 seconds using the recipe in table 5.2 with a silicon carrier. After the etch the PMMA was measured to have a thickness of 379.6 nm, with a g-factor of 0.9995. The calculated etch rate is then

$$\text{PMMA Etch rate} = \frac{559.9\ nm - 379.6\ nm}{30\ s} \cdot 60\ s = 360.6\ {}^{nm}/_{min} \tag{5.3}$$

The silicon etch depth was measured to be ∼305 nm, giving an etch rate of

$$\text{Silicon Etch rate} = \frac{305\ nm}{30\ s} \cdot 60\ s = 610\ {}^{nm}/_{min} \tag{5.4}$$

This in turn presents a selectivity of

$$\text{Selectivity} = \frac{610\ nm}{360.6\ nm} = 1.692 \approx 1.7 \tag{5.5}$$

The etch recipe in table 5.2 retains a selectivity of 1.7:1 for silicon:PMMA when using a silicon carrier.

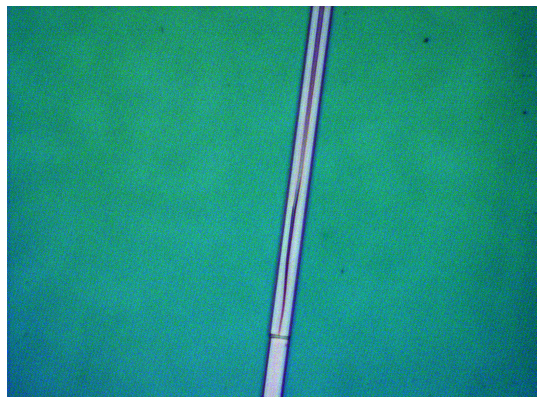

Figure 5.7: *A better defined taper for sample L4.11. Note that some deformation is still present.*

The SEM images in Figures 5.8a to 5.8d show significant variation in write field alignments. The EBL instrument being used have a write field accuracy of 40 nm according to the engineer responsible for the instrument. The large variation of write field alignments could be caused by the sample being slanted[54]. This implies that the problem either resides with the stage configuration or with the sample. The most likely issue is that there is a bit of resist left on the back side of the wafer, or that there is some dust on the stage beneath the sample. The stage itself could be at a slight angle as it is configured once at the beginning of the year and it is not unreasonable to assume that over the course of a year the stage could have become slightly slanted. The exposures were done close to the end of the year. Figure 5.8a shows almost perfect vertical alignment, however further along the waveguide figure 5.8b shows a vertical misalignment of ∼90 nm. Figure 5.8c shows severe misalignment in both vertical and horizontal directions, however further along the waveguide in the same direction figure 5.8d shows nearly perfect alignment in the vertical and horizontal directions. All the images show a fairly low amount of shrinking, the waveguides are ∼10-20 nm below the intended width of 500 nm. This indicates that the exposure dose is close to optimal for these features, slightly overexposing. Figure 5.9 shows that the coupling region on the racetrack resonator is ∼30-35 nm wider than the rest of the waveguides. This could be due to some difference in the mask design or a measuring error. The two waveguides are separated by 200 nm as mentioned in section 4.1. Since this is a positive resist the area between the waveguides

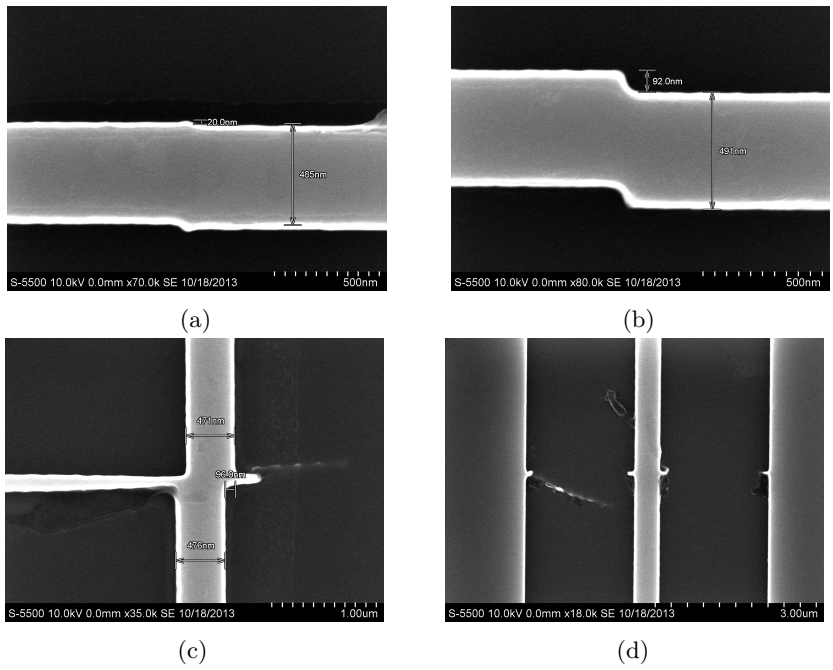

(a) (b)

(c) (d)

Figure 5.8: *Comparison images of large variations in write field alignment in both u- and v-directions. The variations can be caused by sample tilt.*

is exposed as well as the areas to the side of the waveguides. Because of the small area between the waveguides the width of the waveguides might increase because of a reduction in proximity effects[42][55]. Figure 5.10 shows the taper from the image of the mask in figure 5.7. Significant roughness can be observed as well as the deformation noted from figure 5.7. Unfortunately no cross-section images are available since a tightly fastened screw broke the sample.

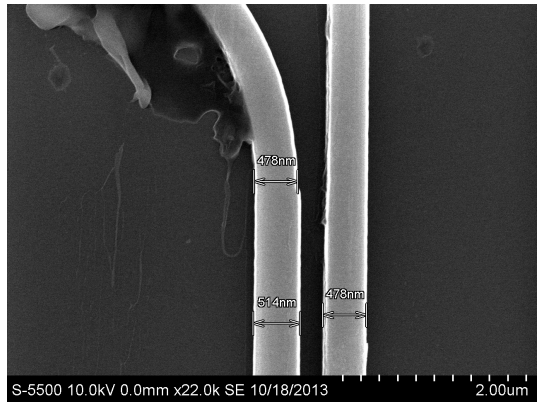

Figure 5.9: *The coupling region of a racetrack resonator with a difference in waveguide width for the resonator and coupling waveguide.*

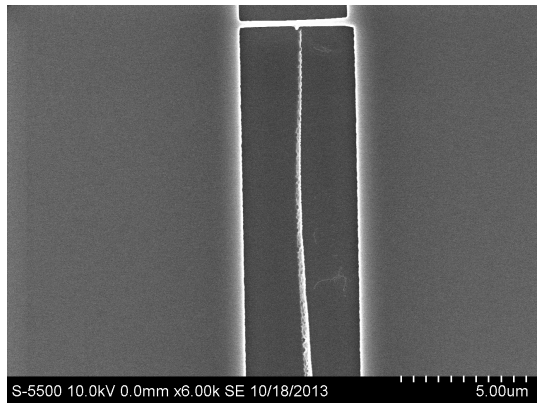

Figure 5.10: *SEM image of one of the tapers after the etching. Significant roughness and deformation is observed.*

5.2 Spin tests and taper exposure tests

The thickness of the PMMA resist layer on previous samples after etching indicates that the resist layer thickness can safely be reduced. A reduced resist layer thickness is desired as the thick resist is suspected of causing the small features of the tapers to loose adhesion and deform during development. This section contains resist mixture and spin tests to find a suitable resist blend and a lower PMMA layer thickness. After the spin tests some exposure tests with lower resist thickness are performed and discussed.

Sample L4.09 The purpose of this sample was to serve as a reference to exposures done on samples with thinner resist layers. The mask was spun on according to the recipe in table 5.5 using the deteriorated resist blend. With the

Table 5.5: The fourth spin recipe.

Sequence	*Spin speed[RPM]*	*Time[s]*
1	500	12
2	3000	60

thickening resist it was necessary to change the recipe again and increase the spin velocity. The resulting PMMA layer was measured to be 471.2 nm with a g-factor of 0.955. The reduced goodness of fit could imply greater surface roughness. The mask depicted in figure 4.7 was exposed at dose scale factors of 1.4-2.8 with a step of 0.2. A selection of the results from the exposure as inspected by an optical microscope is shown in figures 5.11a to 5.11d. Figures 5.11a to 5.11d show the taper exposed with an exposure dose scaling factor of 1.4, 1.6, 1.8, and 2.0, respectively. As can be seen from figure 5.11a even though the taper is whole, it looks to be too thick at the tip, suggesting underexposure, yet the taper still becomes malformed. This could indicate the exposure dose is not the issue.

Samples L4.08, L4.07, and L4.06 If the exposure dose is not the cause of the problem with taper deformation the mask thickness seems more likely to be causing the issue. New resist blends were made and spun on samples L4.08-L4.06. Samples L4.08, L4.07, and L4.06 were all spun on with the same recipe shown

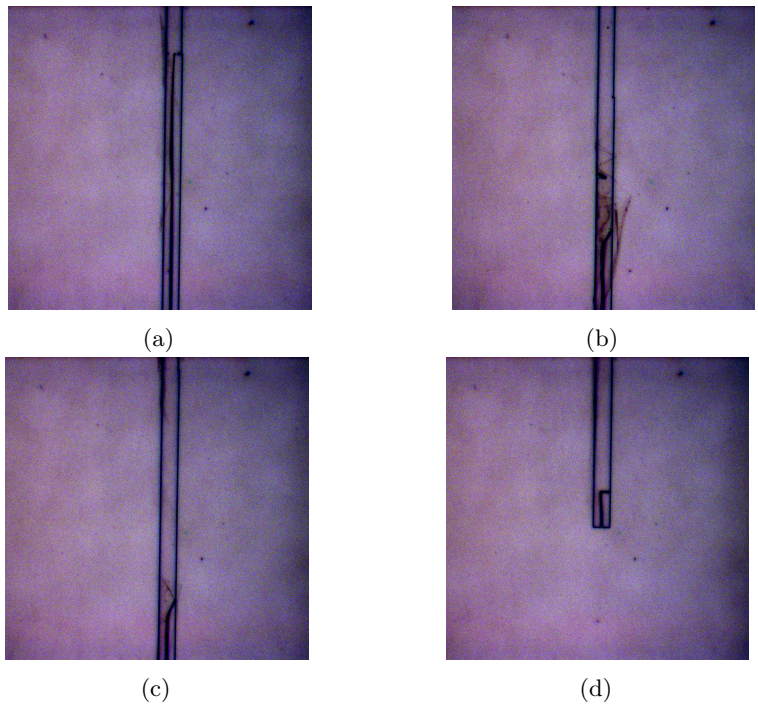

(a) (b)

(c) (d)

Figure 5.11: *Optical inspection of developed tapers with dose scale factor of (a) 1.4, (b) 1.6, (c) 1.8, and (d) 2.0*

in table 5.6. The samples are coated with different resist blends in an attempt to find an appropriate resist thickness, and see the effect of different ratios of anisol and A9 PMMA. The A9 means that the resist contains 9% solids. For sample L4.08 the blend is 25% A9 PMMA and 75% anisol. For sample L4.07 the blend is 33% A9 PMMA and 66% anisol. For sample L4.06 the blend is 50% A9 PMMA and 50% anisol. These were used as spin tests targeting a resist thickness between 250 nm and 300 nm. The results of the experiment is listed in table 5.7. From these results it is apparent that sample L4.06 with the blend of 50% A9 PMMA and 50% anisol is closest to the target thickness. By increasing the rotation speed the thickness of the resist layer will decrease further.

Table 5.6: The fifth spin recipe.

Sequence	*Spin speed[RPM]*	*Time[s]*
1	500	12
2	2000	60

Table 5.7: The results of spinning different resist blends using the same recipe.

Sample	*Resist blend PMMA A9[%]/Anisol[%]*	*Thickness[nm]*	*g*-factor[1]
L4.08	25/75	95.86	0.9992
L4.07	33/66	169.0	0.9706
L4.06	50/50	319.1	0.9985

Sample L4.05 The purpose for sample L4.05 was to investigate the effects of a thinner resist layer when exposing tapers at different doses. The 50/50 resist was spun on according to the recipe in table 5.4 which yielded a thickness of 295.6 nm with a *g*-factor of 0.9979. The mask depicted in figure 4.7 was exposed using dose scale factors of 1.4-2.6 with a step of 0.2. Figures 5.12a to 5.12d are the first four exposures at dose scale factors of 1.4, 1.6, 1.8, and 2.0 for figure 5.12a, 5.12b, 5.12c, and 5.12d, respectively. From figure 5.12a some underexposure can be seen at the outer edges as well as from the thickness of the tip of the taper. The taper in figure 5.12b seems very promising, however the tip might still be too thick. Figure 5.12c reveals some overexposure as the taper seems to disappear just before reaching the appropriate length. At a dose scale factor of 2.0 figure 5.12d indicates a problem with the taper deforming. When comparing these results with the results from sample L4.09, it is suggested that the deformed tapers are an issue with both the mask thickness as well as with overexposure.

The sample was etched for 27 seconds using the recipe in table 5.2 with a silicon carrier. The PMMA thickness was measured to be 130.4 nm with a *g*-factor of 0.9995 after the etch. This gives a PMMA etch rate of

$$\text{PMMA Etch rate} = \frac{295.6\ nm - 130.4\ nm}{27\ s} \cdot 60\ s = 367.1\ {}^{nm}/_{min}. \tag{5.6}$$

Figure 5.13 shows the first taper, exposed at a dose scale factor of 1.4, and reveals

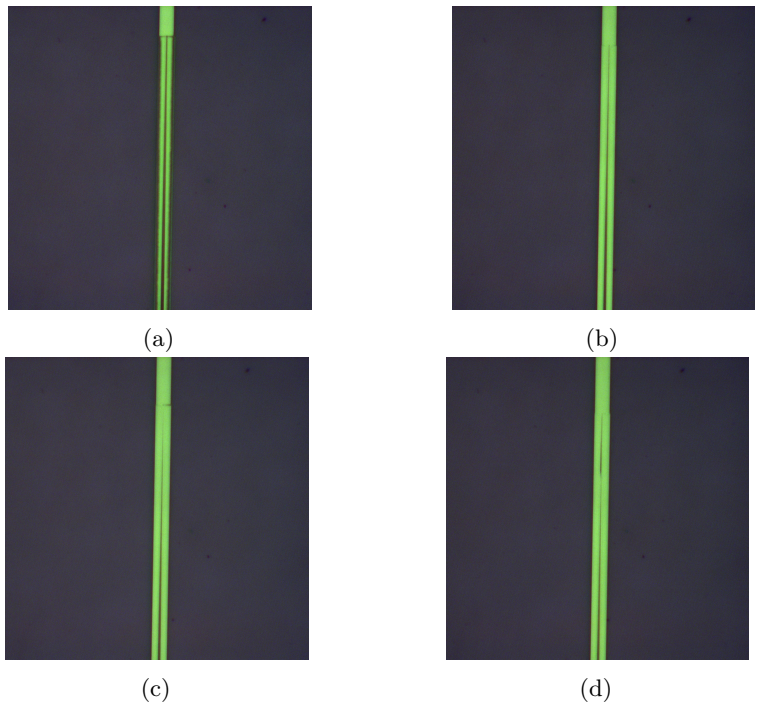

Figure 5.12: *Optical inspection of the developed tapers at dose scale factors of (a) 1.4, (b) 1.6, (c) 1.8, and (d) 2.0*

jagged edges along the entire taper. Further the general size of the roughness can be observed from figure 5.14a to be ∼15-35 nm, which would produce extreme losses. Figure 5.14b shows the tip of the taper to be ∼210 nm wide, 130 nm wider than intended, confirming underexposure. Figure 5.15a shows that even at a dose scale factor of 1.6 the edges are fairly jagged, with the size of the roughness being ∼20 nm. Figure 5.15b displays that the width of the tip of the taper is ∼113-115 nm, still indicating some underexposure. Figure 5.16a shows the roughness to be ∼10-15 nm at a dose scale factor of 1.8, exhibiting improvement. The tip in figure 5.16b is shown to be between 90-100 nm wide, very close to the desired 80 nm.

At a dose scale factor of 2.0 the taper, as depicted in figure 5.17a, exhibits a roughness of less than 10 nm. The white part at the edge of the tapered

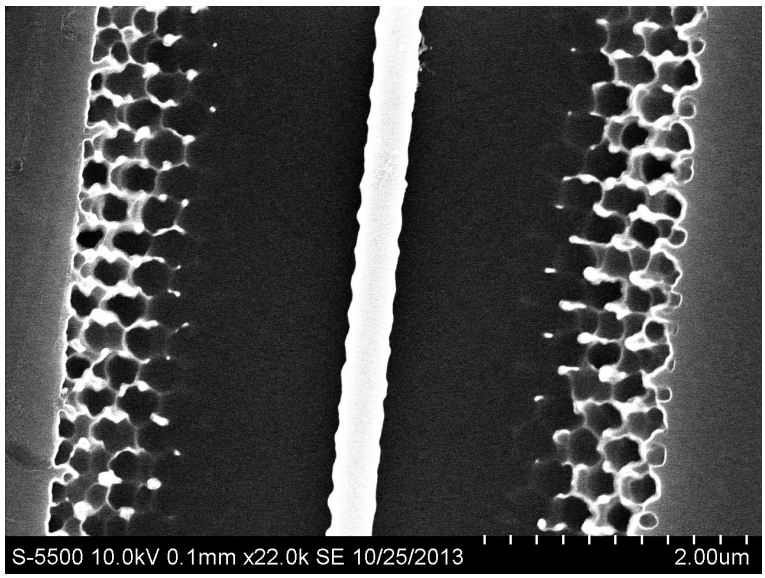

Figure 5.13: *Taper exposed at a dose scale factor of 1.4*

waveguide is perhaps a ledge or rounding of the edge. Figure 5.17b shows the taper tip to be overexposed, exhibiting severe roughness creating gaps in the waveguide and eventually disappearing entirely before the intended end.

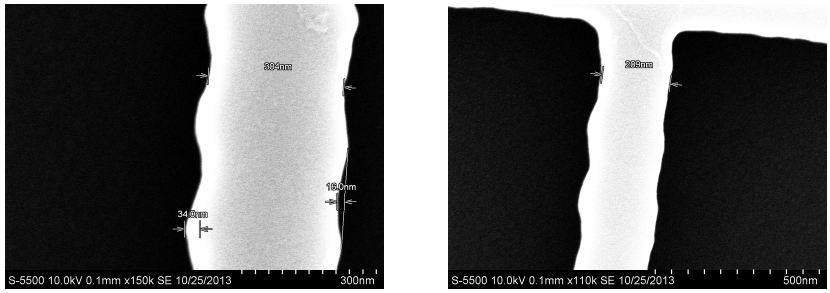

(a) (b)

Figure 5.14: *Taper exposed at a dose scale factor of 1.4. (a) The measured roughness is ∼15-35 nm. (b) The tip of the taper measured to be ∼210 nm wide.*

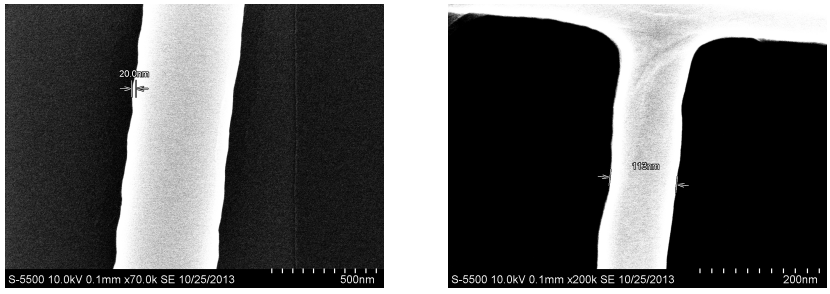

(a) (b)

Figure 5.15: *Taper exposed at a dose scale factor of 1.6. (a) The measured roughness is ∼20 nm. (b) The tip of the taper measured to be ∼113-115 nm wide.*

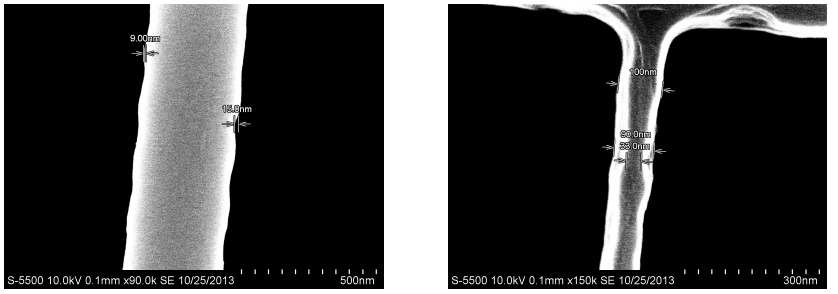

(a) (b)

Figure 5.16: *Taper exposed at a dose scale factor of 1.8. (a) The measured roughness is ∼10-15 nm. (b) The tip of the taper measured to be ∼90-100 nm wide.*

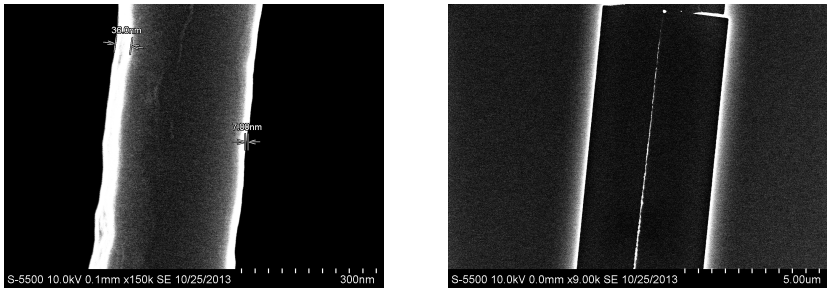

(a) (b)

Figure 5.17: *Taper exposed at a dose scale factor of 2.0. (a) The measured roughness is ∼10 nm. (b) Tip of the taper disintegrated by roughness induced by overexposure.*

Sample L4.04 The purpose of this sample was to expose the mask in figure 4.6 having the tapers tied to another layer as shown in figure 4.6b. This is done to investigate the need for different exposure doses for the tapered waveguides and the normal waveguides. The resist was spun on according to the recipe in table 5.8 with the 50/50 resist blend. Since the resist layer thickness versus

Table 5.8: The sixth spin recipe.

Sequence	*Spin speed[RPM]*	*Time[s]*
1	500	12
2	3500	60

spin speed relation is not linear but closer to an exponential decrease[52], it was expected that an increase of spin speed to 3500 rpm would yield a thickness close to 250 nm. The PMMA thickness was measured to be 259.9 nm, with a *g*-factor of 0.9981. The two layers of the mask depicted in figure 4.6 were exposed separately. Layer 0, contains the main elements of the mask, and has a dose scale factor of 2.0. Layer 1, contains the tapered waveguides, and has a dose scale factor of 1.6.

The sample was etched according to the recipe in table 5.2 for 27 seconds using a silicon carrier. The thickness of the PMMA layer was measured to be 90.16 nm, with a *g*-factor of 0.9993. The silicon etch depth was measured to be 300.11 nm. This gives a PMMA etch rate of

$$\text{PMMA Etch rate} = \frac{259.9\ nm - 90.16\ nm}{27\ s} \cdot 60\ s = 377.2\ {}^{nm}/_{min}, \tag{5.7}$$

a silicon etch rate of

$$\text{Silicon Etch rate} = \frac{300.11\ nm}{27\ s} \cdot 60\ s = 666.91\ {}^{nm}/_{min}, \tag{5.8}$$

and a selectivity of

$$\text{Selectivity} = \frac{666.91\ nm}{377.2\ nm} = 1.768 \approx 1.75. \tag{5.9}$$

A silicon:PMMA selectivity of 1.75:1 is comparable to the results from sample L4.11, with some margin of error in measurements as well as in the etch chamber atmosphere.

Because of compounded stitching errors the tapered waveguides were placed on top of the already exposed areas. This means that in addition to the aforementioned write field misalignments, there are issues when aligning a new item with an old item in the position list in the Raith software. With no options available to minimize the issue, another approach was used. By defining the exposure dose factors for the elements on each layer in the gds-editor, it was assumed that the issue was avoided since both layers were exposed in the same write field.

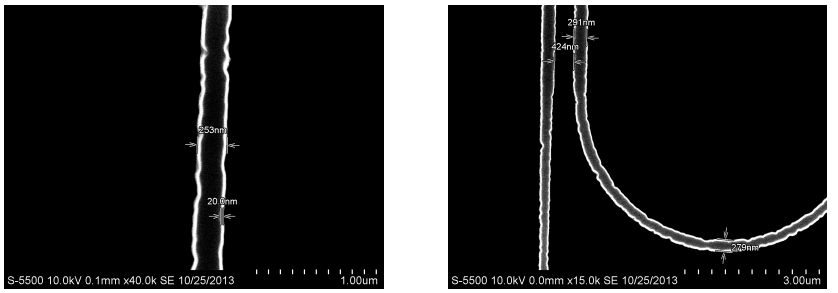

(a) (b)

Figure 5.18: *Using a dose scale factor of 2.0 on a resist layer of 259.9 nm. Gross overexposure have reduced the waveguides to half the intended size*

Figures 5.18a and 5.18a show the problem of not taking the thickness of the resist layer into account. A dose scale factor of 2.0 was meant to be used with a thickness of ∼470 nm, and a factor 1.6 was meant to be used with a thickness of ∼300 nm. However the sample provided valuable insights that can be compared to previous results. It can be seen from the figures that such overexposure have decreased the width of the waveguides to approximately half the intended size.

Sample L4.03 The purpose of this sample was to carry out the proposed solution of defining the exposure doses for the layers in the gds-editor discussed in the results of the previous sample. Resist was spun on according to the recipe in table 5.8 with the 50/50 resist blend. The PMMA layer was measured to be 273.1 nm with a g-factor of 0.9992. The second layer in the previous sample was severely misaligned with the first layer due to the use of two items in the

position list in the software. For this sample the mask depicted in figure 4.6 was still used, however the dose factors were set in gds-file as 1.8 for the main layer and 1.6 for the taper layer. In this way exposure of both the layers could be done as one item in the position list. Due to a misunderstanding of the software the dose scale factors were not saved to the elements, having them both exposed at a dose scale factor of 1.0.

The sample was etched according to the recipe provided in table 5.2 for 27 seconds using a silicon carrier wafer. The PMMA thickness was measured to be 112.3 nm, with a g-factor of 0.9995, after the etch. This yields a PMMA etch rate of

$$\text{PMMA Etch rate} = \frac{273.1\ nm - 112.3\ nm}{27\ s} \cdot 60\ s = 357.33\ {}^{nm}/_{min}. \quad (5.10)$$

The results of the etch are shown in figure 5.19. From figure 5.19 underexposure

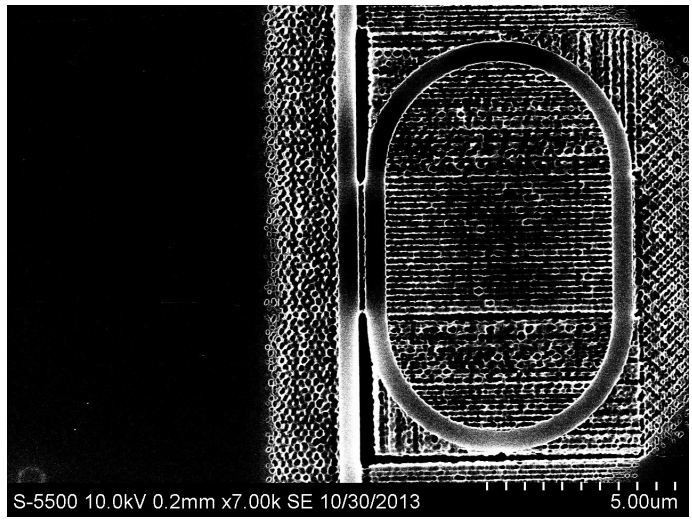

Figure 5.19: *Waveguide and resonator exposed using a dose scale factor of 1.0. Severe underexposure is evident.*

is evident. However an experiment always provides some information. The pattern that emerges from this underexposure invites some discussion on how the EBL exposes the mask. A difference in exposure patterns can be seen around the

bends of the resonator compared to the trenches on the sides of the waveguides. According to the software manual[56] the Elphy plus software handles bends by dividing them into trapezoids, which can be observed in the figure. The underexposure also makes a flaw in the mask even more prominent. Directly before and after the coupling region the area between the waveguide and the half circles have received a higher exposure dose. This is believed to be caused by overlapping elements, the width of the overlapping area being 200 nm. The overlapping area is then exposed twice at the same dose.

Sample L4.02 The purpose of this sample was to redo the experiment done for the previous sample as well as investigate the effects of using a sapphire carrier during the etching process. The resist was spun on according to the recipe in table 5.8 using the 50/50 resist blend. This yielded a PMMA layer thickness of 252.4 nm with a g-factor of 0.999. The sample was exposed using the mask depicted in figure 4.6, dose factors were set to 1.8 for the main layer and 1.6 for the taper layer in the gds-editor.

The sample was etched utilizing the recipe in table 5.2 for 27 seconds using a sapphire carrier. The carrier was switched from silicon to sapphire to minimize the amount of silicon atoms in the etching chamber. The small agglomerations seen in figures 5.21a and 5.21d were thought to be deposited silicon during the etching process. Silicon deposited on or around would cause major problems. If the silicon is deposited on the waveguide the result is very large roughness. If it is deposited near the waveguide the incoming guided wave can couple to the deposited silicon 2.2 causing loss of intensity, and possibly interference[53]. In retrospect however this is more likely residual PMMA. After the etch the PMMA thickness was measured to be 76.75 nm with a g-factor of 0.999. The silicon etch depth was measured to be ∼370 nm. This gives a PMMA etch rate of

$$\text{PMMA Etch rate} = \frac{252.4\ nm - 76.75\ nm}{27\ s} \cdot 60\ s = 390.33\ {}^{nm}/_{min}, \quad (5.11)$$

a silicon etch rate of

$$\text{Silicon Etch rate} = \frac{370\ nm}{27\ s} \cdot 60\ s = 822.22\ {}^{nm}/_{min}, \quad (5.12)$$

and a selectivity of

$$\text{Selectivity} = \frac{822.22\ nm}{390.33\ nm} = 2.106 \approx 2.1. \tag{5.13}$$

The higher etch rates when using a sapphire carrier as opposed to a silicon carrier can be explained by an increased amount of available reactive ions. As mentioned earlier the ICP power determines the ion density in the gas which reacts with the silicon in the chamber. However with much less silicon in the etching chamber the availability of reactive ions become greater, providing a faster etch[43]. The increased selectivity of 2:1 silicon vs PMMA can be explained by the fact that even though more reactive ions does increase the PMMA etch rate, the resist is etched mainly by the physical etch component[43] which does not increase with increased reactive ion availability. Therefore the silicon etch rate increased to a greater extent than the PMMA etch rate, resulting in increased selectivity.

Figure 5.20a shows a top down view of the resulting waveguide. With a width of ∼360 nm the pattern has clearly been overexposed. The roughness that resembles ledges on the side of the waveguide are potentially almost as deep as the trenches surrounding the waveguide. However it is impossible to discern from this angle. As can be seen from the figure they are ∼25-40 nm in size, representing significant roughness. Figure 5.20b shows the taper starting to deform after ∼50 μm from the overexposure. Figure 5.20c shows the measured width of the upper and lower parts of the waveguide, as well as the etch depth. Figure 5.20d shows positive sidewall profile, inclining ∼30 nm from the bottom to the top. The hypothesis is that the incline is not caused by the etching process, but stems from overexposure during EBL. Figure 5.21a shows the entire racetrack resonator and is included as a reference point for figures 5.21b to 5.21d. Figures 5.21b and 5.21c attest to the point made earlier that the roughness which appears to be shallow ledges may extend down the majority of the height. Figure 5.21d shows a close-up of the residue deposited on the coupling region of the resonator. The appearance of the residue, in contrast to the crystalline structure of the silicon, seems soft and malleable. Since no other materials have been deposited on the wafer and it does not appear to be dust, it is safe to assume that this is residual PMMA. Figure 5.22 shows a very good example of how much dust can be attracted to the waveguides during a scribe and break process.

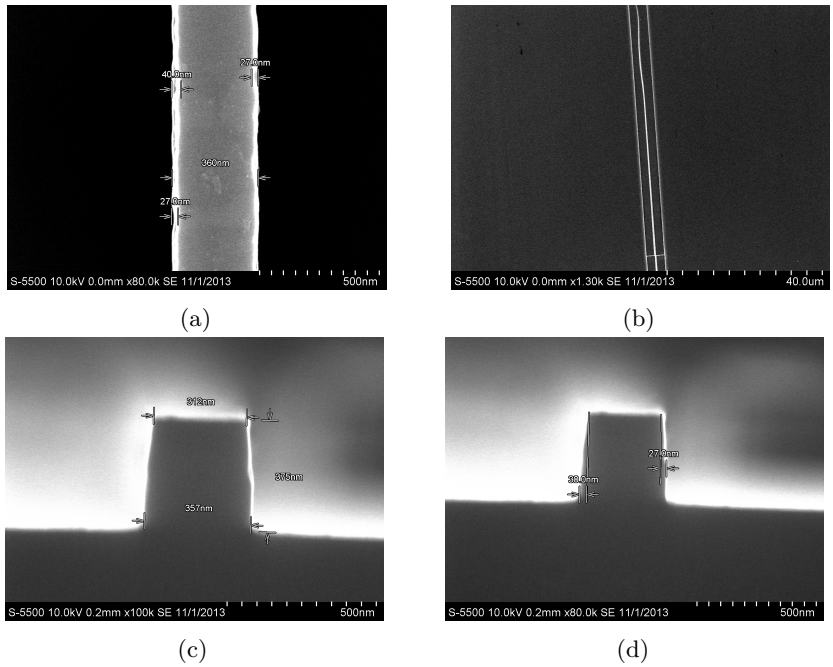

(a) (b)

(c) (d)

Figure 5.20: *(a) Top down view of a waveguide with a width of 360 nm showing roughness of 27-40 nm. (b) Top down view of a tapered waveguide. Some deformation is observed. (c) Waveguide sidewall profile showing the differences in width from top to bottom. (d) Positive sidewall profile measured at 30 nm difference top to bottom.*

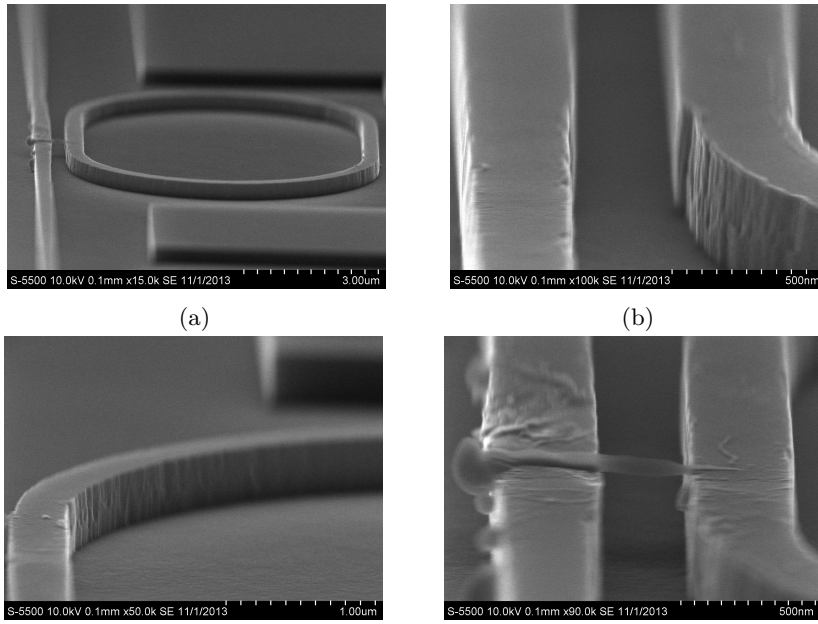

Figure 5.21: *(a) Resulting ring resonator with PMMA residues observed in the coupling area. (b) Sidewall roughness of the resonator. a shrinking of the waveguide can be observed. (c) Sidewall roughness on the inside of the resonator. (d) The residual resist deposited in the coupling area.*

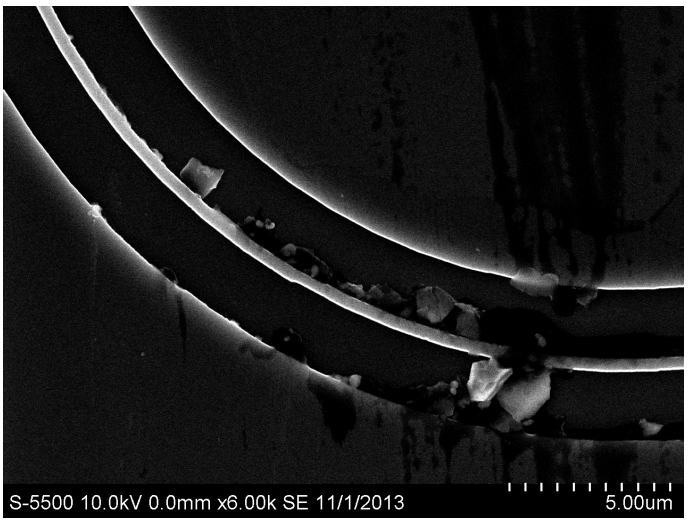

Figure 5.22: *Silicon dust from the scribing and breaking process. The black substance observed is likely residual resist.*

Sample L4.01 The purpose of this sample was to investigate if an exposure dose scale factor of 1.6, with 1.5 set for the tapered waveguides would still overexpose. The resist layer was spun on according to the recipe in table 5.8 using the 50/50 resist mixture. The resulting PMMA layer thickness was measured to be 251.7 nm with a g-factor of 0.9912. The sample was exposed using the mask depicted in figure 4.6, with dose scale factors set to 1.6 for the main layer and 1.5 for the taper layer.

The sample was etched according to the recipe in table 5.2 for 23 seconds using a sapphire carrier. The etch time was lowered as a consequence of the results from the last sample showing that the etch recipe is faster when using a sapphire carrier. After the etch the PMMA layer thickness was measured to be between 115.0-110.6 nm with a g-factor of 0.9996. Using the average which is 112.8 nm the calculated PMMA etch rate is

$$\text{PMMA Etch rate} = \frac{251.7\ nm - 112.8\ nm}{23\ s} \cdot 60\ s = 362.35\ {}^{nm}/_{min}. \quad (5.14)$$

As can be seen from the measurement results in figure 5.23 the etch depth was

measured to be ∼300 nm. The different etch depths seen in the figure originates

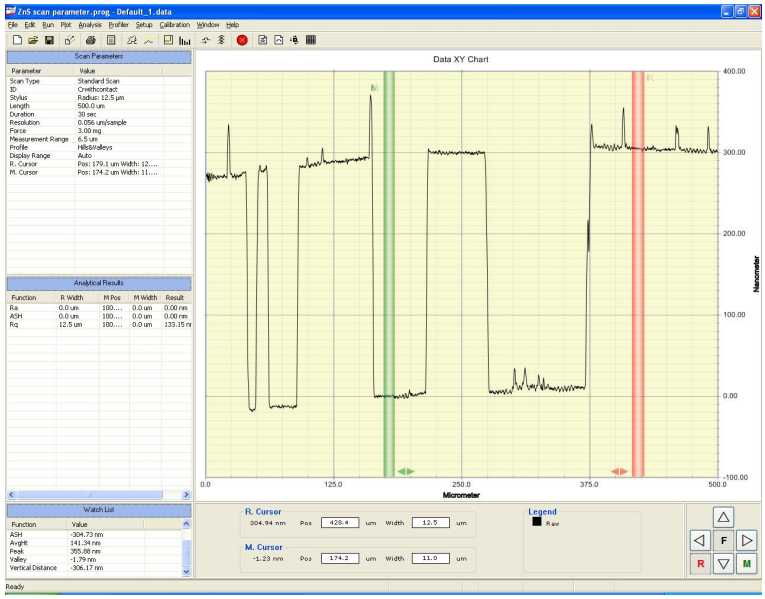

Figure 5.23: *Profilometer scan of sample L4.01.*

from varying degrees of macro-loading, which is explained in section 3.4.2. The silicon etch rate is calculated to be

$$\text{Silicon Etch rate} = \frac{306.17\ nm}{23\ s} \cdot 60\ s = 798.7\ {}^{nm}/_{min}, \tag{5.15}$$

and the selectivity then becomes

$$\text{Selectivity} = \frac{798.7\ nm}{362.35\ nm} = 2.204 \approx 2.2. \tag{5.16}$$

What can also be observed in figure 5.23 is the absence of hills before the trenches. This increases the probability that the hill observed in figure 5.1 corresponds to masking layer residue or specks of dust.

Figure 5.24a shows that the tapers are still greatly overexposed and also that deformation begins when the width of the tapered waveguide decreases past a certain point. Figure 5.24b shows that this point is at a width of ∼140 nm.

Figure 5.24c shows that the width has increased to ∼400 nm, however the roughness is still around 20-30 nm in size. Figure 5.24d shows the write field alignment to be $\lesssim$40 nm and the width of the waveguide to be ∼385 nm. When exposing this sample using the EBL the beam current was unstable, fluctuating between 38.8 pA and 40.5 pA. This could cause the variations in the waveguide width. Another possible cause is varying resist thickness as an area with a thinner resist layer would require less exposure.

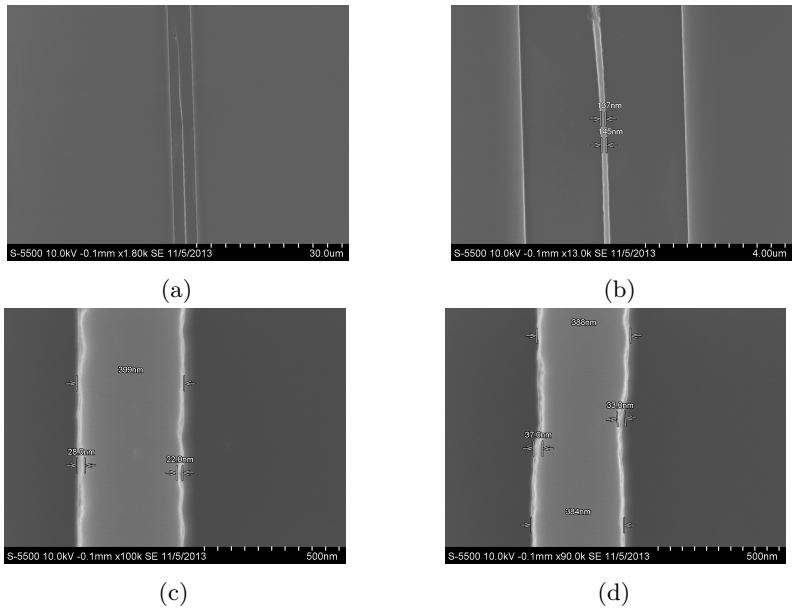

Figure 5.24: *(a) One of the tapered waveguides for sample L4.01. Significant deformation is observed. (b) Taper measurements before deformation. (c) Waveguide measurements. Width measured to be 399 nm and roughness to be 22 nm and 28 nm. (d) Write field misalignment measured to be ∼40 nm.*

Figure 5.25a shows the sidewall profile of the waveguide, with a width of 391 nm and an etch depth of 301 nm. The positive profile has decreased, but is still observable at the upper part of the sidewall. Decreasing the exposure dose while retaining the etch recipe and the mask thickness used previously indicates that the positive profiles are caused by overexposure of the mask. Some residual PMMA attached to the left sidewall can also be observed. In figure 5.25b a

round edge on top of the waveguide protruding to some extent from the sidewall can be observed. Figure 5.25c gives a view of the inner sidewalls of the racetrack resonator which displays roughness of similar magnitude and shows remnants of the PMMA mask on top of the resonator. It is evident that simply leaving the sample in acetone for ∼5 minutes is not enough to completely remove the PMMA, and that submerging the sample in acetone and then applying an ultrasonic signal to the acetone and sample might be necessary. Figure 5.25d shows the profile of a second resonator on the same sample but which does not display the rounded overhanging edge of the resonator in figure 5.25b. A thorough discussion on this phenomenon is given later.

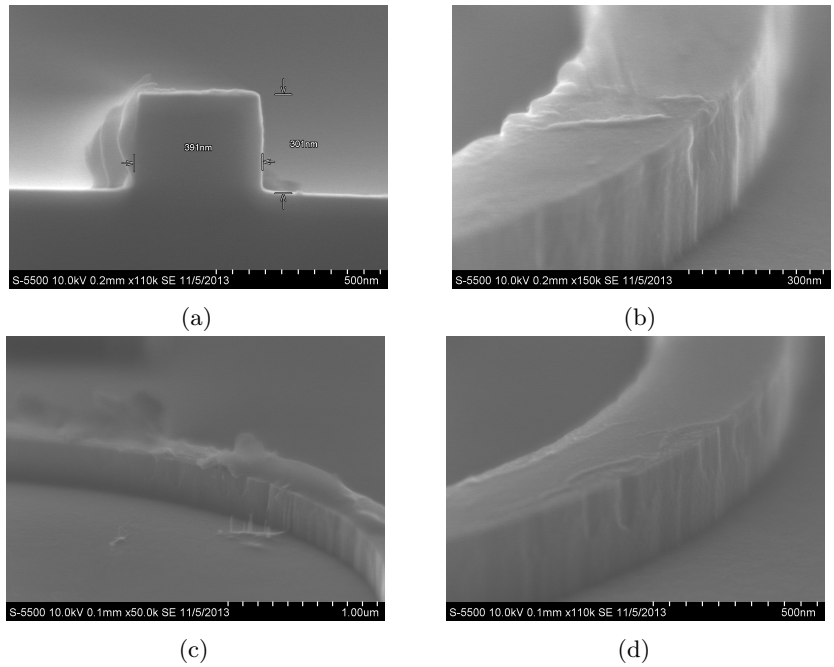

(a) (b)

(c) (d)

Figure 5.25: *(a) Width and height measurements. (b) Rounded overhanging edge and sidewall roughness. (c) Sidewall roughness on the inside. Significant amounts of resist residue left on the waveguide can be observed. (d) The rounded overhanging edge is not present at all locations.*

During the lithography process of this sample a misunderstanding of the Raith software was resolved. There are several ways of setting the exposure dose for a mask. It is possible to manually set the step size, dwell time, and the dose amount – the amount of energy delivered – for each element. The doses for each element is a function of step size, dwell time, and the beam current. For the area dose the function is

$$\text{Area Dose} = \frac{\text{Beam Current} \cdot \text{Area Dwell Time}}{\text{Area Step Size } U \cdot V}, \tag{5.17}$$

for the curve dose the function is

$$\text{Curve Dose} = \frac{\text{Beam Current} \cdot \text{Curve Dwell Time}}{(\text{Curve Step Size})^2}, \tag{5.18}$$

for the line dose the function is

$$\text{Line Dose} = \frac{\text{Beam Current} \cdot \text{Line Dwell Time}}{\text{Line Step Size}}, \tag{5.19}$$

and lastly for the dot dose the function is

$$\text{Dot Dose} = \text{Beam Current} \cdot \text{Dot Dwell Time}. \tag{5.20}$$

When the beam current has been input it is possible to automatically calculate and set the other values. However when this is done the doses for each element are set slightly off from the default values. This error will also have been scaled by the dose scale factor. Since the values would only slightly deviate from the default values, and a trial and error method based on the previous samples has been used, the consequences of the misunderstanding is not thought to be significant.

5.3 EBL exposure dose precedence test

The Raith software manual was ambiguous when explaining which dose scale factors take precedence. Therefore a test was devised to understand how the software handles dose changes in both the gds-file and in the position list. From this point the doses for the different elements were kept at their default values as seen in table 5.9 unless otherwise stated.

Table 5.9: The default doses for each element in the Raith software.

Element	*Dose*	*Unit*
Area	100.0	$^{\mu As}/_{cm^2}$
Curve	100.0	$^{\mu As}/_{cm^2}$
Line	450.0	$^{pAs}/_{cm}$
Dot	0.080	pAs

Sample L5.01 This sample was multi purposed as an exposure test as well as the exposure dose precedence test. The resist layer was spun on according to the recipe in table 5.8 using the 50/50 blend. The thickness was measured to be 252.2 nm with a g-factor of 0.9993. The sample was then exposed using the mask depicted in figure 4.7, with dose scale factors from 0.8 to 2.0 using a step of 0.2, which were changed in the position list. These were used as references as well as another exposure and etch test. In addition three extra sets of the same mask were exposed $\sim$100 μm above the reference exposures. The additional masks all had their dose scale factor changed in the gds-file to 1.6, however the dose scale factor given in the position list for these exposures were set to 1.0, 1.2, and 4.0, respectively. An image of the layout is given in figure 5.26. The three topmost tapers form the exposure dose precedence test.

Table 5.10: The dose precedence test set up. The tapers are numbered 1 to 3 from top left to top right in layout image.

Taper number	*.gds dose scale factor*	*Position list dose scale factor*
1	1.6	1.0
2	1.6	1.2
3	1.6	4.0

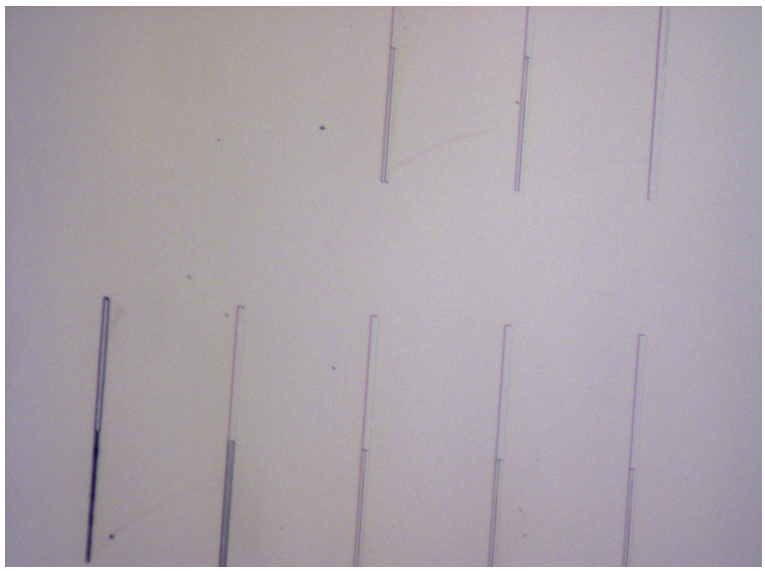

Figure 5.26: *The layout of the tapers after development. Dose scale factors of 0.8 to 2.0 on the bottom and the three precedence test exposures on the top with the 1.6/1.0 dose scale factor taper directly above the 1.6 reference taper.*

The sample was etched using the recipe in table 5.2 for 23 seconds, with a sapphire carrier. After the etch the PMMA mask layer thickness was measured to be 91.34 nm with a *g*-factor of 0.9993. This yields a PMMA etch rate of

$$\text{PMMA Etch rate} = \frac{252.2\ nm - 91.34\ nm}{23\ s} \cdot 60\ s = 419.63\ {}^{nm}/_{min}. \quad (5.21)$$

The tapered waveguide with exposure dose scale factors of 0.8 and 1.0 was underexposed to the point where no waveguides were discernible. Figures 5.27a to 5.27d show the reference tapers with exposure dose scale factors of 1.2 to 1.8, respectively. The T-shape observed in the figure is caused by a write field misalignment in v-direction. This T-shape would cause increased reflection losses when coupling into the tapered waveguide. Figure 5.28 shows the taper exposed with a dose scale factor of 2.0 being deformed. Figure 5.27d shows the taper tip to be very close to the desired width of 80 nm. However previous samples with

equivalent resist thickness had shown that a dose scale factor of 1.6 and 1.8 to be overexposing when using the mask in figure 4.6. This could indicate that the error imposed by setting the dose for the elements automatically is greater than assumed. However, another reason might be that there is something inherent in the different mask files that would have one mask require a lower dose scale factor than another.

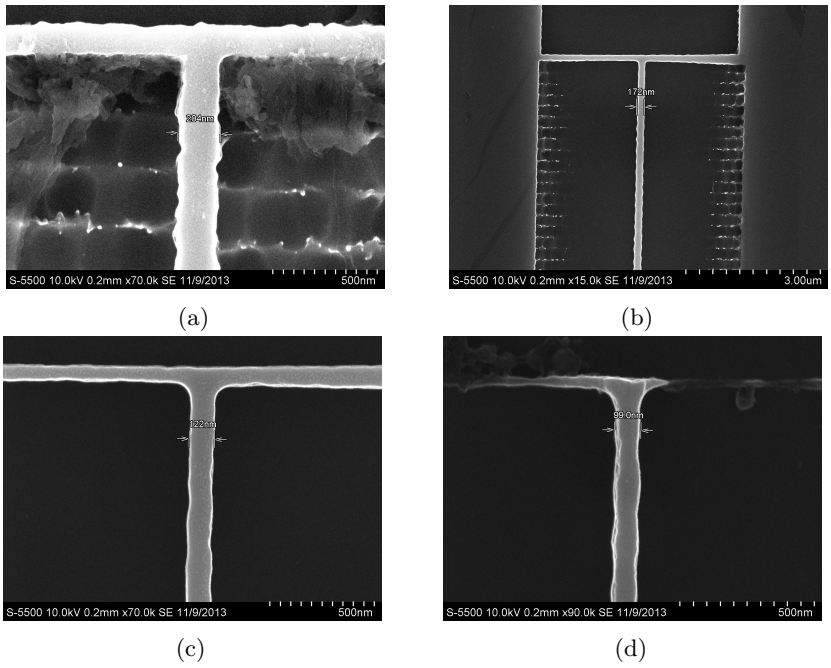

Figure 5.27: *(a) Taper tip exposed with dose scale factor of 1.2. (b) Taper tip exposed with dose scale factor of 1.4. (c) Taper tip exposed with dose scale factor of 1.6. (d) Taper tip exposed with dose scale factor of 1.8. A dose scale factor of 1.8 is closest to the desired waveguide width of 80 nm.*

As can be seen from figure 5.26, taper number 3 as per table 5.10 is overexposed to the point where there no longer is a tapered waveguide to be identified. Figure 5.29a shows that taper number 1 with its taper tip at a width of ∼122 nm appears to be closer to an optimal dose when compared with the reference taper exposed with a dose scale factor of 1.6 shown in figure 5.27c. This could

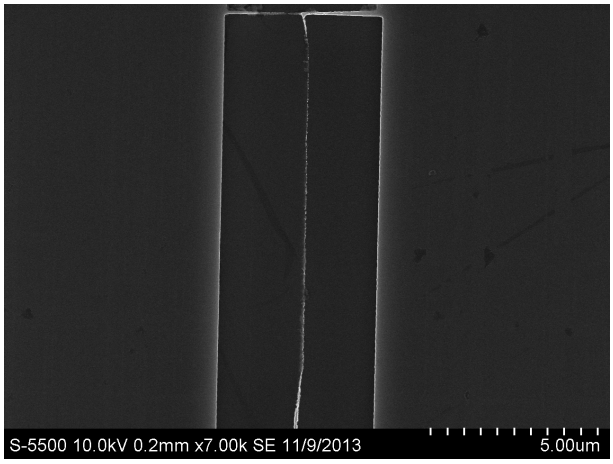

Figure 5.28: *The tapered waveguide exposed with a dose scale factor of 2.0. Significant deformation along with disintegration is observed.*

be due to differences in resist thickness, however since the tip of the two tapers in question are only ∼200 μm apart this seems improbable.

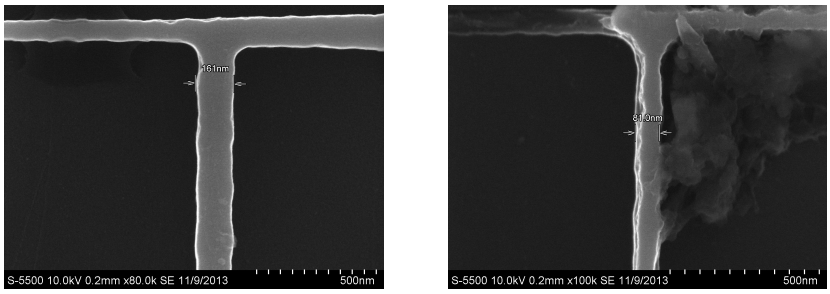

(a) (b)

Figure 5.29: *(a) The tip of the tapered waveguide with a dose of 1.6/1.0. (b) The tip of the tapered waveguide with a dose of 1.6/1.2.*

When investigating taper number 2 shown in figure 5.29b the tip width of ∼80 nm indicates near perfect dosage. And when compared with the reference

waveguides this dose should be somewhere between a dose scale factor of 1.8 and 2.0, discounting any difference in the thickness of the resist layer. This could indicate that the relation between the dose scale factor set in the gds-file and the dose scale factor set in the position list is

$$\text{Actual DSF} = \text{gds DSF} \times \text{p.l. DSF} = 1.2 \cdot 1.6 = 1.92. \tag{5.22}$$

If the DSF is not set to a value in the gds-file it appears to be ignored.

5.4 Lowering the dosage

To investigate if the need for a lower dose for the larger mask is connected to the set doses slightly deviating from the default values, samples with equal PMMA layer thickness were made. The mask in figure 4.6 was exposed while lowering the dose scale factors and keeping the doses for each element at the default values. If the lowered dose factors cause the mask to be underexposed, it becomes more likely that the error in dose values caused the issue.

Sample L5.02 The resist layer was spun on using the recipe in table 5.8 with the 50/50 resist blend. The thickness of the PMMA layer was measured to be 255.9 nm with a g-factor of 0.9969. The sample was then exposed using the mask depicted in figure 4.6 twice, approximately 100 μm apart. The dose scale factors in the position list were set to 1.4 for the first one and 1.5 for the second one. The sample was then etched for 20 seconds using the recipe from table 5.2 with a sapphire carrier. After the etch the PMMA layer thickness was measured to be 124.0 nm with a g-factor of 0.9996. This gives a PMMA etch rate of

$$\text{PMMA Etch rate} = \frac{255.9\ nm - 124.0\ nm}{20\ s} \cdot 60\ s = 395.7\ {}^{nm}/_{min}. \tag{5.23}$$

From figures 5.30a and 5.30b the etch depth is observed to be 275 nm. This gives a silicon etch rate of

$$\text{Silicon Etch rate} = \frac{275\ nm}{20\ s} \cdot 60\ s = 825\ {}^{nm}/_{min}, \tag{5.24}$$

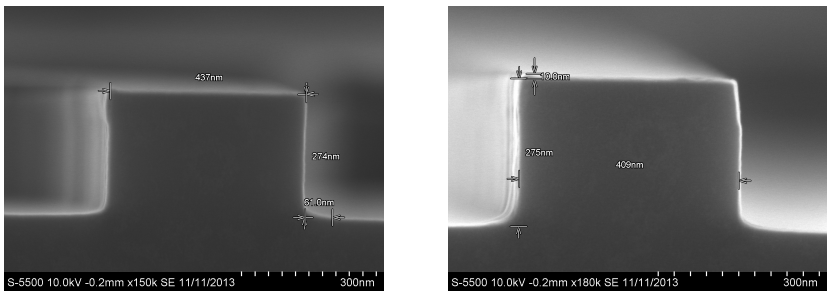

(a) (b)

Figure 5.30: *(a) Measurements of the waveguide exposed with a dose scale factor of 1.4. (b) Measurements of the waveguide exposed with a dose scale factor of 1.5.*

and a selectivity of

$$\text{Selectivity} = \frac{825\ nm}{395.7\ nm} = 2.085 \approx 2.1. \tag{5.25}$$

Figure 5.30b shows the waveguide having been exposed with a dose scale factor of 1.5. A slight positive profile can be observed on the rightmost sidewall. In figure 5.30a, which shows the waveguide exposed with a dose scale factor of 1.4, no such positive profile is observable. This could indicate that the hypothesis in the discussion of sample L4.01 that the positive profiles are caused by significant overexposure is accurate. When compared to the results from samples L4.02 and L4.01 it could also indicate that positive sidewall profiles are related to both exposure dose and etch time. Sample L4.02 was exposed with a dose scale factor of 1.8 for the normal waveguides and was etched for 27 seconds. Sample L4.01 was exposed with a dose scale factor of 1.6 for the normal waveguides and was etched for 23 seconds. As can be seen in figure 5.20c the positive profile extends from the top to approximately the middle of the waveguide, while figure 5.25a shows the positive profile ending before reaching the middle of the waveguide. That the etch time has been reduced while the sidewall profiles have improved should not be overlooked.

To investigate the sidewall profiles in the coupling region the sample has been broken across the racetrack resonator as shown in figure 5.31. From figure 5.32 a roundness at the base between the waveguides as well as a slightly more shallow

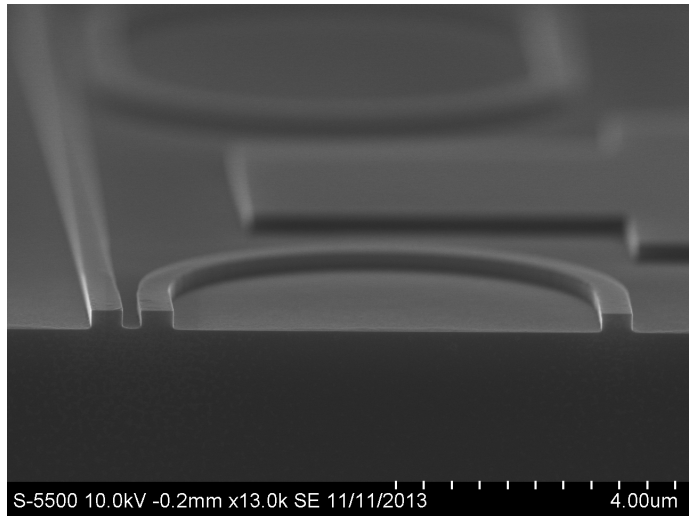

Figure 5.31: *Cross-section SEM of the racetrack resonator exposed with a dose scale factor of 1.4. The profile of the coupling region is shown and a rounding of the trench can be observed between the two waveguides.*

etch depth can be observed. The more shallow etch is caused by micro-loading, a depletion of free radicals, which is explained in section 3.4.2. The roundness of the trench occurs because the etch is slightly isotropic. A shelf can also be observed on the rightmost waveguide in the top left corner. Figures 5.33a to 5.33d show a selection of the characterization results of the waveguides exposed with a dose scaling factor of 1.4. Figure 5.33a shows that the width of the waveguide is still diminished due to overexposure and that roughness size is below 10 nm. Figure 5.33b shows the effect of negative write field misalignment. The alignment in v-direction is such that the tapered waveguide has received double exposure for a small section and consequently leaving a gap between write fields. The u- and v-directions are the relative x- and y-directions, respectively, taking sample angle and origin correction into account. Aside from not being aligned, this is the worst possible type of misalignment as a gap in the waveguide would cause major reflections and scattering. Deformation can also be spotted further along the tapered waveguide. Figures 5.33c and 5.33d show the sidewall of the resonator and are discussed along with the next set of figures. Figures 5.34a to 5.34c show some of the characterization results of the waveguides exposed with

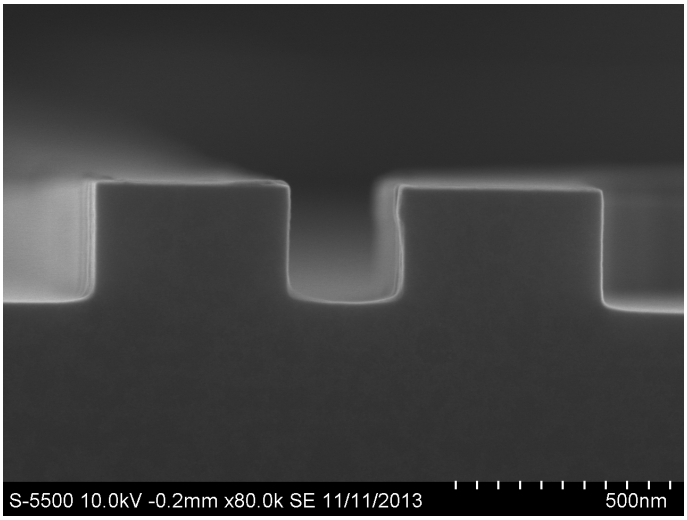

Figure 5.32: *The sidewall profiles of the coupling region. A rounded trench between the waveguide and the resonator can be observed. The sidewalls are near 90° on the outer and inner walls. Because of the round top edge the sidewall profile appear negative, however a closer look reveal that they are straight.*

a dose scaling factor of 1.5. Figure 5.34a shows the waveguide to be overexposed and the roughness size to be up to ∼25 nm. Figure 5.34b shows the roughness to be nearly causing a gap in the tapered waveguide. A shelf effect can be observed in figures 5.32, 5.33c, 5.34c, and 5.34d. This phenomenon appears to be randomly localized. It appears to be more prominent around the resonators but can also be seen in figure 5.30b, though to a lesser extent. This has been discussed at length with the NanoLab engineers, however no definitive answer has been found to what causes of the effect. The random locations, the straight sidewall profile below the shelf, and the fact that the edge rises upwards before continuing down the sidewall suggests that it is unlikely that this is caused by ion shadowing and the bottling effect[44]. Ion capturing may be the cause of this phenomenon as the surface mobility of fluorine atoms decreases with temperature[44]. Another cause might be a combination of local hot spots and compounded sidewall deposition of either silicon-passivation reaction products or resist-passivation reaction products. Surface temperatures influence re-deposition of reaction products on feature surfaces[57], so a local hot spot would cause

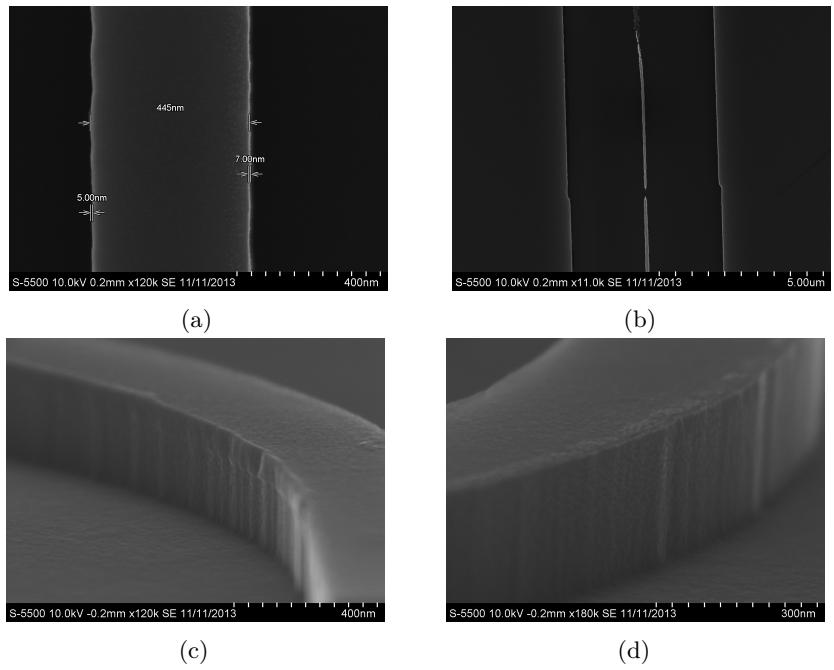

Figure 5.33: *The waveguides exposed with a dose scale factor of 1.4. (a) Width and roughness measurement. Width measured to be 445 nm, and roughness to be between 5 and 7 nm. (b) A gap in the tapered waveguide left by negative write field misalignment in v-direction. (c) A shelf on the edge of the waveguide can be observed. (d) Amorphous material deposited on the waveguide.*

more deposition on the sidewall. More material could then deposit on top of the sidewall ledge to form the observed hill. This seems unlikely as the local temperature differences would have to be several tens of degrees for this amount. Another possibility is that the shelf has formed from PMMA resist redepositing on the edge during removal after the etching process. In future work the samples should be cleaned in a sonic bath to eliminate any possibility that there is resist left on the sample during characterization.

The amorphous appearing material containing small spots deposited on the sidewall and top inner edge of the waveguide observed in figure 5.34c is most likely a passivation product, a polymer consisting of CF_i bonds where i=1,2,3[46]. However it could also contain carbon and sulphur[45]. The signs of deposition

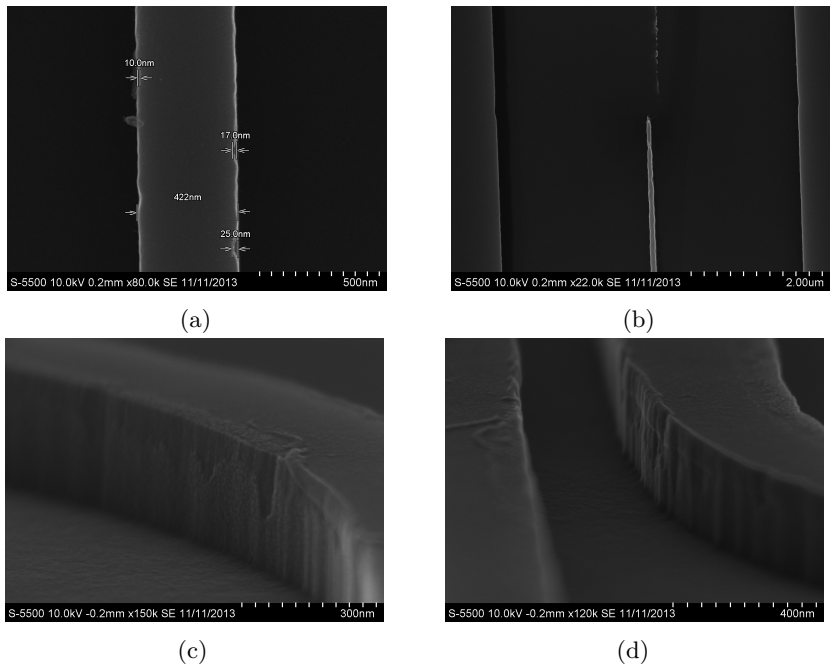

Figure 5.34: *The waveguides exposed with a dose scale factor of 1.5. (a) Width and roughness measurement. Width measured to be 422 nm, and roughness to be between 10 and 25 nm. (b) Tip of the tapered waveguide (c) Amorphous deposits deposited on the waveguide introducing more roughness. (d) Pronounced shelf located at a bend on the racetrack resonator.*

on top of the waveguide are curious. There should be no deposition on top of the waveguide as there should still be a relatively thick mask layer left after the etch. This could be due to poor mask adhesion locally. Conceivably the polymer barrier could form before fluorine radicals arrived to form SiF_4. At the time of writing this phenomenon has been shown to an international dry etch forum through the NTNU NanoLab, however no answers of what could cause the phenomenon have been received. The shaping of the passivation product introduces more roughness on the waveguide sidewall. The refractive index of the passivation product for the 1550 nm wavelength determines the significance of this roughness.

Sample L5.03 The purpose of this sample is to lower the dose further and investigate if underexposure can be achieved using the larger mask. The resist was spun on according to the recipe in table 5.8 using the 50/50 resist blend. The thickness of the resist layer was measured to be 250.5 nm with a g-factor of 0.9995. The sample was then exposed using the mask depicted in figure 4.6 three times, approximately 100 μm apart. Lowering the doses the dose scaling factors were set to 1.1, 1.2, and 1.3. The sample was then etched for 20 seconds according to the recipe in table 5.2 using a sapphire carrier. After the etching process the PMMA layer thickness was measured to be 106.8 nm with a g-factor of 0.9991 yielding a PMMA etch rate of

$$\text{PMMA Etch rate} = \frac{250.5\ nm - 106.8\ nm}{20\ s} \cdot 60\ s = 431.1\ {}^{nm}/_{min}. \qquad (5.26)$$

The results of the profilometer scan over the scratch in the sample are given in figure 5.35 showing a silicon etch depth of ∼301 nm. This gives a silicon etch

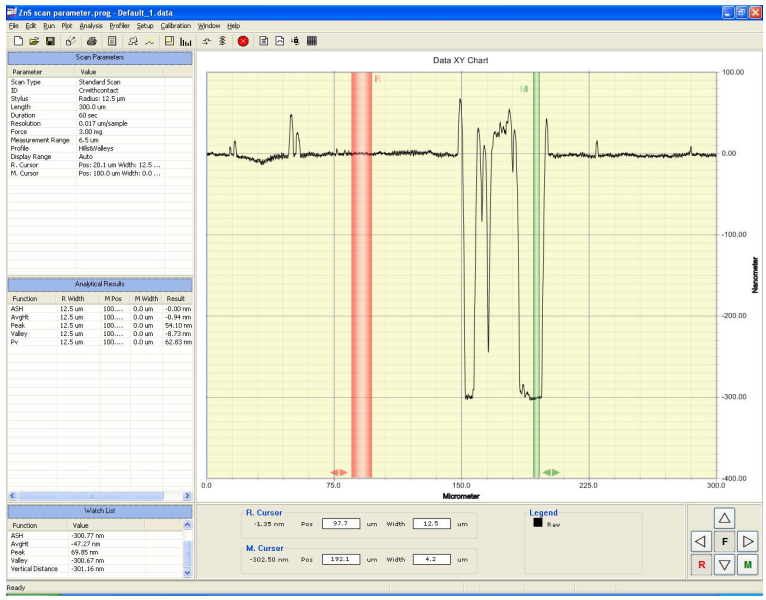

Figure 5.35: *Profilometer scan of the silicon etch depth.*

rate of

$$\text{Silicon Etch rate} = \frac{301.16\ nm}{20\ s} \cdot 60\ s = 903.48\ {}^{nm}/_{min}, \tag{5.27}$$

and a selectivity of

$$\text{Selectivity} = \frac{903.48\ nm}{431.1\ nm} = 2.096 \approx 2.1. \tag{5.28}$$

Figures 5.36a to 5.36d show the waveguides exposed at a dose scaling factor of 1.1. A slight underexposure is apparent from the figures showing a waveguide width between 507 nm to 514 nm, roughness size of ∼20 nm, and lines along the trenches connecting to the waveguides. Residual resist and dust particles are observable in figures 5.36b and 5.36c to the point where it is difficult to differentiate between roughness and contamination along the tapered waveguide in figure 5.36b. There is also an indication of the shelf phenomenon along parts of the inside of the resonator in figure 5.36d.

Figures 5.37a to 5.37d show the waveguides exposed at a dose scaling factor of 1.2. Figures 5.37a and 5.37b show some overexposure measuring the waveguide width to be ∼475 nm. This implies that the desired exposure dose for a mask thickness of ∼250 nm lies between a dose scaling factor of 1.1 and 1.2 when using the default dose values. The measure of roughness in figure 5.37a is difficult to trust as it is impossible to discern anything between the measuring lines. Figure 5.37b displays ∼90° sidewalls. Figures 5.37c and 5.37d show the amorphous, spotted material to only be deposited on the sidewalls and an extremely thin layer of resist on top of the waveguides, even forming a suspended membrane in the coupling region. These observations strengthen the hypothesis that the shelf phenomenon is due to residual resist, and that the amorphous looking material observed on this and the previous sample is the passivation polymer from the CHF_3 chemistry in the plasma. Figures 5.38a to 5.38d show the waveguides exposed with a dose scaling factor of 1.3 and are included as a reference. Figure 5.38b shows further overexposure with a measured width of 456 nm. The effect of micro-loading can also be observed and are measured as a trench depth difference of 7 nm.

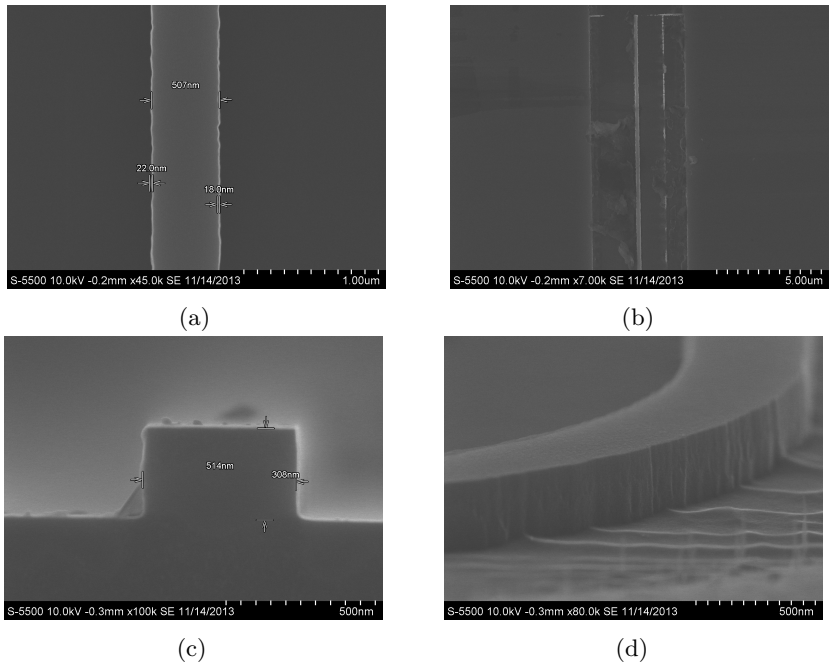

(a) (b)

(c) (d)

Figure 5.36: *The waveguides exposed with a dose scale factor of 1.1 showing signs of underexposure. (a) Width and roughness measurements. Width is measure to be 507 nm and roughness to be between 18 nm and 22 nm. (b) Tapered waveguide. (c) Cross-section measurements and profile. Width measured to be 517 nm and height to be 308 nm. (d) Ridging at the bottom of the trench indicating underexposure.*

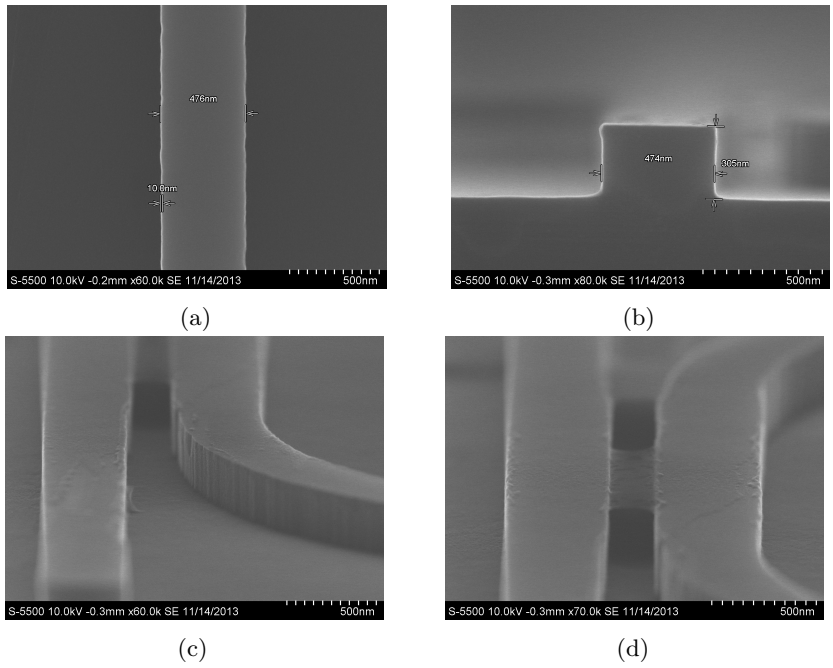

Figure 5.37: *The waveguides exposed with a dose scale factor of 1.2 showing signs of overexposure. (a) Width and roughness measurements. Width is measure to be 476 nm and roughness to be approximately 10 nm. (b) Cross-section measurements. Width measured to be 474 nm and height to be 305 nm. (c) Passivation layer observed to only be deposited on the sidewalls. (d) A thin layer of residual resist deposited on top of the waveguides forming a thin bridge between the waveguides.*

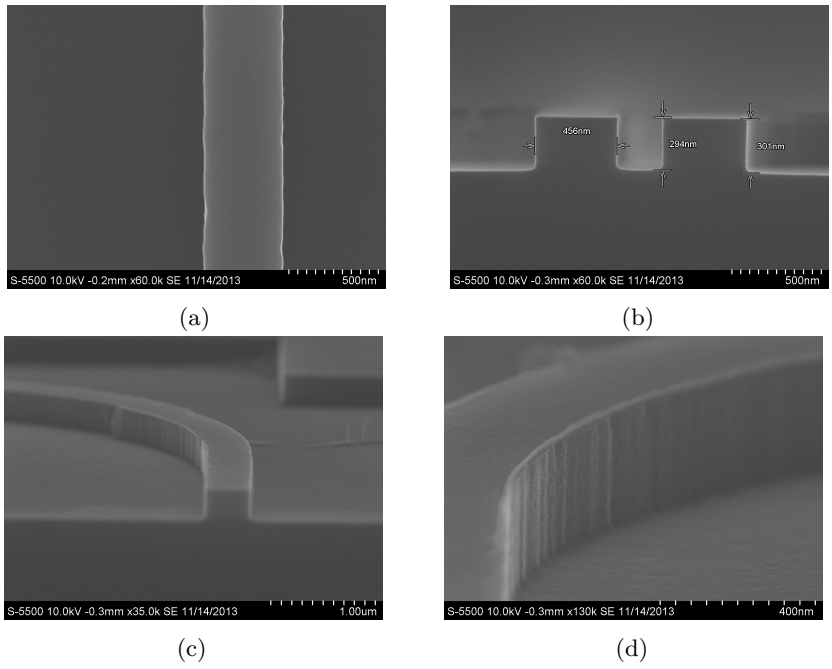

(a) (b)

(c) (d)

Figure 5.38: *The waveguides exposed with a dose scale factor of 1.3 showing overexposure. (a) Waveguide showing some roughness (b) Cross-section measurements and profile. Width measured to be 456 nm. The effects of microloading can be observed between the waveguides. (c) & (d) Reference sidewall roughness for the racetrack resonators. The passivation layer on the sidewalls and a thin layer of PMMA on top of the waveguides can be observed.*

5.5 Line dose experiment

The NanoLab engineer responsible for lithography suggested a line dose of 300 $\frac{pAs}{cm}$ as a good starting point instead of the default 450 $\frac{pAs}{cm}$. As the default value is 50% higher than the dose suggested by the engineer the line dose was changed to 300 $\frac{pAs}{cm}$ for sample L5.04.

Sample L5.04 The resist was spun on using the recipe in table 5.8 and the 50/50 resist blend. The resulting PMMA layer was measured to be 277.0 nm with a g-factor of 0.9993. The sample was then exposed using the mask depicted in figure 4.6 three times. These were placed approximately 100 μm apart, meaning 100 μm from the lower right corner of the previous exposure to the lower left corner of the next exposure. The dose factors were set to 1.2 for the first exposure, 1.25 for the second exposure, and 1.3 for the third exposure. The results from the previous sample indicated that a dose scaling factor between 1.1 and 1.2 would be close to the desired exposure dose. However the mask thickness of this sample is ∼37 nm thicker than the previous sample, therefore dose scaling factors between 1.2 and 1.3 is investigated instead. The sample was etched for 20 seconds according to the recipe in table 5.2 using a sapphire carrier. After the etch the resist layer was measured to be 132.3 nm with a g-factor of 0.9995 giving a PMMA etch rate of

$$\text{PMMA Etch rate} = \frac{277.0\ nm - 132.3\ nm}{20\ s} \cdot 60\ s = 434.1\ {}^{nm}/_{min}. \tag{5.29}$$

In figure 5.40b the silicon etch is measured to be 298 nm. This yields a silicon etch depth of

$$\text{Silicon Etch rate} = \frac{298\ nm}{20\ s} \cdot 60\ s = 894\ {}^{nm}/_{min}, \tag{5.30}$$

and a selectivity of

$$\text{Selectivity} = \frac{894\ nm}{434.1\ nm} = 2.059 \approx 2.05. \tag{5.31}$$

Figures 5.39a to 5.39d show the waveguides exposed with a dose scaling factor of 1.2. The figures show signs of severe underexposure, giving an angled view on the connected silicon pillars made from the underexposure. Figures 5.40a to 5.40d show the waveguides exposed with a dose scaling factor of 1.25. Signs

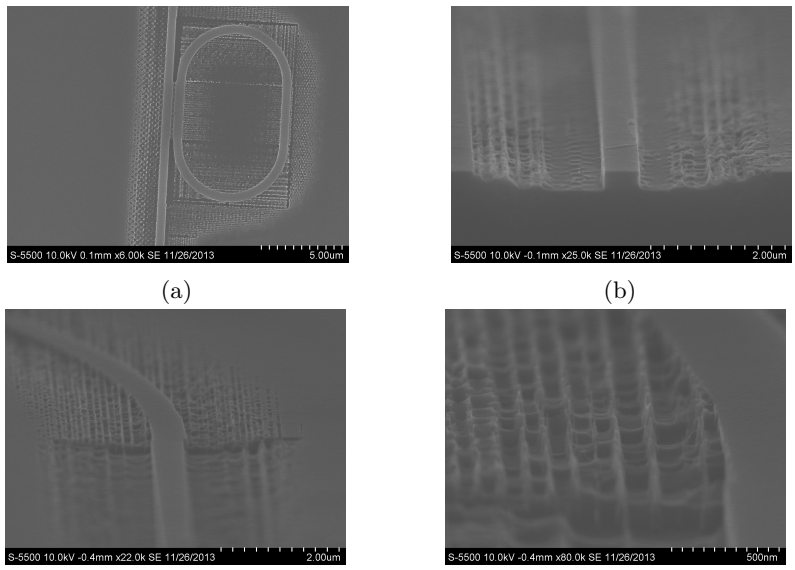

(a) (b)

(c) (d)

Figure 5.39: *The waveguides exposed with a dose scale factor of 1.2 showing significant underexposure.*

of underexposure are still observable from the connected silicon pillars and the increased waveguide width. Figure 5.40b shows the measured waveguide width to be 489 nm. Compared with the measured width of 527 nm in figure 5.40a the difference is in the order of ∼40 nm, which is quite significant. Figures 5.41a to 5.41d show the waveguides exposed with a dose scaling factor of 1.3. There are still signs of underexposure, though they are very slight. These are the increased roughness shown in figure 5.41c and the hills around the outer edge of the trenches in figure 5.41d. The width of the waveguide is measured to be different in three separate locations in figures 5.41a, 5.41b, and 5.41c, ranging from 500 nm to 445 nm. Along with the difference measured in the previous exposure this could indicate poor resist uniformity, the layer being thinner in the middle where the sample was scribed and broken, and thicker towards the edge of the sample. The underexposures are most probably only related to the mask thickness, as most of the elements would be exposed using the area dose. Any area larger than the step size of the beam would use the area dose. Changing

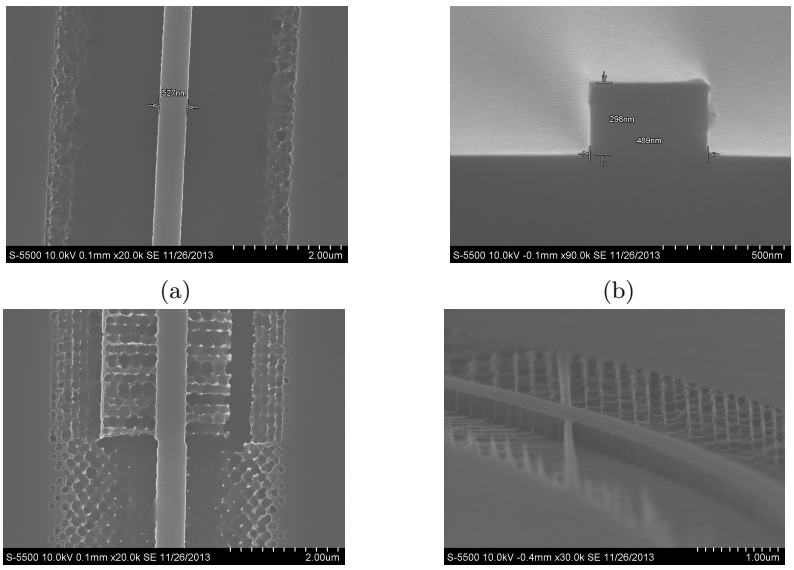

(a) (b)

(c) (d)

Figure 5.40: *The waveguides exposed with a dose scale factor of 1.25 showing underexposure. (a) Width of the waveguide measured to be 527 nm. (b) Cross-section measurements showing a width of 489 nm and a height of 298 nm, and straight profiles. (c) Beginning of the tapered waveguide. (d) Bends still indicate significant underexposure with silicon pillars reaching the waveguide in certain locations.*

the line dose would only affect the edges of the elements exposed[56]. Because of the underexposure it is difficult to discern if the increased roughness along the sidewalls is caused by reducing the line dose or if it is a product of the general underexposure.

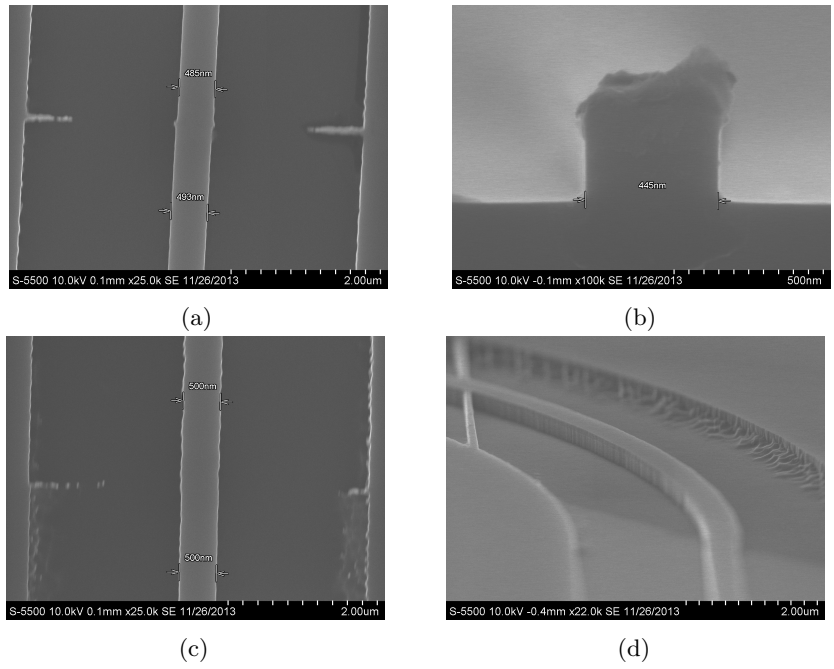

(a) (b)

(c) (d)

Figure 5.41: *The waveguides exposed with a dose scale factor of 1.3. (a) & (c) The width measured at two write field junctures. The measurements range from 485 nm to 500 nm. Excellent write field alignment can also be observed. (b) A cross-section view of the waveguide show straight sidewalls and another width measurement measuring 445 nm. (d) Some underexposure at the outer edge of the trenches.*

Sample L5.05 Since the question if different masks needs different exposure doses has not yet been answered definitively, this sample was used to investigate if different masks with identical doses would present different levels of over-/underexposure. The resist was spun on according to the recipe in table 5.11 using the 33/66 resist blend. The resist layer thickness was measured to be 186.5 with a g-factor of 0.995. The reason for switching resist blend and recipe was that 20 seconds of etching appeared to only remove ∼150 nm of resist indicated by results of the previous samples. Therefore a resist layer thickness of ∼200 nm should be sufficient. The exposure was set up so that each of the masks in figures 4.6, 4.7, and 4.3 were each exposed three times, with dose scaling factors of 1.1, 1.2, and 1.3. The smaller masks were placed in the middle of the sample. The dose settings were according to table 5.9. For this exposure the mask in figure 4.6 had been updated by widening the taper tips to be 150 nm and adjusted the area before and after the coupling area for the racetrack resonators to no longer double expose a small region. The reason for widening the taper tips to 150 nm was to investigate if it would improve the tip profile and reduce roughness. Guanghui Ren et al.[51] show that increasing the tip width to 150 nm will increase reflections by approximately 1 dB when coupling into the tip. However coupling light through the taper will still be feasible despite the losses gained from this increase.

Table 5.11: The seventh spin recipe.

Sequence	*Spin speed[RPM]*	*Time[s]*
1	500	12
2	2000	60

After the exposure the sample was etched for 20 seconds according to the recipe in table 5.2 using a sapphire carrier. After the etch the thickness of the resist layer was measured to be 43.67 nm with a g-factor of 0.9911. This yields a PMMA etch rate of

$$\text{PMMA Etch rate} = \frac{186.5\ nm - 43.67\ nm}{20\ s} \cdot 60\ s = 428.49\ {}^{nm}/_{min}. \quad (5.32)$$

Figure 5.42a shows the resonator exposed with the mask in figure 4.6 after the adjustment. Figure 5.42b shows the mask in figure 4.3 which did not receive any adjustments. In figure 5.42b a small indentation on the right side of the

waveguide before and after the coupling region can be observed. This is a result of overlapping elements in the mask which is not present in figure 5.42a.

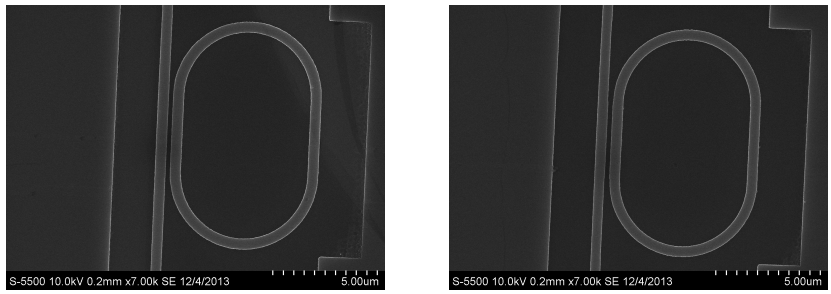

(a) (b)

Figure 5.42: *Racetrack resonators exposed with a dose scale factor of 1.3. An indentation can be observed in (b) which is not present in (a).*

Figures 5.43, 5.44, and 5.45 are ordered such that figure a is the exposure with the mask in figure 4.6, figure b is the exposure with the mask in figure 4.7, and figure c is the exposure with the mask in figure 4.3. Figures 5.43a to 5.43c show the three masks exposed at a dose scaling factor of 1.1. All show signs of underexposure. The exposure in figure 5.43a has a width of ∼530 nm and the trenches are not fully etched. Figure 5.43b shows the tip to have a width slightly less than ∼230 nm.

When exposing the mask in figure 4.7 the mask was started 100 μm below the mask in figure 4.3. However the tapers and following trench are together 200 μm long. This means that the large trench in the mask in figure 4.7 was placed on top of the leftmost waveguide in figure 4.3. This places the taper tip directly below a double-exposed area. This is most likely the reason why the trenches are better developed around the tip of the taper as they have received a greater amount of scattered electrons from the proximity effect. This is true for all the exposures of the taper mask. Figure 5.43c shows better developed trenches, however the width of the waveguides are still of the same order, ∼525 nm.

These results indicate that the masks themselves do not need different exposure doses. For this exposure, the larger mask appeared to need a larger exposure dose than the smaller masks while for previous samples the reverse had seemed the case. For the exposures with a dose scaling factor of 1.1 the smaller masks

were located ∼2 mm to the right of the mask, while for the exposures with a dose scaling factor of 1.3 the distance between the large and small masks had been ∼500 μm. For the exposures with dose scaling factor of 1.2 the distance between the masks was ∼1 mm.

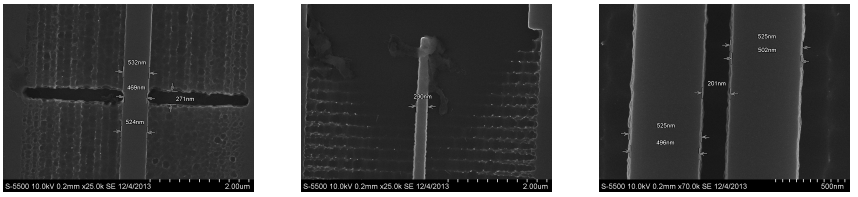

(a) (b) (c)

Figure 5.43: *The three different masks exposed with a dose scale factor of 1.1, all showing underexposure. (a) Measurements of a waveguide from the larger mask shows a width between 524 nm and 532 nm. (b) Tip width of the tapered waveguide from the taper mask measured to be approximately 230 nm. (c) Coupling region of a resonator from the small resonator mask. The width of the waveguides measured to be approximately 525 nm.*

Figures 5.44a to 5.44c show some underexposure with widths greater than 500 nm, however as with figure 5.43 the smaller masks appear to be less underexposed than the larger. The tip of the tapered waveguide appears to be more developed which is probably due to proximity effects from the double exposure above.

Figure 5.45a shows the width of the waveguide from the larger mask to be ∼505 nm, very slightly underexposed. Figure 5.45b shows the taper tip to be fairly overexposed at a width of 57 nm. And figure 5.45c shows the width of the waveguide from the smaller mask to be slightly overexposed with a width of ∼490 nm. These results confirms that for this sample the larger mask needs a larger exposure dose than the smaller masks, while for previous samples the reverse had seemed the case. Clearly the different masks are exposed in areas of different resist thickness. This indicates further that the need for different exposure doses is not a consequence of using different masks of different sizes, but that the exposure dose is dependent on resist thickness and, to a certain degree, proximity effects. The exposure dose is dependent on resist layer thickness to such a degree that a difference in resist thickness of 20 nm could render a waveguide unusable. If the resist uniformity cannot be controlled adequately one

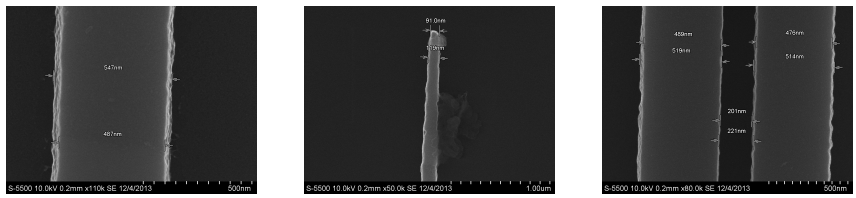

(a) (b) (c)

Figure 5.44: *The three different masks exposed with a dose scale factor of 1.2. (a) Measurements of a waveguide from the larger mask shows a width between 487 nm and 547 nm. (b) Tip width of the tapered waveguide from the taper mask measured to be 91 nm. (c) Coupling region of a resonator from the small resonator mask. The width of the waveguides measured to be between 476 nm and 519 nm.*

could attempt to overexpose and account for 20-30 nm width reduction in the mask design.

Figure 5.46 show the sidewalls of the tapers produced by exposing the mask in figure 4.6. The first set of images is of the ones exposed at a dose scaling factor of 1.1, the second set at 1.2, and the third set at 1.3. At a dose scale factor of 1.1 the trenches have barely been etched at all. At a dose scale factor of 1.2 the trenches are still not etched completely and the waveguide features exhibit positive sidewall profiles. At a dose scale factor of 1.3 the tapered waveguide shows approximately straight sidewall profiles and fully etched trenches. In figure 5.46e there appears to be an issue with aligning the elements the taper consists of, producing a feature that resembles a waveguide next to the tapered waveguide. As the spot size converter would cover both the tapered waveguide as well as this undesired feature, it presents a problem during testing and operation. The etch depth measurements shown in these figures may not be accurate as the sample is angled, presenting difficulties identifying the bottom of the taper when viewing the front of the tip.

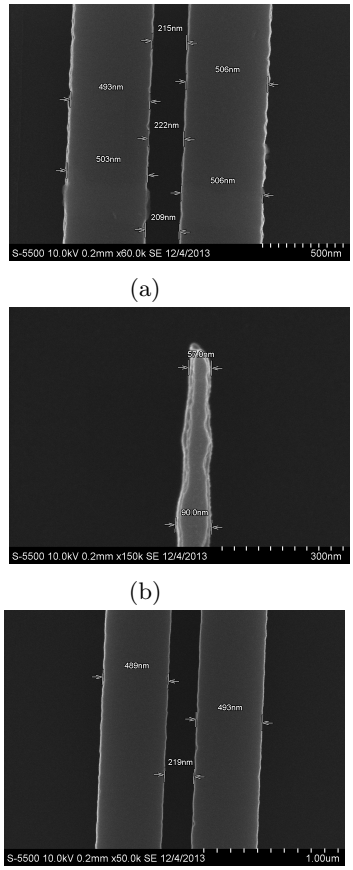

(a)

(b)

(c)

Figure 5.45: *The three different masks exposed with a dose scale factor of 1.3. (a) Measurements of the waveguides in the coupling region from the larger mask shows a width between 493 nm and 506 nm. (b) Tip width of the tapered waveguide from the taper mask measured to be 57 nm. (c) Coupling region of a resonator from the small resonator mask. The width of the waveguides measured to be between 486 nm and 493 nm.*

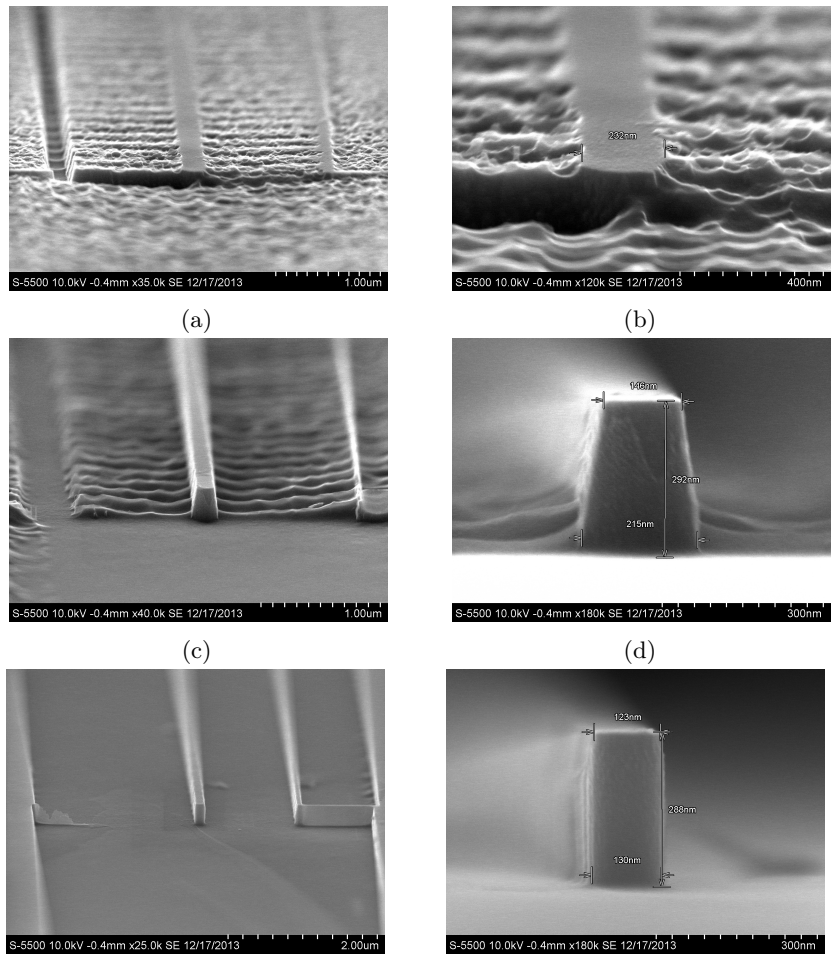

Figure 5.46: *Tapers from the larger mask with dose scale factors of (a) & (b) 1.1, (c) & (d) 1.2, and (e) & (f) 1.3. (a) & (b) The underexposure caused the etching process to barely etch a pattern. The discernible width of the tapered waveguide is approximately 232 nm. (c) & (d) Significant underexposure is evident from the silicon ridges protruding from the waveguide. The taper features positive sidewall profiles and a width between 146 nm and 215 nm. (e) & (f) Some overexposure is evident from the width of the tip being approximately 130 nm. The sidewall profile appears reasonably straight, however it is difficult to discern the exact profile because of the angle and the taper widening in the background.*

As can be seen in figure 5.47 the changes in mask thickness can be quite significant. The two waveguides are $\sim$50 μm apart however they both present the same indentation at approximately the same location along the waveguide. A faint stripe can be observed between the waveguides. This could indicate that between the waveguides the unexposed resist layer was barely etched through. Proximity effects account for the deeper indentation in the waveguides. The stripe between the waveguides is slightly more prominent at the edge of the trenches, however the proximity effect is less significant at the edge of the trenches than it is in the middle at the waveguides.

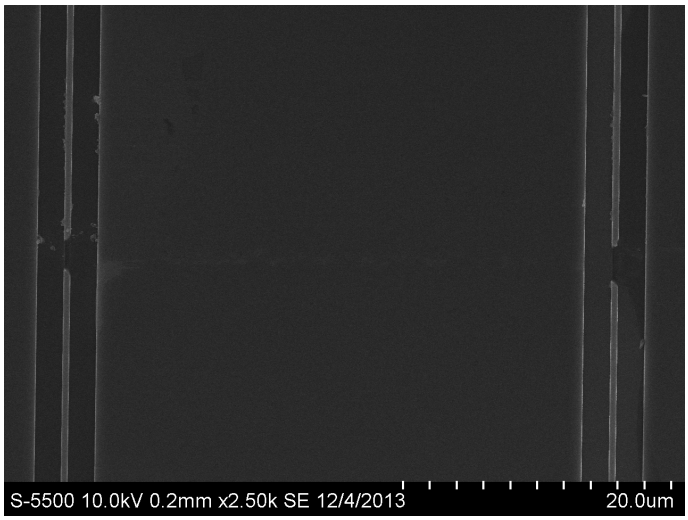

Figure 5.47: *Indentations in the same plane for both waveguides indicates an area of decreased resist layer thickness.*

Spot-Size Converter The purpose of this sample was to be a test of the potential for hardened S1818 to be used as spot-size converters. The spot-size converters were made using UV-lithography. A 50 mm silicon wafer was spun at 1500 RPM for 50 seconds using the S1818 resist and then soft baked at 115$^{\circ}C$ for 60 seconds. The target thickness was 3 μm, however the thickness could not be measured as the lamp in the refractometer had stopped working. Then edge bead removal was performed by putting a piece of silicon on top of the resist mask and exposing the edge with $\sim$1100 $\frac{mJ}{cm^2}$. The sample was then developed

using MF 26A developer until the edge disappeared. The edge did not disappear completely, however since the edge bead no longer touched the rest of the mask the rest of the edge bead could be removed using a small sponge with acetone. The sample was then rinsed with DI water and soft baked at $115°C$ for another 60 seconds. Using a test mask the sample was then exposed with $\sim$150 $\frac{mJ}{cm^2}$. The sample was developed for $\sim$2 minutes using MF 26A developer. Lastly the masked resist layer was hard baked at $125°C$ for 5 minutes. The resist layer had become cloudy, as shown in figure 5.48, before being exposed the second time. Since it became less cloudy during hard bake, this was most likely caused by the resist becoming hydrated during the DI rinse.

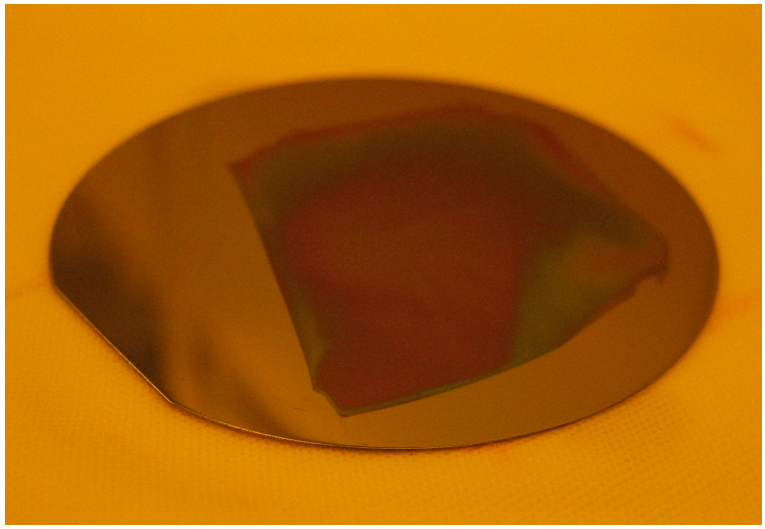

Figure 5.48: *S1818 resist layer after edge bead removal.*

Figures 5.49a and 5.49b show the cross-section measurements of a 3 μm resist line and of a 4 μm resist line, respectively. The lines exhibit significant positive sidewall profiles and rounded tops. This may have been caused by the resist becoming cloudy. Assuming this was caused by hydration light would experience more scattering and absorption as it enters the resist. Both the lines height is measured to be $\sim$2 μm a micron lower than desired. The width of the 3 μm line is measured to be 2.58 μm at the top and 5.63 μm at the bottom. The width of the 4 μm line is measured to be 3.31 μm at the top and 6.91 μm at the bottom.

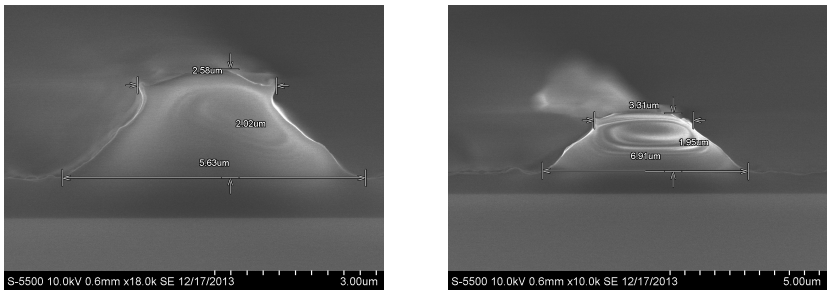

(a) (b)

Figure 5.49: *Cross-section measurements of (a) 3 µm line and (b) 4 µm line. Large positive sidewall profiles and round tops are observed.*

Figure 5.50 shows an angled view of one of the resist lines. Resist in the trenches can be observed indicating that the resist is underexposed. This explains the lower height measured for the resist lines. When comparing to the measurements seen in figures 5.49a and 5.49b, however, the tops appear overexposed while the bottom appears underexposed. This could be a result of more absorption and backscattering from water vapour. Less UV-light reaches the bottom of the resist and because of backscattering more light exposes the top layer of the resist. It is also safe to assume that the optimal dose was not applied on the first attempt. Therefore the dose could be under- or overexposing the resist despite the added challenge of water vapour in the resist. Unfortunately there was only time to do one trial run to make the spot-size converters. The method retains potential however, as Magnus Breivik[58] has demonstrated resist lines of comparable size with more desirable sidewall profiles.

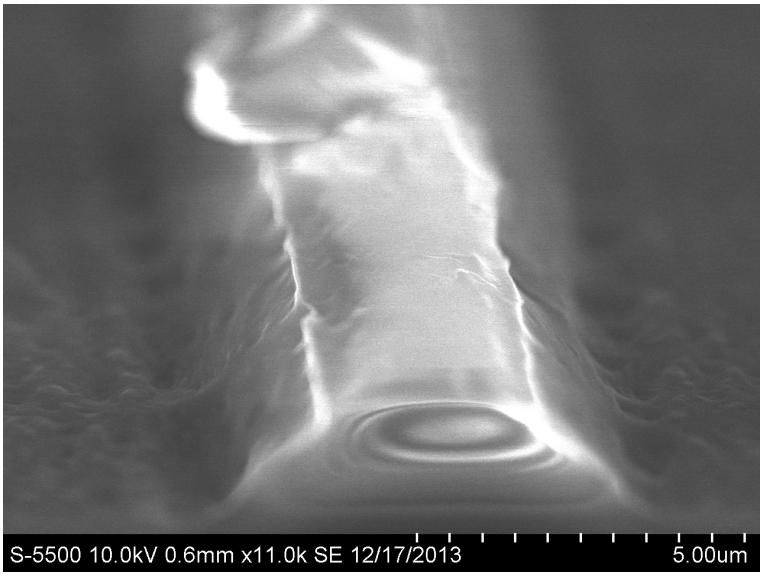

Figure 5.50: *Angled view of the resist line. Resist is still present in the trenches.*

5.6 Result summary and discussion

This section will summarise the most important results given in this chapter and discuss the findings collectively.

In the discussion of sample L5.01 it was indicated that the error imposed by setting the dose for the elements automatically was greater than assumed, or that there was something inherent in the different masks files that would require one mask to have a lower dose scale factor than another. According to these results along with the results of sample L5.01, L5.02 and L5.03, both of these statements are false. Both samples retained the same resist thickness, however results from sample L5.01 showed the features from the mask in figure 4.7 to be best developed for a dose scale factor of 1.8 and 1.92 while results from sample L5.03 show the larger mask in figure 4.6 to require a slightly lower dose scale factor than 1.2. The element doses were kept constant for all L5 samples. This along with equal resist thickness indicates that the required dose factors should have been the same, and thereby invalidating the large error in dose hypothesis.

The results from this sample, L5.05, show that each mask requires approximately the same dose to be developed adequately. This then invalidates the hypothesis that there is something inherent in the different mask files that would require one mask to receive a higher dose than another.

Having concluded that all the mask designs need the same amount of exposure dose for the same sample enables the comparison of exposure doses for sample L5.01 to samples L5.03 and L5.05. Sample L5.01 retained a resist layer thickness of 252.2 nm and showed best developed features for dose scale factors of 1.8 and 1.92. However sample L5.03 retained approximately the same resist layer thickness of 250.5 nm yet indicated that a dose scale factor between 1.1 and 1.2 would be optimal. Sample L5.05 retained a significantly lower resist layer thickness of 186.5 nm yet required an increase in dose scale factor, results indicating 1.3 to be the optimal dose. Resist uniformity is a concern as demonstrated by the results shown in figure 5.47 of sample L5.05. However if uniformity was an issue to such a degree that the difference would range from needing a dose scale factor of 1.2 to 1.8 the larger mask would have presented extensive differences in development of the waveguides on the same sample. While the larger mask has typically needed a lower dose, this has been true for the whole mask. At the end of the semester the light bulb of the reflectometer went out. If the bulb was about to go out the intensity could have fluctuated, resulting in measurement error. However, the measurements have been consistent and predictable. Therefore making the probable assumption that the reflectometer measurements are correct within a tolerable margin of error, these results then leave two possible explanations. (1) The EBL exposure doses vary slowly during the course of a semester, or the dose delivered by the electron beam depends on other conditions than the software settings. (2) The composition of the resist layer varies with each sample, indicating that the dose required by the PMMA depends on something in addition to resist thickness and resist type. For instance if the sample have been in contact with moisture from the breath of the user. Explanation (1) is implausible as the dose is dependent on the beam current. Any conditions which would alter the beam current is counteracted since the exact current is measured before exposing. A poorly grounded sample on the stage could cause variations in the electron beam, however this would also manifest as poor resolution when using the SEM of the EBL, which was not the case for these samples. Explanation (2) is conceivable. The design and routines of the cleanroom are devised to minimize humidity, in addition to other concerns. However, despite masks being worn, a sample raised close to the face during inspection could introduce increased hydration to the resist

layer, and the sample. Increased PMMA film hydration may cause increased scattering and absorption of electrons, requiring a higher dose to expose the pattern. Note that even though different resist blends were used, all the blends were made from the same PMMA and anisol bottles. After spin coating and soft bake the anisol should be completely evaporated, therefore the amount of anisol in the different blends should be of no consequence. Unfortunately there is insufficient data to determine what the source is for this irregularity in required dose. Additional systematic experiments are needed to understand the widely varying dose requirements for seemingly equal samples.

A relation between the dose scale factors changed in the gds-editor and the position list were found when defining a dose for both for the same exposure. The relation was deduced from empirical data acquired while performing the EBL exposure dose precedence test. It was found to be

$$\text{Actual DSF} = \text{gds DSF} \times \text{p.l. DSF}, \tag{5.33}$$

and concluded that the taper with the best defined features for sample L5.01 had an actual exposure dose of 1.92.

When the electron beam lithography parameters are optimized, approximately 90° sidewall profiles are realised and the roughness size becomes ∼5 nm which is the maximum size for a waveguide. Overexposed samples during this work have presented increased roughness size and positive profiles, however the roughness size may also depend on temperature during development according to Mohammad et al.[59]. Sidewall roughness showed great improvement with dose optimisation and development temperature has not varied by more than a degree, not enough to cause significant increase in roughness. The improvement of the sidewall profiles when the optimal exposure dose was found indicate that the positive profiles were caused by overexposure, and that the etching recipe is optimised for straight sidewall profiles. It should be noted that the etching time was reduced along with the exposure and may also have been a factor in improving the sidewall profiles. However, when considering figures 5.46c and 5.46d two pieces of information are indicated. The first is that underexposure causes positive sidewall profiles. The second is that the sidewalls feature positive profiles despite the decreased etch time. This indicates that the etching time does not contribute significantly in producing straight sidewall profiles when etching a pure single crystalline silicon wafer. The 5 nm roughness is most likely an attribute of the etching process. Either from the random locations and angles of the incoming etching radicals or the deposition of the passivation layer,

which has been observed deposited on the sidewalls. Roughness of 5 nm will yield attenuation of 60dB/cm for a 400 × 200 nm^2 waveguide core according to [3]. The passivation layer is thought to consist of mostly CF_i(i=1,2,3) bonds[46]. If the roughness is caused mostly by the deposition of the passivation layer the losses caused would be dependent on the refractive index of this material. These achievements are very promising for future work with micro- and nano-scale silicon photonic waveguides at the NTNU NanoLab. The fabrication process have been optimised for the desired sidewall profile and roughness size can be improved further by optimising the etch process or by adding more process steps after the etch process. Fabricating the waveguides, as optimised in this work, on silicon-on-insulator(SOI) wafers and placed in a test bench with proper spot-size converters would likely provide measurable results. However, the roughness induced losses would be significant. Note that when fabricating on SOI the silicon-silicon dioxide interface must be considered. If etching continues after the top silicon layer has been removed, notching may occur[48]. This only briefly touches subjects of roughness and sidewall profiles, but to fully exhaust a discussion on these topics a deeper study of the theory is required.

The write field alignment is shown to vary significantly and have been attributed to sample tilt. This can be counteracted by ensuring that no dust or residual resist lies between the sample and the stage. This can be done by thoroughly cleaning the back side of the sample and the EBL stage. There is a possibility of accounting for sample tilt in the Elphy Plus software. However Beckwith[41] suggests that other methods may be preferred if correct write field alignment is critical. If write field misalignment is kept below 40 nm at every 100 μm misalignment losses will be insignificant compared to roughness losses. However, T-shaped tapers should be avoided as they will result in significant reflection losses when coupling to the waveguide from optical fibres. This is most easily avoided by designing the mask such that alignment occurs after the light is fully coupled to the silicon waveguide. Another possibility is to use nanoimprint lithography which have the advantage of faster exposure times for large masks and avoiding alignment issues. A disadvantage, however, is that the mask cannot easily be corrected as making a new mask is costly and can take several weeks.

As seen from early results large aspect ratio features in the resist causes the features to topple or loose adhesion, and deform, during development. The implication is that when reducing features to a certain size the resist layer thickness must also be reduced. When increasing the taper tips to 150 nm and reducing the PMMA thickness to below 200 nm the features were well

defined with sidewall roughness comparable to the main waveguides as seen in figures 5.46e and 5.46f for sample L5.05. To realise taper tips of 80 nm the mask thickness must be reduced further, probably to 100 nm or lower. This would require greater selectivity during etch, however. This can be achieved by changing the etch recipe, or by changing the mask. A hard mask eliminates both issues as the high selectivity allows the mask thickness to be greatly reduced and deposition techniques such as e-beam evaporation produce considerably better uniformity. Shearn et al.[43] proposes using alumina in lieu of other metal masks because of its electric insulation. It is important to note that for small features overexposure might be devastating.

A thin layer of PMMA was discovered to be present on most of the waveguides after the samples were cleaned with acetone. This is observed to cause ledges to appear on the corners of the waveguide causing difficulties in discerning sidewall roughness from a top down perspective. Submerging the sample in acetone for 5 minutes is not enough to completely strip it of all resist. To ensure that all resist is removed from the sample it should be submerged in acetone and placed in a sonic bath for upwards of 20 minutes. Resist present on critical features like a sharp bend could cause adverse effects, to which extent is determined by the resists refractive index.

The coupling region between the waveguide and the racetrack resonator will receive slightly less proximity effects. If the exposure dose is optimised to the stand-alone waveguides this results in the coupling region receiving a slightly smaller effective dose which may cause a small widening of the waveguides in this region. Depending on the dimensions this could introduce higher order TE and TM modes. This would cause coupling between modes and change the amount of light coupling into the resonator. The wider waveguides could cause the distance between the waveguides to shrink. The consequence of this would be that the light would couple faster into the racetrack resonator and start coupling back before going through the resonator. To ensure that higher order modes does not appear in the coupling region, the waveguide should be designed such that the dimensions are tens of nanometres below the critical dimensions that satisfy the single mode condition. If 100% coupling is critical, the precise dimensions the reduced proximity effect produce must be investigated and accounted for in the mask design.

The spot-size converters made in this work was done in a first try trial run with many issues related to an inexperienced user. However, as indicated by Breivik's[58] results as well as the datasheet for S1800 G2 resist[60], the sidewall

profiles and roughness can be greatly improved by a more experienced user. If spot-size converters with 90° sidewalls can be realised from photoresist with minimal roughness this could provide an easy process for researchers to couple light into test samples. Correctly designed, light should only propagate through the SSC a short distance($\sim$100 μm). This indicates that the requirements for less sidewall roughness are more relaxed than for the silicon waveguides if minimizing losses are not critical. Photoresist spot-size converters must be added as the last step, however, as any temperatures above $\sim 130°C$ would cause resist re-flow to deform features.

Table 5.12: The yielded thickness of the different spin recipes.

Sample	*Resist blend*	*Recipe*	*Yield [nm]*	*Goodness of fit, g*
L4.15	Deteriorated A5.5	Table 5.1	611.1	0.996
L4.14	Deteriorated A5.5	Table 5.1	580.0	0.995
L4.13	Deteriorated A5.5	Table 5.3	517.9	0.9968
L4.11	Deteriorated A5.5	Table 5.4	559.9	0.9984
L4.09	Deteriorated A5.5	Table 5.5	471.2	0.955
Sample	*PMMA A9[%]/Anisol[%]*	*Recipe*	*Yield [nm]*	*g*
L4.08	25/75	Table 5.6	95.86	0.9992
L4.07	33/66	Table 5.6	169.0	0.9706
L4.06	50/50	Table 5.6	319.1	0.9985
L4.05	50/50	Table 5.6	295.6	0.9979
L4.04	50/50	Table 5.8	259.9	0.9981
L4.03	50/50	Table 5.8	273.1	0.9992
L4.02	50/50	Table 5.8	252.4	0.999
L4.01	50/50	Table 5.8	251.7	0.9912
L5.01	50/50	Table 5.8	252.2	0.9993
L5.02	50/50	Table 5.8	255.9	0.9969
L5.03	50/50	Table 5.8	250.5	0.9995
L5.04	50/50	Table 5.8	277.0	0.9993
L5.05	33/66	Table 5.11	186.5	0.995

Table 5.12 summarizes the results for spin coating yields. The results are consistent and predictable according to the intended yields of the recipes. Samples L4.03 and L5.04 show some irregularities yielding a thicker resist layer with respect to the known conditions. A possible explanation is that the resist is not perfectly homogeneous and that the resist was drawn from deeper within the bottle, providing thicker resist. It is also possible that the resist was in some way more hydrated before being spun on to the sample, causing a thicker layer.

The silicon etch rates throughout this work has varied significantly, however the PMMA etch rates have varied to the same degree. This is probably an effect of changing process conditions. Shearn et al.[43] mention that selectivity values are highly dependent on process conditions and are seen to widely vary. Selectivity values in this work has been consistent. This is most likely caused by the fact that for most of the time only this project was using this particular ICP-RIE system. Therefore the process conditions were kept constant. Table 5.13 show the average etch rates and selectivity for the etching process with silicon carriers and sapphire carriers. As can be seen the impact on the silicon etch rate was significant. The higher etch rate was attributed to an increase in available reactive ions[43]. There was a noticeable impact on the PMMA etch rate as well, however it is much lower. Having more available ions by switching carrier wafers could possibly account for a slightly more physical etch, similarly to how increasing the ICP power slightly increases the physical part of an etch[43]. As the silicon etch is shallow, a high selectivity is not needed, and a silicon:PMMA selectivity of 2:1 have been sufficient for this work.

Table 5.13: The average etch rates and selectivity.

Parameter	*Amount*	*Unit*
Silicon etch rate with Silicon carrier	593.64	$[^{nm}/_{min}]$
Silicon etch rate with Sapphire carrier	848.68	$[^{nm}/_{min}]$
PMMA etch rate - Silicon carrier	363.89	$[^{nm}/_{min}]$
PMMA etch rate - Sapphire carrier	408.81	$[^{nm}/_{min}]$
Selectivity - Silicon carrier	1.73:1	[1]
Selectivity - Sapphire carrier	2.11:1	[1]

Chapter 6

Conclusions

This work has gone through mask design and electron beam optimisation, with respect to feature size and development, in detail. Electron beam dose requirement with respect to resist layer thickness has been studied and discovered to fluctuate significantly. Although the issue was discussed and a few explanations were proposed, no conclusion could be reached regarding the cause of the fluctuations without further study. Write field alignment was investigated and was thought to vary depending on sample tilt. Therefore using tilt correction during exposure is necessary when fabricating photonic waveguides, which depends critically on good alignment between write fields.

Resist thickness was investigated and suitable resist blends were made to produce the desired thickness. A low resist thickness was found to be required when exposing very small feature sizes, as the resist would topple and deform when high aspect ratio features in the resist were developed. However, etching results of sample L5.05 reveal that mask uniformity must be considered, in some areas the mask may deviate from the measured thickness by tens of nanometres. By substituting the PMMA with a hard mask eliminates both issues.

A thin layer of PMMA on top of the waveguides after acetone cleaning was discovered. The samples must undergo a more thorough clean such as a sonic bath to ensure removal of the resist.

Optimised doses along with optimised resist thickness produced straight sidewall profiles and roughness size of $\sim$5 nm without changing any etching parameters

other than etch time and carrier wafer. It was discovered that over- and underexposure during electron beam lithography will cause positive sidewall profiles, while the etching time was found not to contribute significantly to sidewall profiles. The roughness of waveguides fabricated using an optimal EBL dose is postulated to be introduced either by the etching radicals or by deposition of the passivation layer.

The relation between the dose scale factor used from the gds-file and the dose scale factor used from the position list was found through empirical study and the optimal dose scale factor for sample L5.01 was found to be 1.92.

The coupling region between the waveguide and the racetrack resonator was discovered to receive a smaller dose, resulting in slightly wider waveguides in this area. A widening of the waveguides can induce higher order modes and reduce the efficiency of the coupling region. This can be counteracted by using waveguide dimensions tens of nanometres below the dimensions needed for single mode waveguiding, or by accounting for the widening waveguides in the mask design.

SOI and testing were discussed with respect to the realised waveguides which were considered to be functional. However, the roughness size of $\sim$5 nm will produce high propagation losses. Nevertheless this very promising for future silicon waveguide fabrication at the NTNU NanoLab.

In preparation for test work, external coupling was considered in the design. Inverse tapered waveguides with polymer spot-size converters fabricated from photoresist were chosen because this would only add one extra process step, minimizing process complexity. The final design tapered the waveguides from 500 nm to 150 nm over a course of 100 μm. The spot-size converters were chosen to be fabricated from S1818 photoresist and have 3×3 μm^2 cross-section dimensions. Time would only allow one fabrication test of the spot-size converters and the resulting SSCs were found to have positive profiles and rounded tops. However, optimisation of the fabrication process is postulated to produce functional spot-size converters.

Switching the carrier wafer during etch from silicon to sapphire was an attempt to minimize silicon re-deposition during etching. The deposited material on the waveguides was discovered to be residual PMMA, however higher etch rates and greater selectivity was observed while using the sapphire carrier. The average selectivity was found to be 1.73 while using a silicon carrier wafer, and 2.11 while using a sapphire carrier wafer.

6.1 Future work

Hopefully this thesis will provide a platform for future work in photonic waveguiding and provide adequate information to begin work with silicon-on-insulator wafers and testing at the NTNU NanoLab. Many possibilities for future work are recognized in this thesis, including, but not limited to:

- More systematic experiments to determine the cause of the fluctuating dose requirement.
- Deeper study of the theory to along with experiments to discover the cause of the roughness during etching.
- Optimisation of the etching process step and adding additional process steps to minimize sidewall roughness.
- Optimising the fabrication process for spot-size converters to improve sidewall profiles and roughness.
- Incorporating a hard mask to decrease the tip width of the tapered waveguides to 80 nm.
- Investigate roughness induced losses in small silicon-on-insulator racetrack resonators.

Bibliography

[1] Bahram Jalali and Sasan Fathpour. Silicon photonics. *JOURNAL OF LIGHTWAVE TECHNOLOGY*, 24(12), 2006.

[2] Wim Bogaerts, Peter De Heyn, Thomas Van Vaerenbergh, Katrien De Vos, Shankar Kumar Selvaraja, Tom Claes, Pieter Dumon, Peter Bienstman, Dries Van Thourhout, and Roel Baets. Silicon microring resonators. *Laser & Photonics reviews*, 6(1), January(September) 2012(2011).

[3] K. Yamada. *Silicon Photonics II*, chapter 1. Springer, 2011.

[4] D. Fattal Q. Xu and R.G. Beausoleil. Silicon microring resonators with 1.5-μm radius. *OPTICS EXPRESS*, 16(6), 2008.

[5] Jens Høvik. Photonic crystal waveguide fabrication. Master's thesis, Norwegian University of Science and Technology, August 2012.

[6] Marius Lorvik. Photonic crystal structures - design and fabrication. Master's thesis, Norwegian University of Science and Technology, July 2013.

[7] Leidulv Vigen. Simulations of silicon-on-insulator micro-ring resonators. Norwegian University of Science and Technology, May 2013. Project thesis.

[8] Shankar Kumar Selvaraja. *Wafer-scale fabrication technology for silicon photonic integrated circuits*. PhD thesis, Gent University, 2011.

[9] David K. Cheng. *Field and Wave Electromagnetics*, chapter 3.8. ADDISON-WESLEY, 2nd edition, 1989.

[10] David K. Cheng. *Field and Wave Electromagnetics*, chapter 6.7. ADDISON-WESLEY, 2nd edition, 1989.

[11] David J. Griffiths. *Introduction to Electrodynamics*. Prentice Hall, 1999.

[12] David K. Cheng. *Field and Wave Electromagnetics*, chapter 7.3. ADDISON-WESLEY, 2nd edition, 1989.

[13] David K. Cheng. *Field and Wave Electromagnetics*, chapter 6. ADDISON-WESLEY, 2nd edition, 1989.

[14] B.E.A Saleh & M.C. Teich. *Fundamentals of Photonics*, chapter 5.1. Wiley, 2nd edition, 2007.

[15] David K. Cheng. *Field and Wave Electromagnetics*, chapter 7.5. ADDISON-WESLEY, 2nd edition, 1989.

[16] Erwin Kreyszig. *Advanced Engineering Mathematics*, chapter 12.3. John Wiley & Sons, Inc., 9th edition, 2006.

[17] Erwin Kreyszig. *Advanced Engineering Mathematics*, chapter 11. John Wiley & Sons, Inc., 9th edition, 2006.

[18] Max Born & Emil Wolf. *Principles of Optics - Electromagnetic Theory of Propagation, Interference and Diffraction of Light*, chapter 1.1. Pergamon Press, 5th edition, 1975.

[19] B.E.A Saleh & M.C. Teich. *Fundamentals of Photonics*, chapter 12. Wiley, 2nd edition, 2007.

[20] Katsunari Okamoto. *Fundamentals of optical waveguides*, chapter 4. Academic Press, 2006.

[21] Jia-Ming Liu. *Photonic Devices*, chapter 4. Cambridge University Press, 2009.

[22] B.E.A Saleh & M.C. Teich. *Fundamentals of Photonics*, chapter 8. Wiley, 2nd edition, 2007.

[23] Zhou Fang and Ce Zhou Zhao. Recent progress in silicon photonics: A review. *ISRN Optics*, 2012.

[24] B.E.A Saleh & M.C. Teich. *Fundamentals of Photonics*, chapter 8.2. Wiley, 2nd edition, 2007.

[25] T. D. Visser, H. Blok, B. Demeulenaere, and D. Lenstra. Confinement factors and gain in optical amplifiers. *IEEE JOURNAL OF QUANTUM ELECTRONICS*, 33(10), 1997.

[26] B.E.A Saleh & M.C. Teich. *Fundamentals of Photonics*, chapter 5.3. Wiley, 2nd edition, 2007.

[27] R.G. Hunsperger. *Integrated Optics - Theory and Technology*, chapter 2. Springer Science+Business Media, 2009.

[28] B.E.A Saleh & M.C. Teich. *Fundamentals of Photonics*, chapter 8.3. Wiley, 2nd edition, 2007.

[29] Fengnian Xia, Lidija Sekaric, M. O'Boyle, and Y. Vlasov. Coupled resonator optical waveguides based on silicon-on-insulator photonic wires. *Applied Physics Letters*, 89, 2006.

[30] A. Einat and Uriel Levy. Analysis of the optical force in the micro ring resonator. *OPTICS EXPRESS*, 19(21), 2011.

[31] Peter De heyn, Diedrik Vermeulen, Dries Van Thourhout, and Gunther Roelkens. Silicon-on-insulator all-pass microring resonators using a polarization rotating coupling section. *IEEE PHOTONICS TECHNOLOGY LETTERS*, 24(14), 2012.

[32] M. K. Chin, C. Youtsey, W. Zhao, T. Pierson, Z. Ren, S.L. Wu, L. Wang, Y. G. Zhao, and S. T. Ho. Gaas microcavity channel-dropping filter based on a race-track resonator. *IEEE PHOTONICS TECHNOLOGY LETTERS*, 11(12), 1999.

[33] William R. Headley, Graham T. Reed, Simon Howe, Ansheng Liu, and Mario Paniccia. Polarization-independent optical racetrack resonators using rib waveguides on silicon-on-insulator. *Applied Phsysics Letters*, 85(23), 2004.

[34] Gregory N. De Brabander, Joseph T. Boyd, and G. Beheim. Integrated optical ring resonator with micromechanical diaphragm for pressure sensing. *IEEE PHOTONICS TECHNOLOGY LETTERS*, 6(5), 1994.

[35] Microring resonators. `https://www-eng.llnl.gov/mic_nano/mic_nano_micro_ring.html`.

[36] Giora Griffel. Synthesis of optical filters using ring resonator arrays. *IEEE PHOTONICS TECHNOLOGY LETTERS*, 12(7), 2000.

[37] Katrien De Vos, Irene Bartolozzi, Etienne Schacht, Peter Bienstman, and Roel Baets. Silicon-on-insulator microring resonator for sensitive and label-free biosensing. *Optics Express*, 15(12), 2007.

[38] Shinji Matsuo and Toru Segawa. Microring-resonator-based widely tunable lasers. *IEEE JOURNAL OF SELECTED TOPICS IN QUANTUM ELECTRONICS*, 15(3), 2009.

[39] K. Tiefenthaler and W. Lukosz. Sensitivity of grating couplers as integrated-optical chemical sensors. *Optical Society of America*, 6(2), 1989.

[40] T. Shoji, T. Tsuchizawa, T. Watanabe, K. Yamada, and H. Morita. Low loss mode size converter from 0.3pm square si wire waveguides to singlemode fibres. *ELECTRONICS LETTERS*, 38(25), 2002.

[41] Kai Müller Beckwith. Improving EBL performance for writing nanostructure arrays over large areas. Document to be integrated with the electron beam lithography training at NTNU NanoLab, November 2013.

[42] Joe Nabity, Lesely Anglin Campell, Mo Zho, and Weilie Zhou. *Scanning Microscopy for Nanotechnology*, chapter 5. Springer, 2007.

[43] Michael Shearn, Xiankai Sun, M. David Henry, Amnon Yariv, and Axel Scherer. *Semiconductor Technologies*, chapter 5. InTech, April 2010.

[44] Henri Jansen, Meint de Boer, and Miko Elwenspoek. The black silicon method vi: High aspect ratio trench etching for MEMS application. In *The Ninth Annual International Workshop on Micro Electro Mechanical Systems*. IEEE, 1996.

[45] Rob Legtenberg, Henri Jansen, Meint de Boer, and Miko Elwenspoek. Anisotropic reactive ion etching of silicon using sf6/o2/chf3 gas mixtures. *Journal of the Electrochemical Society*, 142(6), 1995.

[46] C. Gatzert, A. W. Blakers, Prakash N. K. Deenapanray, D. Macdonald, and F. D. Auret. Investigation of reactive ion etching of dielectrics and Si in CHF3/O2 or CHF3/Ar for photovoltaic applications. *Journal of Vacuum Science and Technology A*, 24(5), 2006.

[47] Michael Quirk and Julian Serda. *Semiconductor Manufacturing Technology*. Prentice Hall, 2001.

[48] S. L. Lai, D. Johnson, and R. Westerman. Aspect ratio dependent etching lag reduction in deep silicon etch processes. *Journal of Vacuum Science and Technology A*, 24(4), June 2006.

[49] P. Hublina, J. Luňáček, D. Ciprian, and R. Chlebus. Spectral interferometry and reflectometry used to measure thin films. *Applied Physics B, Lasers and Optics*, 92(2), 2008.

[50] Frederik Van Laere, Tom Claes, Jonathan Schrauwen, Stijn Scheerlinck, Wim Bogaerts, Dirk Taillaert, Liam O'Faolain, Dries Van Thourhout, and Roel Baets. Compact focusing grating couplers for silicon-on-insulator integrated circuits. *IEEE PHOTONICS TECHNOLOGY LETTERS*, 19(23), December 2007.

[51] Guanghui Ren, Shaowu Chen, Yongpeng Cheng, and Yao Zhai. Study on inverse taper based mode transformer for low loss coupling between silicon wire waveguide and lensed fiber. *Optics Communications*, June 2011.

[52] MicroChem. PMMA DataSheet. `http://microchem.com/pdf/PMMA_Data_Sheet.pdf`.

[53] J. H. Schmid, A. Delâge, B. Lamontagne, J. Lapointe, S. Janz, P. Cheben, A. Densmore, P. Waldron, D.-X. Xu, , and K. P. Yap. Interference effect in scattering loss of high-indexcontrast planar waveguides caused by boundary reflections. *OPTICS LETTERS*, 33(13), 2008.

[54] S. Thoms and D. S. Macintyre. Tilt-corrected stitching for electron beam lithography. *Microelectronic Engineering*, 84, 2007.

[55] Martin Peckerar, David Sander, Ankur Srivastava, Adakou Foli, and Uzi Vishkin. Electron beam and optical proximity effect reduction for nanolithography: New results. *Journal of Vacuum science & Technology B*, 25, 2007.

[56] *Elphy plus software reference manual.*

[57] Jae-Ho Min, Sung-Wook Hwang, Gyeo-Re Lee, and Sang Heup Moon. Redeposition of etch products on sidewalls during SiO2 etching in a fluorocarbon plasma. IV. Effects of substrate temperature in a CF4 plasma. *Journal of Vacuum Science and Technology B*, 21(5), 2003.

[58] Magnus Breivik. *Fabrication of mid-infrared laser diodes.* PhD thesis, Norwegian University of Science and Technology, 2013:373.

[59] Mohammad Ali Mohammad, Mustafa Muhammad, Steven K. Dew, and Maria Stepanova. *Nanofabrication - Techniques and Principles*, chapter 2. Springer, 2012.

[60] Rhom and Haas. S1800 G2 series photoresist DataSheet. http://www.microresist.de/products/room_haas/pdf/microposit_s1800_g2_serie.pdf.

Appendix A

Sample numbering

Using sample L4.16 as an example; the L indicates the user, the number following the letter indicates the wafer number, and the number following the punctuation indicates the die number. After the silicon wafer was broken into square samples, the condition of the samples were rated, 1 being the best condition and 16 being the lowest condition. At the start of the work it made sense to make all the mistakes on the samples in the worst condition and work towards the samples in better condition as the users skill increased. This is why the results start with die number 16. When moving on to the next wafer it made sense to continue the work on the samples in the best condition, which is why the results from the samples from wafer number 5 begins on die 1.

Appendix B

List of instruments

Table B.1: A list of the instruments used throughout this work. The numbering is the NTNU NanoLab internal ID.

NanoLab ID number	*Tool type*	*Model*	*Manufacturer*
1103	EBL	4300 SEM & Raith electronics	Hitachi
1207	ICP-RIE	Plasmalab System 100 ICP-RIE 180	Oxford Instruments
1512	SEM	S-5500 S(T)EM	Hitachi
1720	Profilometer	Dektak 150	Veeco
3021	Scriber	DXIII	Dynatex
1500	Reflectometer	F20	Filmetrics